

**Engineered Acoustic Emission Sensing in Metallic Structures by
Phononic Crystals and MEMS Sensors**

by

MINOO KABIR

B.S. (Sharif University of Technology) 2011

M.S. (Sharif University of Technology) 2013

Thesis submitted in partial fulfillment of the requirements
for the degree of Doctor of Philosophy in Civil Engineering
in the Graduate College of the
University of Illinois at Chicago, 2018

Chicago, Illinois

Defense Committee:

Dr. Didem Ozevin, Chair and Advisor

Dr. J. Ernesto Indacochea, Civil & Materials Engineering

Dr. Eduard Karpov, Civil & Materials Engineering

Dr. Mustafa Mahamid, Civil & Materials Engineering

Dr. Carmen Lilley, Mechanical & Industrial Engineering

Copyright by
MINOO KABIR
2018

This thesis is dedicated to,

my dearest and wonderful parents,

and my beloved and brilliant husband, Amir,

I'm blessed to have them in my life.

ACKNOWLEDGMENTS

These years of graduate study at University of Illinois at Chicago has been a period of extensive learning for me, both academically and personally. I would like to acknowledge all the individual who trained me, supported me, and cheered me along the way. First and foremost, I would like to offer my deepest gratitude to my advisor, Professor Didem Ozevin, for always being encouraging, supporting and inspiring me. I thank her for not only being a great teacher and mentor for me, but also providing the opportunity to explore new ideas and grow as an independent researcher.

I would like to express my sincere gratitude to all members of my thesis committee, Professors J.Ernesto Indacochea, Mustafa Mahamid, Eduard Karpov and Carmen Lilley for reviewing my work and giving me helpful advice. Also I would like to thank Prof. Farhad Ansari for his time and advice through the preliminary stage of my work.

I would also like to thank members of Non-Destructive Evaluation laboratory over these years. Prof. Chudnovsky for teaching outstanding classes. Many thanks to Lu, Hanieh, Zeynab, Onur and Gorkem, for providing a friendly work environment. Also, I would like to thank Dr. Zhou, Dr. An, for opening their laboratories, providing testing equipment and support. Much appreciation to the department's staff, Pam, Sara, Dandel, and James.

I would like to thank my family for their love and support throughout all my life. Thanks to my wonderful parents, Tahmineh and Aliasghar, for having absolute faith in me and being always supporting. Thanks to my wonderful siblings, my beloved brother Aliakbar and his lovely wife Mina, my beloved Maryam and Payam for providing me through moral and emotional support. You guys are always there

ACKNOWLEDGMENTS (Continued)

for me. A special thanks to my adorable sister, Maryam, who was here next to me throughout the joy and hardship. And, there are my friends, Neda, Hossein, Hooman, Apameh, Amirhassan, Sanaz, Behnam, Zohre, Majid and Maryam. You guys are fantastic friends, my extended family. We were not only able to support each other by deliberating over our problems and findings, but also happily by talking about things other than just our papers.

Finally and most importantly, I thank my precious Amir, my soulmate and best friend. Thanks for supporting, encouraging and having faith in me at all times. I feel blessed to have you in my life.

Thank you very much, everyone!

CONTRIBUTION OF AUTHORS

This thesis includes six chapters. Chapter 1 introduces the problem statement and motivations, the objectives and scope, contributions, and summary of the research. In Chapter 2, the background literature are presented that covers the general understandings of the acoustic emission (AE) method and its application for damage assessment of metallic structures, phononic crystals, and MEMS AE sensors. The literature research presented in this chapter was partially published in the journal of Civil Structural Health Monitoring as "Noise Isolation with Phononic Crystals to Enhance Fatigue Crack Growth Detection using Acoustic Emission" in 2018 with my research advisor Dr. Ozevin and Ph.D. student Amir Mostavi as the co-authors [1], and in the journal of Sensors and Actuators A: Physical as "Piezoelectric MEMS Acoustic Emission Sensors" in 2018 with my research advisor Dr. Ozevin and Ph.D. student Hanie Kazari as the co-authors [2]. In Chapter 3, perforated PC plates are introduced, and numerical and experimental studies are presented. The content presented in this chapter was partially published in the proceeding of the SPIE 2016 conference of Nanoscience + Engineering as "Integration of periodic structure and highly narrowband MEMS sensor to enhance crack detection ability in steel structures" with my research advisor Dr. Ozevin as the co-author [3]. The experimental studies are performed implementing the MEMS AE sensors designed by Saboonchi et al. [4; 5]. In chapter 4, noise isolation through the stubbed PC structure is described, which includes numerical studies on the design of the PC structure and the experimental studies on the validation of the noise isolation through the PC. The content presented in this chapter has been published at the journal of Civil Structural Health Monitoring as "Noise Isolation with Phononic Crystals to Enhance Fatigue Crack Growth Detection using Acoustic Emission", with my research advisor Dr. Didem Ozevin and the Ph.D. student Amir Mostavi as the co-

CONTRIBUTION OF AUTHORS(continued)

authors [1]. Also, parts of the results presented in this chapter is already drafted and will be partially published in the journal as "An Approach towards the Repeatability of Acoustic Emission by Noise Isolation through Phononic Crystals" with my research advisor Dr. Ozevin and Ph.D. student Amir Mostavi as the co-authors. Kabir performed the numerical simulatio^s to design the PC structure and Mostavi prepared the experiments and analyzed the data, the experiments are preformed by Ozevin, Mostavi and Kabir, and Ozevin reviewed the results. Chapter 5 describes the design and characterization of the piezoelectric MEMS AE sensors. The content presented in this chapter has been published at the Journal of Sensors and Actuators A: Physical as "Piezoelectric MEMS Acoustic Emission Sensors", with my research advisor Dr. Didem Ozevin and Ph.D. student Hanie Kazari as the co-authors [2]. Kazari performed the literature studies, the L-Edit drawings and initial experiments were performed by Kabir and Kazari, Kabir performed the numerical simulations and Ozevin reviewed the results. The laboratory experiments were performed by Ozevin, Kabir and Kazari. The conclusions and future work are summarized in Chapter 6.

TABLE OF CONTENTS

<u>CHAPTER</u>	<u>PAGE</u>
1 INTRODUCTION	1
1.1 Problem Statement and Motivations	1
1.2 Research Objectives and Scope	2
1.3 Summary of Approach	3
1.4 Contribution to Knowledge	6
1.5 Organization of Dissertation	7
2 BACKGROUND LITERATURE	8
2.1 Acoustic Emission (AE) Method	8
2.1.1 The Application of AE Method to Steel Truss Bridges	10
2.2 Phononic Crystal (PC)	12
2.3 MEMS AE Sensors	15
2.3.1 Piezoelectric MEMS Sensors	17
3 PERFORATED PCS TUNED TO STRUCTURAL DESIGN AND DAMAGE DETECTION	19
3.1 Introduction	19
3.1.1 Numerical Studies	21
3.1.1.1 Unit Cell Analysis	22
3.1.1.2 Transmission Loss Analysis	26
3.2 MEMS AE Sensor	28
3.2.1 Experimental Results	29
3.3 Summary	33
4 NOISE ISOLATION THROUGH PHONONIC CRYSTALS	35
4.1 Introduction	35
4.2 Illustration of the Proposed Approach in Steel Structures	36
4.3 Numerical Studies	37
4.3.1 Phononic Crystal Models	39
4.3.2 CT Specimen Model	47
4.4 Experimental Study	48
4.4.1 Experimental Setup	48
4.4.2 Experimental Results	50
4.4.2.1 Cumulative AE Energy Behavior with Respect to Crack Size	50
4.4.2.2 Comparison of AE Waveforms	52
4.5 The Repeatability of Acoustic Emission to Detect Fatigue Crack Growth	56

TABLE OF CONTENTS (Continued)

<u>CHAPTER</u>		<u>PAGE</u>
	4.6 Summary	61
5	PIEZOELECTRIC MEMS AE SENSORS	65
	5.1 Introduction	65
	5.2 Description of Piezo-MEMS Device	66
	5.3 Sensor Design	66
	5.3.1 Manufacturing Process	66
	5.3.2 Final Sensor Design	69
	5.3.3 Numerical Studies	71
	5.4 Characterization Experiments	79
	5.4.1 Electromechanical Characterization	79
	5.4.2 Mechanical Characterization	81
	5.5 The Comparison of Conventional Piezoelectric and Piezo-MEMS AE Sensors	83
	5.6 Summary	87
6	CONCLUSIONS AND FUTURE WORK	91
	6.1 Conclusions	91
	6.2 Future Work	94
	APPENDICES	97
	CITED LITERATURE	102

LIST OF TABLES

<u>TABLE</u>		<u>PAGE</u>
I	SPECIMEN NAMES AND THEIR DATA ACQUISITION SETTING . . .	58
II	ELECTRICAL AND MECHANICAL PROPERTIES OF TWO COMMON PIEZOELECTRIC MATERIALS (ALN AND PZT)	71
III	MATERIAL PROPERTIES OF SI AND ALN AS USED IN NUMERI- CAL SIMULATION	74
IV	BEAMS AND OCTAGONAL DIMENSIONS	75
V	EXPERIMENTAL AND NUMERICAL RESONANT FREQUENCIES . .	82
VI	THE COMPARISON OF CONVENTIONAL PIEZOELECTRIC AND PIEZO- MEMS AE SENSORS	88

LIST OF FIGURES

<u>FIGURE</u>		<u>PAGE</u>
1	Integration of PC structure and MEMS sensor to focus wave propagation (b) dispersion curve of the PC structure (c) frequency response of MEMS sensor . .	4
2	Two types of phononic crystal plates: (a) periodically perforated plate, (b) surface stubbed plate	20
3	2D connection plate with bolts exhibiting some periodicity	21
4	Integrated behavior of the periodic perforated plate and MEMS AE sensor . . .	22
5	(a) Unit cell of the periodic structure, showing periodic boundary conditions applied on all sides of the unit cell, (b) first IBZ	24
6	(a) Dispersion curve of the perforated PC indicating the band gap near 60 <i>kHz</i> , (b) the unit cell of the PC illustrating the dimensions of the final design, and (c) the first IBZ of the square lattice	25
7	(a) Supercell geometry, (b) transmission loss through the supercell, (c) dispersion curve of the unit cell	27
8	(a) Displacement field at the frequency of 60 <i>kHz</i> and (b) displacement field at the frequency of 25 <i>kHz</i>	28
9	(a) The overview of MEMS device designed by Saboonchi, (b) the constituent cell of each type of sensor, and (c) the frequency domain spectra of the received signal by of S1 and S2	30
10	Experimental setup for testing one dimensional PC plate	31
11	Experimental results, (a) time histories, and (b) frequency spectra for 60 <i>kHz</i> excitation	31
12	Experimental results, (a) time domain response, and (b) frequency domain response for 150 <i>kHz</i> excitation	32
13	Frequency spectra of (a) the reference plate, and (b) the PC plate	33

LIST OF FIGURES (Continued)

<u>FIGURE</u>		<u>PAGE</u>
14	An example of application of the proposed method illustrating the (a) friction emissions generated at the bolted connection and (b) the incoming waves are reflected using the PC structure	38
15	The unit cell analysis of the PC structure, (a) periodic stubbed plate (b) the unit cell of the PC structure, presenting periodic boundary conditions applied on sides of the unit cell, (c) The first IBZ	39
16	The effect of (a) diameter and (b) height of stubs on the band gap frequency range	41
17	(a) Dispersion curve of the PC plate, indicating the band gap near 150 <i>kHz</i> , (b) the unit cell of the PC illustrating the dimensions of the final design, and (c) the first IBZ of the square lattice	42
18	The transmission analysis	43
19	(a) The waveforms extracted at points 1 and 2 (z-component of displacement field), (b) the frequency spectra of the time history waveforms	44
20	The z-component of displacement field (cm) at different time of study	44
21	Deformation of the stub at the edge of the band gap	45
22	The results of frequency domain analysis demonstrating the wave propagation through a path between the stubs, (a) three-dimensional geometry modeled in COMSOL, (b) the deformation of the stubs at 150 <i>kHz</i> excitation	46
23	(a) The standard CT specimen with dimensions in (<i>mm</i>), and (b) the von Mises stress (<i>MPa</i>) distribution in CT specimen	48
24	(a) The plain CT specimen, (b) the stubbed CT specimen	50
25	Experimental setup, demonstrating the Servo-hydraulic fatigue testing machine, the data acquisition system to monitor AE signals, and the optical microscope to control crack initiation and growth	51
26	C-scan images of the (a) plain and (b) stubbed CT specimens after the fatigue testing	52

LIST OF FIGURES (Continued)

<u>FIGURE</u>		<u>PAGE</u>
27	Cumulative AE energy and hit during the fatigue tests obtained from (a,b) the plain CT specimen and, (c,d) the stubbed CT specimen. (a,c) received by R6 sensor (b,d) are received by R15 sensor	53
28	Cumulative AE energy during the fatigue test received by R15 sensor along with the crack length measured by optical microscope, (a) the plain CT specimen and, (b) the stubbed CT specimen.	54
29	The initial cycles of received AE waveforms in different times of the fatigue test for (a) the plain CT specimen, and (b) the stubbed CT specimen.	55
30	Histogram of AE hit amplitudes for (a) the plain CT specimen, and (b) the stubbed CT specimen.	57
31	Cumulative AE energy and hits obtained from (a,c) PL2 and, (b,d) ST2. (a,b) show the results received by R6 sensor, and (c,d) show the results received by R15 sensor	59
32	Cumulative AE hits obtained from (a) PL1 and F-PL2, and (b) ST1 and F-ST2 received by the R15 sensor with the synchronized threshold of 45 dB.	60
33	Cumulative AE hits obtained from (a) PL1 and F-PL2, and (b) ST1 and F-ST2 received by the R6 sensor with the synchronized threshold of 50 dB.	61
34	Cumulative AE hits received from the R15 sensor with different amplitude filters for (a) PL2 and (b) ST2 specimens.	62
35	Cumulative AE hits received from the R6 sensor with different amplitude filters for (a) PL2 and (b) ST2 specimens.	63
36	The designed device layout, indicating four sub-layouts	67
37	Summary of the PiezoMUMPs	70
38	L-Edit plots illustrating the planar view of the sensors designed for (a) 40 kHz (LF) and (b) 200 kHz (HF), along with the schematic cross-sectional view of each sensor (unit: μm)	72
39	SEM images of (a) LF and (b) HF sensors (unit: μm)	73
40	The first and second mode shapes of LF (a,c) and HF (b,d) sensors	75

LIST OF FIGURES (Continued)

<u>FIGURE</u>		<u>PAGE</u>
41	The time-domain numerical simulation of the LF sensor, illustrating the defined AlN and silicon layers, the ground and terminal surfaces and the applied load	77
42	Time-domain numerical analysis of the LF sensor, (a) the waveform of the applied chirp, (b) the frequency spectrum of the applied chirp signal, (c) the waveform of the received signal and (d) the frequency spectrum of the received signal, (e) the displaced shapes at six different time positions	78
43	(a) The packaged piezo-MEMS device (b) the L-Edit image of the MEMS chip that includes LF and HF sensors (c) the SEM image of the HF sensors	79
44	Admittance results of the (a) LF and (b) HF sensors	81
45	Equivalent circuit model used to describe the electromechanical response of piezo-MEMS	82
46	Experimental setup for mechanical characterization of the LF and HF sensors using face-to-face excitation by conventional AE transducers	84
47	The LF sensor responses at different excitation frequencies (a) time history signals and (b) their frequency spectra	85
48	The HF sensor responses at different excitation frequencies (a) time history signals and (b) their frequency spectra	86
49	The peak amplitudes of time history signals due to different excitation frequencies	87
50	Experimental setup for the comparison of conventional piezoelectric AE sensors and piezo-MEMS AE sensors	88
51	The time history signals and their frequency spectra obtained from (a) HF (piezo-MEMS AE sensor), (b) R15 (conventional AE sensor), (c) LF (piezo-MEMS AE sensor), (d) R6 (conventional AE sensor)	89

LIST OF ABBREVIATIONS

AE	Acoustic Emission
BS	Bragg's Scattering
LR	Local Resonance
MEMS	Micro-Electro-Mechanical Systems
MetalMUMPs	Metal-Multi-User-MEMS-Processes
NDE	Nondestructive Evaluation
PC	Phononic Crystal
SHM	Structural Health Monitoring

SUMMARY

It is inevitable that infrastructures including bridges, pipelines, and aircraft components eventually develop cracks. Unfortunately, the inspectability of defects is not considered at the design stage. While Structural Health Monitoring (SHM) and/or Nondestructive Evaluation (NDE) methods of large-scale structures are imperative to ensure the structural integrity and identify the presence of flaws to prevent catastrophic failures in structures, the identification of the most suitable method to each structural system/problem is a challenge, especially for the unconsidered and inaccessible design details. The acoustic emission (AE) method is a passive SHM/NDE method that provides direct information about the presence of active defects in structures. The passive nature of this method allows continuous real time monitoring of structures, and eventually uninterrupted service and safety in critical civil structures. Although the AE method is a well-established technique for detecting and characterizing damage in structures, the method has two major drawbacks (background noise and attenuation), which are addressed in this research by introducing an engineered structural and AE approach. The components of the proposed approach are: (i) phononic crystals (PCs), which are spatially periodic subsystems artificially or naturally introduced into structural elements at later or design stage, to block, redirect and strengthen propagating elastic waves, and (ii) highly narrow band piezoelectric MEMS sensors tuned to the band gap of phononic crystals.

(i) PCs exhibit unnatural features, such as band gap formation. As a result, when a wave propagates through a periodic structure, the range of frequencies within the band gap are restricted. The formation of a band gap in PCs has been studied in many applications, such as sound isolation, acoustic mirrors

SUMMARY (Continued)

and waveguides. In this regard, the structural components could be designed based on analogy to PCs, as the existing structures exhibit some periodicity in structural elements, such as perforated beams and location of bolts in bridges. Currently, they are designed based on design requirements, such as stress distribution and minimum/maximum spacing requirements. However, the design can be integrated with the damage detection philosophy such that we can predict the damage presence through damage-induced imperfection and wave redirecting between periodic lines. In this study, two types of PCs are considered: (a) periodic perforated plate naturally introduced to design in order to guide the propagation of elastic waves in a predefined path to the location of the sensor, and (b) periodic stubbed plate artificially introduced to isolate background noise (e.g. friction emissions).

(ii) To further enhance the sensitivity of the sensing system, piezoelectric micro-electro-mechanical systems (MEMS) sensors with highly narrow band frequency response are designed. Piezo-MEMS sensors require low power for operation and are compatible with wireless communications which make them ideal to develop a remote monitoring system. They have highly narrowband response tuned to the band gap of the PC structure.

We aim to engineer structural geometry considering the inspectability of structures using the AE method. The combination of PCs and piezo-MEMS sensors is demonstrated numerically and experimentally to improve the performance of AE method and reduce the cost of monitoring system.

CHAPTER 1

INTRODUCTION

1.1 Problem Statement and Motivations

Monitoring the integrity of in-service infrastructures is an important objective to avoid many of the structural failures that are happening frequently. It is inevitable that infrastructures including bridges, pipelines, and aircraft components eventually develop cracks. Failures in structures cause large number of casualties and have negative social and economic impacts. The most recent bridge failure in Washington State over the Skagit River causing the closure of a main transportation system and the pipeline failure in Arkansas causing crude oil to flow through homes (estimate of 300,000 gallons and residents to be evacuated) are only two examples of the recent structural failures [6; 7]. Unfortunately, current design practice does not include the means of structural damage detection into the design process.

When structures reach their service life, they are regularly inspected using several Nondestructive Evaluation (NDE) methods, or monitored using Structural Health Monitoring (SHM) systems in real time continuously [5]. Currently, most of the highway bridges in the U.S. are inspected visually, and several studies indicated the current inspection method needs additional improvement to increase accuracy and reliability [8; 9; 10]. Existing continuous monitoring methods based on wave propagation still have several limitations such as the baseline requirement for Guided Wave Ultrasonic Testing [11; 12], and difficulties reaching into inaccessible areas for high frequency Ultrasonic Testing.

A continuous real time monitoring system can provide valuable information about status of structures, so that even the smallest crack energies, released by invisible micro-crack growths, can be identified long before the crack reaches the in-stable regime.

Among many SHM methods, acoustic emission (AE) method provides direct information about the presence of active defects in structures. Once a crack initiates inside a material, it generates elastic waves that propagate through the material to be captured by AE sensors attached on the surface of the structure. The AE signals are further analyzed to detect, locate and characterize the initiation and growth of defects. Although the AE method has been shown as a great potential for detecting damage in structures at their early stages, the method has two major drawbacks: (i) wave attenuates in long distances, which leads to placing sensors in close distances and increasing the monitoring cost, (ii) sub-millimeter crack detection requires highly sensitive sensors, which make them sensitive to the influence of external noise sources such as friction.

1.2 Research Objectives and Scope

The overall objective of this research is advancing current AE method through engineering structural components and AE sensing technique. Two major drawbacks of AE method, related to wave attenuation and sensitivity to the influence of background noise are aimed to be conquered. The proposed approach consist of two components: phononic crystals (introduced naturally at the design stage or artificially to existing structures) and piezoelectric MEMS sensors. PCs are introduced into structural elements to block, redirect and strengthen propagating elastic waves. Scattering or local resonance in PC medium affects the elastic wave spectrum (i.e., dispersion curve) such that certain waves cannot

propagate to the medium, known as stop-bands or band gaps. Such design allows the elastic waves emitted from any structural damage to be more easily focused and captured.

Furthermore, the wave field focusing is integrated with highly narrowband MEMS sensors tuned to the stop band of the PC. When acoustic sensors are tuned to stop-bands, they will not detect any signal until damage forms. Once a new crack forms, molecular bonds will be broken and release elastic waves inside the material [13; 14]. The elastic waves will propagate through the structure to be captured by the acoustic sensors attached to the surface of the structure. With focusing the wave field, the capabilities of AE method to detect the damage in structures can be enhanced. Figure 1 illustrates the concept of wave field focusing through the integration of PC structure and MEMS AE sensors. The dispersion curve of the PC structure, Figure 1(b), shows the range of band gap frequency and the frequency response of the MEMS sensor, Figure 1(c), is tuned to the stop band. The AE sensor is surrounded by PC medium, which block the background noise and secondary sources such as friction, that may interfere with primary AE sources.

1.3 Summary of Approach

In this research, an engineered AE sensing method is introduced based on focusing the wave energy released by the newly formed cracks using PCs, and detecting using highly narrow band MEMS AE sensors. This research consist of two major parts: the designs and the evaluations of (a) PC structures, and (b) piezoelectric MEMS AE sensors.

(a) Two types of PC structures are investigated in this study, where each type is designed to address a specific problem in AE monitoring of metallic structures. The PC types are briefly described bellow:

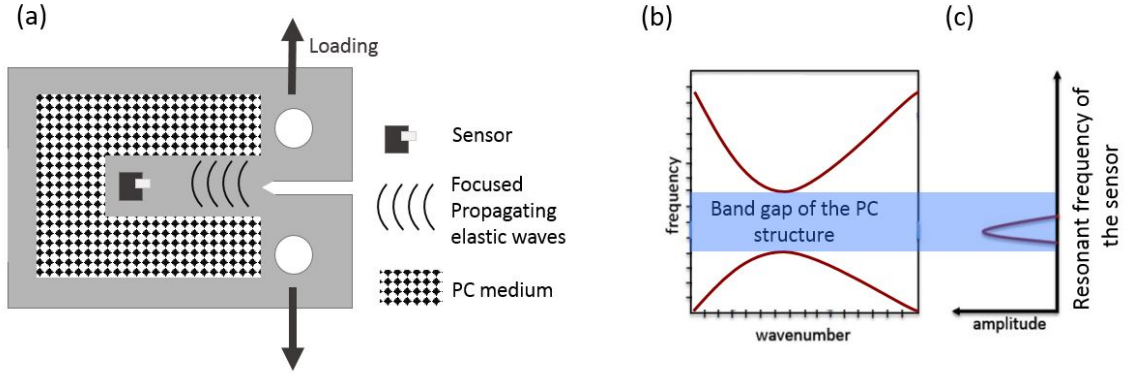


Figure 1. Integration of PC structure and MEMS sensor to focus wave propagation (b) dispersion curve of the PC structure (c) frequency response of MEMS sensor

1. Perforated PC plates: Existing structures exhibit some localized periodicity, such as equally spaced bolts in gusset plates. Currently, perforation locations of bolts at connections are placed based on stress distribution and minimum/maximum spacing requirements. However, the design can be integrated with the damage detection philosophy such that we can predict the damage presence through damage-induced imperfection and wave redirecting between periodic lines. Therefore, periodic perforated plates are numerically studied which resemble periodic location of bolts in connection plates. The dispersion curve of the PC plate is calculated numerically to find the range of frequency band gap. Then, the geometry is exploited to tune range of frequency band gap to the frequency response of the MEMS AE sensors, which is 60 kHz . A one-dimensional perforated PC is prepared and the band gap formation is demonstrated through experimental studies, where MEMS AE sensors are employed for sensing.

2. Stubbed PC plate: The major challenge that limits the application of AE method is background noise. Because the range of frequencies of the background noise is between 0.2 to 200 kHz, it interferes with the operating frequencies of the AE system; subsequently, limits the minimum detectable crack. Two-dimensional PCs in form of periodic cylinders attached to the surface of a plate are designed for noise isolation to monitor a particular location in plate-like structures, such that a single AE sensor is sufficient to monitor the crack activity. The stubs could be placed strategically such that they block the unwanted signals. The proposed PC is made of cylindrical stubs made of aluminum that are designed to block 150 kHz signals. This is the typical frequency used to monitor cracks in metallic structural components which are prevalent in civil and aerospace structures. The designed PC plate works with the mechanism of local resonances in stubs to form a band gap at the desired range of frequencies. The efficiency of the proposed method is demonstrated experimentally through the application of stubbed plate in fatigue testing of compact tension (CT) specimens. The stubs are placed on the CT specimen, except in the path between crack growth direction and the sensor position. The developed approach eliminates any post-processing filtering, which typically depends on experimental setup and limits the applicability of experimental results to other test conditions.

(b) Piezoelectric MEMS sensors are designed, manufactured and characterized. First, numerical studies, using COMSOL Multiphysics software, are implemented to tune them to the desired resonant frequencies. Then, they are fabricated using PiezoMUMPs by MEMSCAP. The PiezoMUMPs process is a 5-masks level SOI patterning and etching process, which includes deposition of 0.5 μm aluminum nitride (AlN) to form piezoelectric layer. The microstructural layers consist of doped silicon, AlN and

metal layer which are working as the bottom electrode, sensing layer and top electrode, respectively. Each design consists of a mass-spring system where a movable plate is connected with four partially clamped beams to the substrate. The mass and stiffness are controlled through the geometry of the beams and diaphragm to tune the sensors to the desired frequencies. The fabricated MEMS device is packaged and the electrical connections are made through wire bonding. The performance of the piezo-MEMS AE sensors is demonstrated through electromechanical and mechanical characterization experiments. The results of experimental studies on two of the sensors with resonant frequency of 40 *kHz* and 200 *kHz* are presented in this study, and they are compared with the conventional piezoelectric AE sensors.

1.4 Contribution to Knowledge

The research has two major contribution to knowledge:

- The proposed PC structure for noise isolation addresses one of the major challenges of real time monitoring of structures using the AE method. The designed PC removes the secondary sources unrelated to the crack growth. Besides, a single sensor would be sufficient for monitoring the crack activity. While, in current practice, multiple sensors and a guard sensors, as well as a filtering (such as first-hit channel), are deployed to intercept noise to monitor activity of a crack in the connection plate of bridges.
- The piezoelectric MEMS sensors for AE detection is designed uniquely for the first time in literature. The piezo-MEMS AE sensor with resonant frequency of 40 *kHz* is especially designed with a mass of entire silicon substrate in order to reduce the overall size of sensor while tuning it to lower frequency. This sensor demonstrates high Q-factor, leading to low damping and

very narrow frequency bandwidth, which is important for source localization, especially in dispersive medium where wave velocity depends on frequency. These sensors are developed using piezoMUMPs, which do not require power for operation. Compared to capacitive MEMS AE sensors, it is a significant advantage for field application.

1.5 Organization of Dissertation

The dissertation comprises of six chapters including the introduction section. In chapter 2, background literature relevant to this study is presented, including an introduction to AE method and its application on monitoring steel truss bridges, phononic crystals, and MEMS AE sensors. In chapter 3, perforated PC plates are introduced, and numerical and experimental studies are presented, which demonstrate the band gap formation through 1D perforated PC. In chapter 4, noise isolation through the stubbed PC structure is described, which includes numerical studies on the design of the PC structure and the experimental studies on the validation of the noise isolation through the PC. Chapter 5 describes the design and characterization of the piezoelectric MEMS AE sensors, followed by the conclusions and future work in chapter 6.

CHAPTER 2

BACKGROUND LITERATURE

The aim of this chapter is to give an outline of the acoustic emission (AE) method, its application for damage assessment of metallic structures, phononic crystals, and MEMS AE sensors. The chapter starts with an introduction to AE method in subsection 1, then the application of AE method for crack monitoring in steel bridges is explored. The challenges of the AE method are introduced, followed by an introduction to the proposed method to overcome the challenges. In subsection 2, phononic crystals are introduced. In subsection 3, MEMS AE sensors including two categories of capacitive and piezoelectric MEMS sensors are introduced.

The content presented in this chapter has been partially published in the journal of Civil Structural Health Monitoring as "Noise Isolation with Phononic Crystals to Enhance Fatigue Crack Growth Detection using Acoustic Emission" in 2018 with my research advisor Dr. Ozevin and Ph.D. student Amir Mostavi as the co-authors [1], and in the journal of Sensors and Actuators A: Physical as "Piezoelectric MEMS Acoustic Emission Sensors" in 2018 with my research advisor Dr. Ozevin and Ph.D. student Hanie Kazari as the co-authors [2].

2.1 Acoustic Emission (AE) Method

Acoustic emission (AE) is defined as transient stress waves generated by the release of energy due to newly formed cracks within a material [15], and can be recorded using sensors mounted on the surface of the material. During the 1960s, engineers became interested in utilizing AE as a technique of structural

evaluation, and significant process since then made it a valuable engineering tool [16]. The AE method has been used to detect, locate and characterize the initiation and growth of cracks inside materials [17]. Nowadays, the AE method is identified as a technique for the structural integrity assessment in a variety of structures, including bridges, buildings, pipelines and air craft components [18; 19; 20; 21; 22]. This is a passive nondestructive testing method where the AE sensors detect AE signals once the sensor response is above the pre-defined threshold. The detectability of an AE source decreases with the decrease of the energy release as threshold should be kept at a certain level to block high hit rates (e.g. above 45 dB - 50 dB [23]). The AE method has some dominant attributes that make it desirable over the other nondestructive monitoring methods, such as the ability to continuously and globally monitor large in-service structures [24; 25]. However, the data contamination due to the background noise has been always a challenge as it makes separating the relevant data difficult [26]. Typical causes for noise in infrastructures include friction at joints, fretting of bolted connections, and impact due to rain/snow. Because the range of frequencies of the background noise is between 0.2 to 200 kHz, it interferes with the operating frequencies of the AE system [27], subsequently, limits the minimum detectable crack. To solve this problem, multiple sensors are required to guard the noise source or locate the AE event in 1D, 2D or 3D. Generally, several techniques are proposed in literature to facilitate the AE signal interpretation, such as multimodal edge reflection approach, source characterization and probabilistic approach [21; 28; 29]; however, the influence of background noise has not been overcome yet. Besides, waves attenuate in long distances which leads to placing sensors in close proximity in large scale structures and increases the cost of structural monitoring.

Certainly, an intelligent data collecting system can increase the reliability of AE method, by canceling

the effect of background noise and focusing the wave field. The following subsection presents a general overview on the applications of AE to monitor steel truss bridges, as well as assessing the status of existing cracks at a particular location of a structure, which are the interest applications in this research.

2.1.1 The Application of AE Method to Steel Truss Bridges

Steel bridges are subjected to cyclic loads induced by traffic which may create fatigue cracks in bridge members. These fatigue cracks mostly happen in welded structural details. Many steel structures have cracks in their service state. However, if the crack is dormant, stress intensity is below threshold value, and design is damage-tolerant, structures continue to their service, and structural retrofit is delayed. Primary crack growth mechanisms vary in three regimes of the fatigue-crack growth rate curve with low to high energy release rates [30], which influence the detectability of crack growth at its early stages. The AE method has been applied to monitor existing cracks at a particular location (e.g., steel girders, truss members, welds, eyebars) of structures to determine if the crack is propagating or dormant. The common sources of acoustic emission in steel structures are dislocation movement, twinning, phase transformation, crack opening/closing and crack initiation/growth [31; 32; 33].

Some of the earliest studies on crack detection and localization in steel members of bridges were conducted by Kentucky Transportation Research Program (KTRP) to detect cracks in steel members [34; 35]. Until late 1980s, many attempts had been made to apply the AE method to in-service steel structures, but many of them failed due to the problem of background noise (e.g., fretting of bolted or riveted connections). Accordingly, KTRP started using a new AE monitoring system, the Acoustic Emission Weld Monitor (AEWM) created by GARD in 1982. The method was successfully applied on different bridges: (a) the 1-24 over the Tennessee River under normal service loads that five crack

locations were tested successfully, (b) the 1-75 Bridge over the Ohio River that the welded cover plates on the bottom flanges of girders were monitored for crack activities [35]. The issue of background noise led researchers to study the characterizations of AE signals [36]. In a most recent study on John F. Kennedy Memorial Bridge, the AE data was obtained using a custom weatherproof enclosure, robust communication and control methods [37]. Different data analyses including "first-hit channel analysis, planar location and spatial/temporal clustering analysis were used to monitor the crack growth". The results of AE monitoring were further validated with ultrasonic testing and radiography methods. In another study, the structural integrity of a steel bridge under live load condition was assessed using the AE method [26]. They compared the structural behavior for the cases of normal traffic and overloading conditions. Intensity charts were used to estimate the damage severity and quantitative analysis of the data.

In a study by Kosnik et al. [38], two steel Interstate Highway bridges were monitored: a cantilever through-truss and a trapezoidal box girder bridge. Quantitative measurements of AE parameters were collected at suspected crack locations under normal service loads (e.g., live traffic and wind). They noted that an entire bridge may be examined for cracks with only a few AE sensors; however, the acoustic noises from rivets or bolts connections and wind-blown dust make it impractical.

Although some solutions are presented to overcome the shortcomings of the AE method, the combination of design practice and damage detection method has not been employed yet. In this research, the structural design will be tuned within the current design practice such that the major drawbacks of AE method could be overcome.

2.2 Phononic Crystal (PC)

Phonon is a unit of vibrational energy in which a lattice of atoms uniformly oscillates at a single frequency within a crystal. Due to the bonds between the atoms, the displacement of one atom leads to vibration of the next atoms and results in propagation of the vibration wave [39]. Simply, one may consider a mechanical wave made up of particles, known as phonons [40]. The idea of controlling the dispersion relation for phonons led to many researches and applications, by knowing the range of band gaps in which vibration or phonons are restricted [41].

The Phononic crystal (PC), also known as Acoustic Metamaterial (AM), is an artificially manufactured structure with special properties to manipulate elastic wave propagation. It is a periodic elastic composite made up two or more materials with different mechanical properties [42]. When a wave passes through these structures, because of the existence of a band gap, a specific range of frequencies is restricted to propagate. The wave dispersion relation of the material is used to find the frequency band gaps, which can be engineered by designing the unit cell of the material [43; 44]. To form a complete band gap, phonons in both longitudinal and transverse vibrations for all values of Bloch wave vector are forbidden [45]. The most common physical phenomena that result in opening a band gap in PC are known as Bragg's scattering (BS) and local resonances (LR) [46]. The BS happens due to destructive interfaces of an incoming wave through the periodic medium, where the unit cell is usually made of two or more materials, with a periodicity on the order of the wavelength of the incoming wave. However, the PC based on LR mechanism are designed with periodicity smaller than the wavelength, which is preferable in designing PCs inducing low-frequency band gaps. The formation of a band gap in PCs has been studied in many applications, such as sound isolation, acoustic mirrors and waveguides [47; 48; 49; 50].

The development of PC to control the elastic mechanical waves was an analogous concept of photonic crystals which was used to control the electromagnetic waves. Primary studies on two-dimensional PC were started simultaneously by Sigalas and Economou [51] and Kushwaha et al. [52] in early 1990s. Sigalas et al. [51; 53] studied the propagation of elastic waves in 2D and 3D systems composed of solid (or liquid) inclusions positioned periodically within a host solid material. They studied Density Of State (DOS) and band structure for spheres made of *Pb* or *Au* placed periodically in a solid homogeneous host, *Si* or *SiO₂*. In another study, *Au* cylinders embedded in a *Be* host resulted in a narrow band gap, resembling a two dimensional system [54]. The theoretical calculation of acoustic band structure for a periodic elastic composite was presented by Kushwaha [55]. The wave equations of motion for both transverse polarization mode, and mixed longitudinal-transverse mode of vibration were calculated by Kushwaha et al. [52]. They studied the specific case of circular cylinders positioned in a form of square lattice, and the band structure for a case of cylinders made up of nickel embedded in aluminum alloy host, and vice versa, was obtained. In 1995, the first experimental measurement of sound filtering using periodic structures was reported by Meseguer et al. [56]. The structure consisted of hollow stainless steel cylinders periodically arranged in air, using a minimalism sculpture by E. Sempere exhibited in Madrid. The transmission characteristics indicated the attenuation around the frequency of 1.67 *kHz*, which happened due to the multiple interference of sound waves with steel as a scatterer. In 1998, the first experimental observation of ultrasonic full band gap was reported [57]. The structure consists of periodic arrangement of cylindrical holes in an aluminum alloy plate filled with mercury. The propagation of wave within the frequency range of 1000-1120 *kHz* was prohibited in all directions. Later on, in 2001 Vasseur et al. [58] reported experimental and theoretical demonstration of absolute acoustic band

gap in a binary composite medium made up of triangular array of steel cylinders in an epoxy host. The transmission spectra through the plate proved the existence of stop band independent of the direction of wave propagation. They used Plane Wave Expansion (PWE) and Finite Difference Time Domain (FDTD) methods to calculate the band structure and transmission spectra for the designed structure. Most of these studies designed PC plates based on BS mechanism, formed by inclusions embedded in a plate.

In most recent studies, PC plates were designed based on LR mechanism, where resonance of stubs (e.g. cylinders) attached to the surface of a plate were utilized to form a band gap. [59; 60; 61; 62; 63]. This type of PC is also referred to as stubbed plate, which is desirable specially in designing low frequency band gaps to avoid large size of unit cells. Numerical and experimental studies on Lamb wave propagation in stubbed plates are presented by Wu et al. [59]. They investigated the effect of height of the stub on the band gap width in numerical studies using COMSOL Multiphysics software. They experimentally demonstrated a band gap from 114 to 145 kHz formed by a stubbed plate made of aluminum. In another study, Oudich et al. [62] experimentally demonstrated a complete band gap from 1.9 to 2.6 kHz , formed by locally resonant stubs made of silicon rubber periodically attached on the surface of an aluminum plate.

In addition, several studies were implemented to find the band gap in the range of very high frequencies by means of microfabrication and micromachining technologies. A review of the micro phononic crystal devices is reported by Olsson and El-Kady [64; 65].

2.3 MEMS AE Sensors

The precise implementation of AE method primarily depends on the detecting system, specifically, the performance and characterization of the sensors. The AE sensors are conventionally made of bulky piezoelectric materials. These sensors generally operate in resonance, and are designed based on diameter and thickness of the piezoelectric material [66]. With the advancement of micromachining techniques, several studies have been reported on designing AE sensors based on micro-electro-mechanical systems (MEMS).

MEMS are known as the miniaturized mechanical or electromechanical components produced with micromachining techniques [67]. The applications of MEMS technology for fabrication of sensors and actuators have been accompanied by many researchers over the past several decades. A review on ultrasonic transducers made by micromachining techniques is presented by Khuri-Yakub [68]. Taking the advantage of miniaturization, light weight and mass fabrication, MEMS sensors show a great prospective in applications including automotive, communication devices and medical imaging [69; 70].

During the last decade, researchers started studying on the MEMS-based AE sensors which provide a very efficient sensor array due to miniturization (light weight), narrow band response and mass fabrication. Besides, they have the potential to be used in wireless systems [71]. In 1998, Schoess and Zook [72] developed an AE microsensor using a resonant cantilever beam. Afterward, Varadan and Varadan [73] introduced a comb type MEMS sensors for the AE detection to be used in wireless monitoring of aircraft components. Three different transduction principles have been reported in designing MEMS AE sensors: piezoelectric, piezoresistive and capacitive. MEMS transducers working with the principle of capacitance change are well-known. In 2003, Ozevin et al. [74] developed a capacitive type MEMS

transducer that was sensitive to normal surface displacement. The device contained 18 independent sensors with resonant frequencies ranged from 100 kHz to 1 MHz . In another study, a MEMS device was fabricated containing seven capacitive type sensors with the same design [75]. The sensors were capable of detecting the AE events due to crack development in the weld metal. However, their sensitivities were about fifty times less than conventional piezoelectric AE sensors. Later on, the improved design of the same MEMS sensor was tested in laboratory scale and field testing [76]. The sensor could detect the AE events successfully; however, the sensitivity was still less than the commercial piezoelectric AE sensors. With the purpose of designing a more practical sensor and improving the sensitivity, a 3D MEMS device was developed by Greve et al. [77] which contained two in-plane sensors and one out-of-plane sensor. The designed device aimed to be improved in two major mechanical aspects: squeeze film damping and separation of resonance modes. Finite element simulation and characterization measurements of resonant frequency of the sensors are reported in a paper by Harris et al. [78]. In their model, the separation of frequency was not achieved due to limitation of the micromachining process. In another paper by Wright [79], the multi-axis capacitive MEMS sensor was tested, contained an out-of-plane sensors with open grill design to increase the sensitivity and a finger type in-plane sensor. The in-plane sensors were capacitive type in the form of a comb drive, which had higher damping ratio in out-of-plane direction to suppress the unwanted out-of-plane motion.

In 2013, Saboonchi and Ozevin [4] designed and manufactured four different types of MEMS AE sensors on a $1\text{ cm} \times 1\text{ cm}$ device area. The device contained two out-of-plane sensors with transduction principle of capacitance change, and two comb-drive in-plane sensors having transduction principle of area change and gap change. The signal to noise ratio of the designed sensors were improved compared

to the similar sensors designed using surface micromachining method. The performance of these sensors showed better characteristics response and sensitivity at the resonant frequency compared to similar frequency of bulky piezoelectric sensors. The sensors are capable of providing very narrow band response which could be tuned to a specific resonant frequency within the band gap of the PC structure. The MEMS AE sensors designed by Saboonchi et al. [5; 80] are used in this research to be integrated with the perforated PC plate (presented in chapter 3).

2.3.1 Piezoelectric MEMS Sensors

The capacitive MEMS sensors have shown a great potential to be applied in the AE method; however, their major challenge in a field deployment is the requirement of high bias voltage. Unlike the capacitive MEMS sensors, the piezoelectric MEMS sensors are introduced, working with the transduction principle of piezoelectricity, which operate without bias voltage [81]. Besides, they require lower polarization voltage, and need no gap to reach the desired transducer sensitivity. They are made of a thin-film of piezoelectric material, such as lead zirconate titanate (PZT), aluminum nitride (AlN) or zinc oxide (ZnO), sandwiched between two layers of electrodes through micromachining depositions [82; 83].

Recently, the piezoelectric micromachined ultrasonic transducers (PMUTs) are investigated as an alternative to conventional piezocomposite ultrasonic transducers due to their unique features [84; 85; 86]. Various methods have been widely applied to study and characterize PMUTs. For instance, Feng et al. [87] presented a MEMS AE sensor with a cantilever sensing structure in which a layer of PZT was deposited on the cantilever for AE sensing. Sommer et al. [88] utilized modified high aspect ratio micromachining (HARM) technology to fabricate MEMS AE sensor working in the frequency range of

100-130 kHz . Lu et al. [89] denoted short-range and high resolution ultrasonic imaging using PMUTs array. Massimino et al. [90] applied complete multi-physics modeling using finite element method to verify the mechanical and acoustical responses for air-coupled PMUTs, which were tuned to 100 kHz resonant frequency. The numerical models considered the residual stress induced during fabrication process, and proper modeling of air along with coupling between different fields. In another study, Shelton et al. [91] produced 5×5 array of complementary metal-oxide-semiconductor (CMOS)-compatible PMUTs excited at 220 kHz resonant frequency by using AlN as the active piezoelectric layer.

In this study, a set of piezoelectric MEMS (Piezo-MEMS) sensors are designed and characterized to be utilized for AE detection and ultrasonic testing. The resonant AE sensors include low-frequency (LF) design tuned to 40 kHz and high-frequency (HF) design tuned to 200 kHz . The sensors are manufactured using PiezoMUMPs by MEMSCAP foundry. The PiezoMUMPs process is a 5-masks level SOI patterning and etching process, which includes deposition of 0.5 μm AlN to form piezoelectric layer [92]. Detailed description of the design process and characterization of the Piezo-MEMS sensors are presented in chapter 5.

CHAPTER 3

PERFORATED PCS TUNED TO STRUCTURAL DESIGN AND DAMAGE DETECTION

The content presented in this chapter has been partially published in the proceeding of the SPIE 2016 conference of Nanoscience + Engineering as "Integration of periodic structure and highly narrow-band MEMS sensor to enhance crack detection ability in steel structures" with my research advisor Dr. Ozevin as the co-author [3].

3.1 Introduction

The most common physical phenomena that result in opening a band gap in PCs are known as Bragg's scattering (BS) and local resonances (LR) [46]. The BS happens due to destructive interfaces of an incoming wave through the periodic medium, where the unit cell is usually made of two or more materials, with a periodicity on the order of the wavelength of the incoming wave. However, the PC based on LR mechanism are designed with periodicity smaller than the wavelength, which is preferable in designing PCs inducing low-frequency band gaps. Two types of PCs based on the mechanism of band gap formation are studied in this research: (a) periodic perforated plates that works based on BS mechanism, and (b) surface stubbed plates that works based on LR in unit cells (as illustrated in Figure 2 (a) and (b), respectively). Existing structures exhibit some localized periodicity such as equally spaced bolts in gusset plates with 2D periodicity as shown in Figure 3. Currently, perforation locations of bolts at connections are placed based on stress distribution and minimum/maximum spacing requirements.

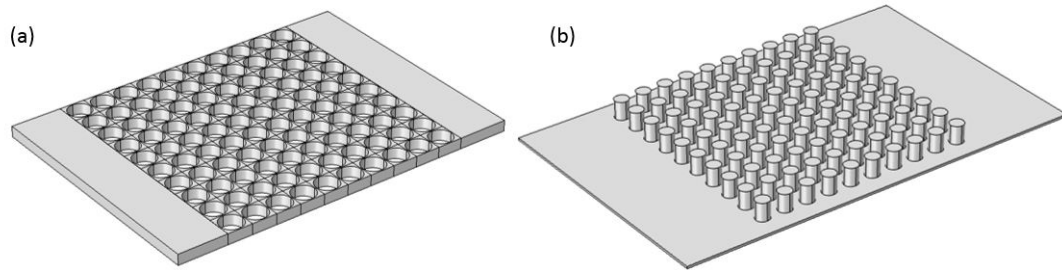


Figure 2. Two types of phononic crystal plates: (a) periodically perforated plate, (b) surface stubbed plate

The design can be integrated with the damage detection philosophy such that we can predict the damage presence through damage-induced imperfection and wave redirecting between periodic lines. In this chapter, the periodically perforated plates are investigated which resemble the periodic arrangement of bolts in a connection plate of a bridge.

The components of the proposed SHM system include: a PC plate to provide wave guiding and the MEMS AE sensor for AE sensing. The perforation location of the bolts in a connection plate can be designed strategically, based on the design of a PC plate. The dispersion curve of the PC plate is used to find the range of frequency band gap and the MEMS AE sensors tuned to stop band of the periodic system will be used for AE sensing. The proposed integration scheme is shown in Figure 4. In the following section, numerical simulation of the PC plate is presented to tune the geometry for the

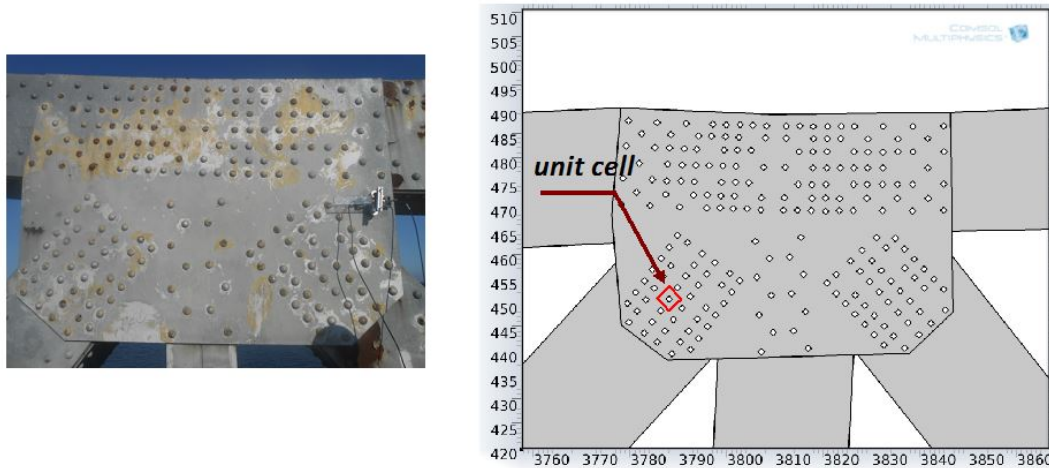


Figure 3. 2D connection plate with bolts exhibiting some periodicity

desired range of frequency. The capacitive type MEMS AE sensors designed by Saboonchi et al. [5] are employed for the experimental tests to show the advantage of narrow band frequency response.

3.1.1 Numerical Studies

The perforated PC plate is numerically studied using COMSOL Multiphysics software. Two approaches are mainly applied in literature to study the band gap developed by the periodic behavior of PC plates: (a) the unit cell analysis and (b) the transmission loss analysis. The first approach results in the dispersion curve of the PC plate using the unit cell of the structure. First, the unit cell analysis is implemented to study the effect of different materials and dimensions on the dispersion curve of the PC structure. The dispersion curve is used to identify the frequency band gap ranges where no phonon

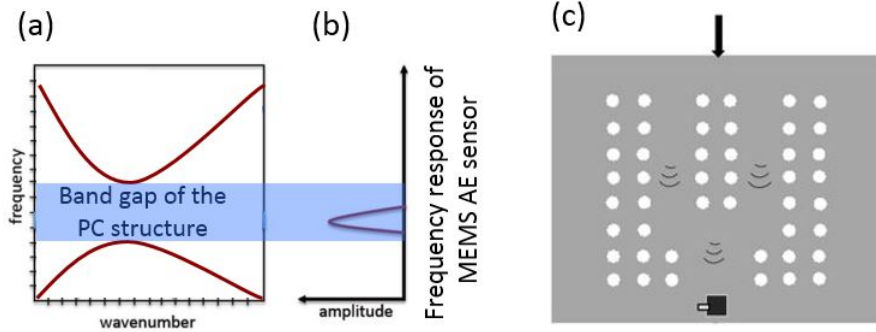


Figure 4. Integrated behavior of the periodic perforated plate and MEMS AE sensor

is allowed to propagate through the media. This phenomena can be seen as a significant attenuation in the transmission spectrum. Therefore, a second numerical study is adopted to study the transmission of waves through an array of unit cells [93]. The wave propagation through the designed geometry is studied experimentally to demonstrate the transmission loss at the designed band gap.

3.1.1.1 Unit Cell Analysis

The perforated PC plate is composed of periodic arrangement of cylindrical holes inside a plate. Due to the periodicity, only a unit cell of the structure is modeled and periodic boundary conditions are applied on the sides of the unit cell, as shown in Figure 5. The periodic boundary conditions are based on the Bloch theorem, in which displacements on the sides of the unit cell are related as

$$u_{output} = e^{-ik_F(r_{output}-r_{input})} u_{input} \quad (3.1)$$

where u represent the displacement and according subscripts refer to the sides of the unit cell where periodic boundary conditions are applied, r is the position vector, and k_F is the wave vector [94].

The three-dimensional model of the unit cell is prepared in COMSOL, as shown in Figure 6 (b), and eigenfrequency study is selected. The wave vector value is swept to cover the edges of the first Irreducible Brillouin Zone (IBZ). The first IBZ related to the square lattice is illustrated in Figure 6 (c), which specifies the highest symmetry points of the wave vector in x and y directions: Γ, X, M [95; 96]. Free tetrahedral elements are used to mesh the models. In order to achieve acceptable accuracy as well as high efficiency, the mesh resolution is kept at least 20 elements in one wavelength of selected frequency [97; 98].

The dimension of the unit cell and the material properties affect the dispersion curve of the PC. Here, the material is selected as structural steel, which is a common material used in metallic bridges. The geometrical parameters of the unit cell, such as lattice size, thickness of the plate and diameter of the holes, affect the range of frequency band gap. The geometrical parameters are iterated to find the desired band gap range near 60 kHz . Several trials were conducted to find the proper geometrical parameters. It is observed that the thickness of the plate has a significant influence to the width of the frequency band gap. The ideal perforated PC design is selected and the results are depicted in Figure 6. Every point at a selected wave vector represents an eigenmode of the PC plate. It is apparent that there is a range of frequencies that no eigenmode exists, indicating the band gap, starting from 51 kHz to 74 kHz . The final geometry is formed by cylindrical holes with diameter of 26 mm periodically placed in a 12 mm thick steel plate with lattice size of 28 mm .

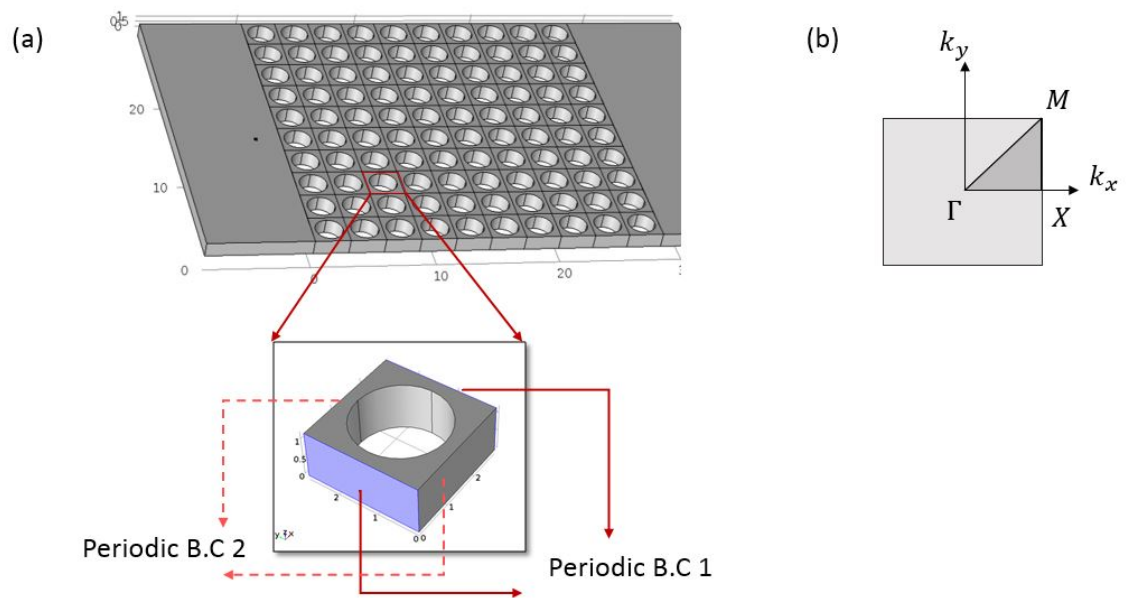


Figure 5. (a) Unit cell of the periodic structure, showing periodic boundary conditions applied on all sides of the unit cell, (b) first IBZ

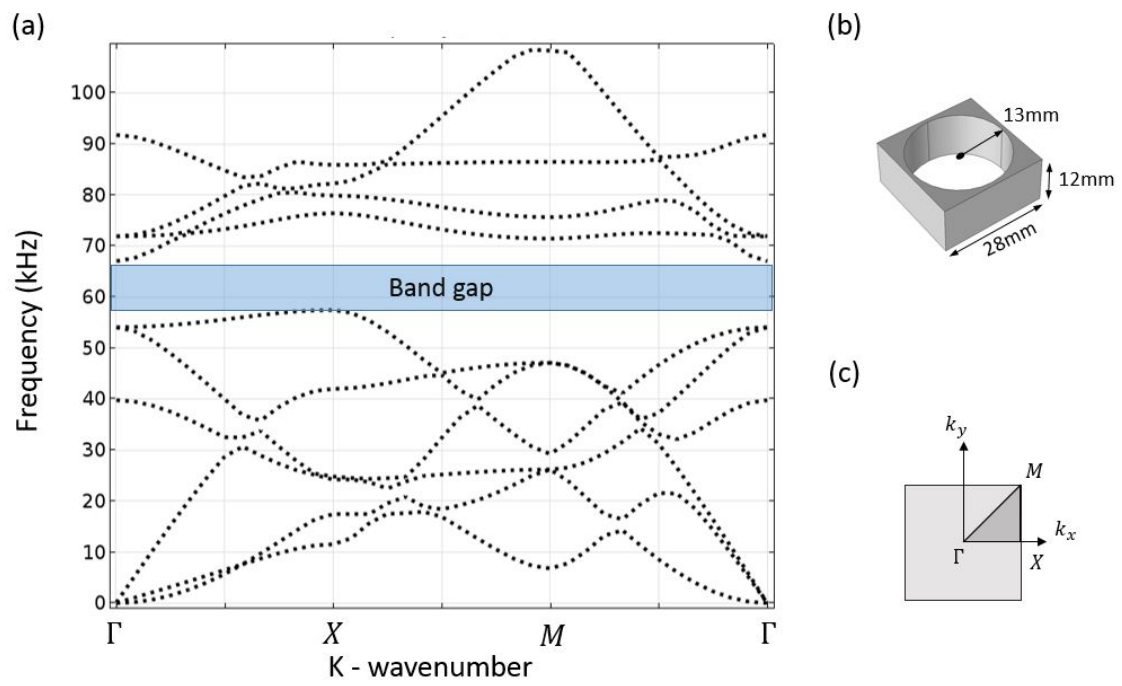


Figure 6. (a) Dispersion curve of the perforated PC indicating the band gap near 60 kHz, (b) the unit cell of the PC illustrating the dimensions of the final design, and (c) the first IBZ of the square lattice

3.1.1.2 Transmission Loss Analysis

To simulate the transmission loss of the wave propagation through the PC plate, a finite number of periods are modeled. A supercell, made of ten unit cell in x-direction, is modeled in COMSOL, as shown in Figure 7(a). A two dimensional analysis is performed by applying an incident boundary load in x-direction. Perfectly Matched Layers (PML) are applied at two end of the model to prevent reflections from the boundaries. A frequency analysis is performed to span a range of frequencies and the transmission loss is obtained considering the displacement of the nodes on the input and output sides of the supercell. Transmission loss, TL , is calculated using the following equation:

$$TL(dB) = -20\log\left(\frac{u_{output}}{u_{input}}\right) \quad (3.2)$$

where u_{input} is the displacement on the left side of the super cell, where the load is applied, and u_{output} is the displacement on the right side of the supercell.

The transmission loss through the array of unit cells is obtained (Figure 7(b)) and the dispersion curve of unit cell is depicted next to it to compare the results. A significant drop in amplitude in transmission spectrum confirms the existence of the band gap obtained by the unit cell analysis.

The displacement fields for two cases, inside and outside the range of frequency band gap, are presented in Figure 8. In order to have a better representation of the displacement field, an array of five supercells in y-direction are located next to each other. The frequency of 60 kHz is in inside the band gap region, as shown in Figure 8(a), the displacement field on the right side of the supercell at this frequency is near

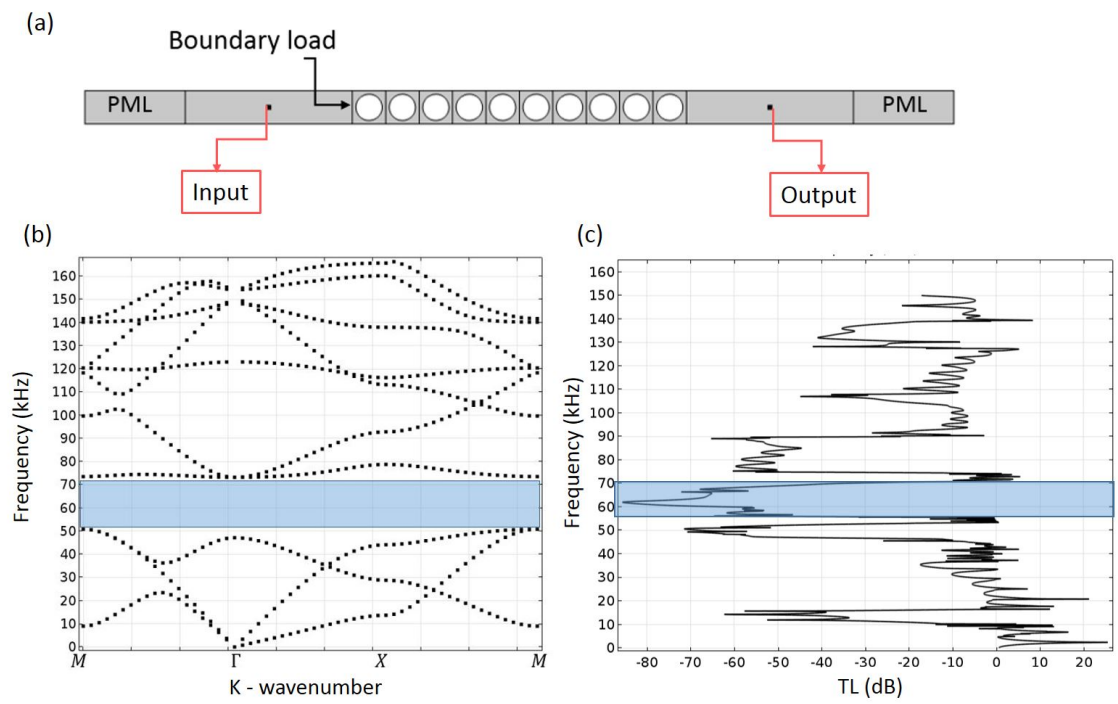


Figure 7. (a) Supercell geometry, (b) transmission loss through the supercell, (c) dispersion curve of the unit cell

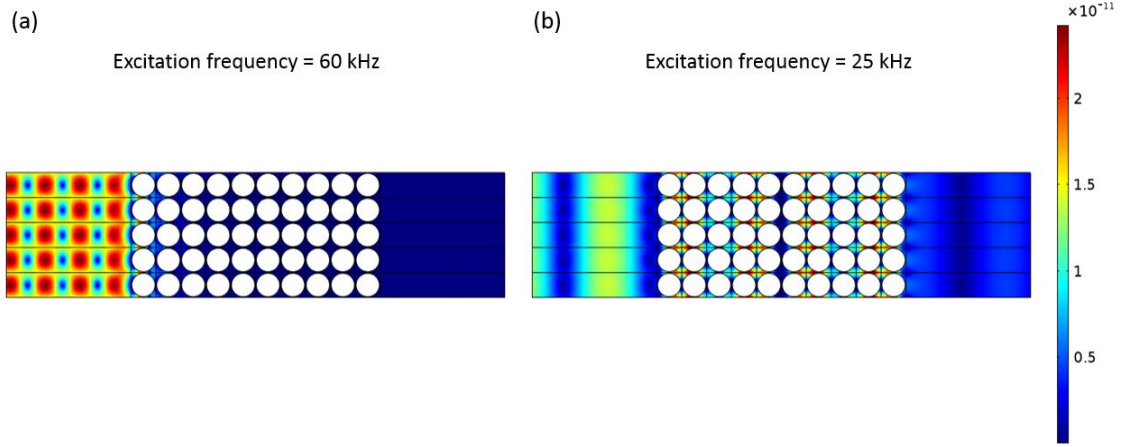


Figure 8. (a) Displacement field at the frequency of 60 kHz and (b) displacement field at the frequency of 25 kHz

zero. Figure 8(b) shows the displacement field at the frequency of 25 kHz (outside the band gap), which is non-zero.

3.2 MEMS AE Sensor

The elastic wave propagation through the PC structure is studied experimentally, and the MEMS AE sensors designed by Saboonchi et al. [80; 5] are implemented as the receiving sensors. The MEMS device contains four different designs. Two out-of-plane sensors with the resonant frequency of 60 kHz (S1) and 150 kHz (S2) are used in this section. The transduction principle of the sensors is capacitance change, and they are manufactured using Multi-User-MEMS-Processes (MetalMUMPs). Each sensor is made up of multiple cells connected in parallel as shown in Figure 9. Figure 9 (c) shows the the

frequency domain spectra of the received signal by of S1 and S2, indicating the narrow band response of the MEMS AE sensors.

3.2.1 Experimental Results

To validate the finite element results of the PC plate, the one dimensional PC (supercell) is manufactured based on the geometrical parameters obtained in the numerical studies. Subsequently, a steel plate containing a square array of ten holes with radius of 13 *mm* and lattice constant of 28 *mm* is fabricated. In order to compare the results with a reference, a steel plate of the same size without any holes is also prepared. Two excitation frequencies are selected, one in the frequency range of the band gap and the other one outside the band gap. Based on the numerical studies, it is expected that 60 *kHz* is in the band gap. Therefore, an actuator (R6 piezoelectric sensor manufactured by Mistras Group Inc) is attached to the left side of the sample to generate sinusoidal wave with the peak frequency of 60 *kHz*. The S1 (MEMS AE sensor with resonance frequency response of 60 *kHz*) sensor is attached to the other end of the sample. The sensors are connected to the Micro-II Digital AE system manufactured by Mistras Group Inc. The experimental setup is shown in Figure 10. The experiments are repeated using R15 as the actuator (exciting 150 *kHz* frequency) and the S2 sensor (150 *kHz* frequency response) as the receiver.

The time domain response of the S1 sensor for PC and the reference plate are presented in Figure 11(a). The signal received from the PC plate has very low amplitude. A MATLAB script is used to calculate their frequency spectra. The results are shown in Figure 11(b). The amplitude of 60 *kHz* frequency significantly decays due to the band gap of the PC plate.

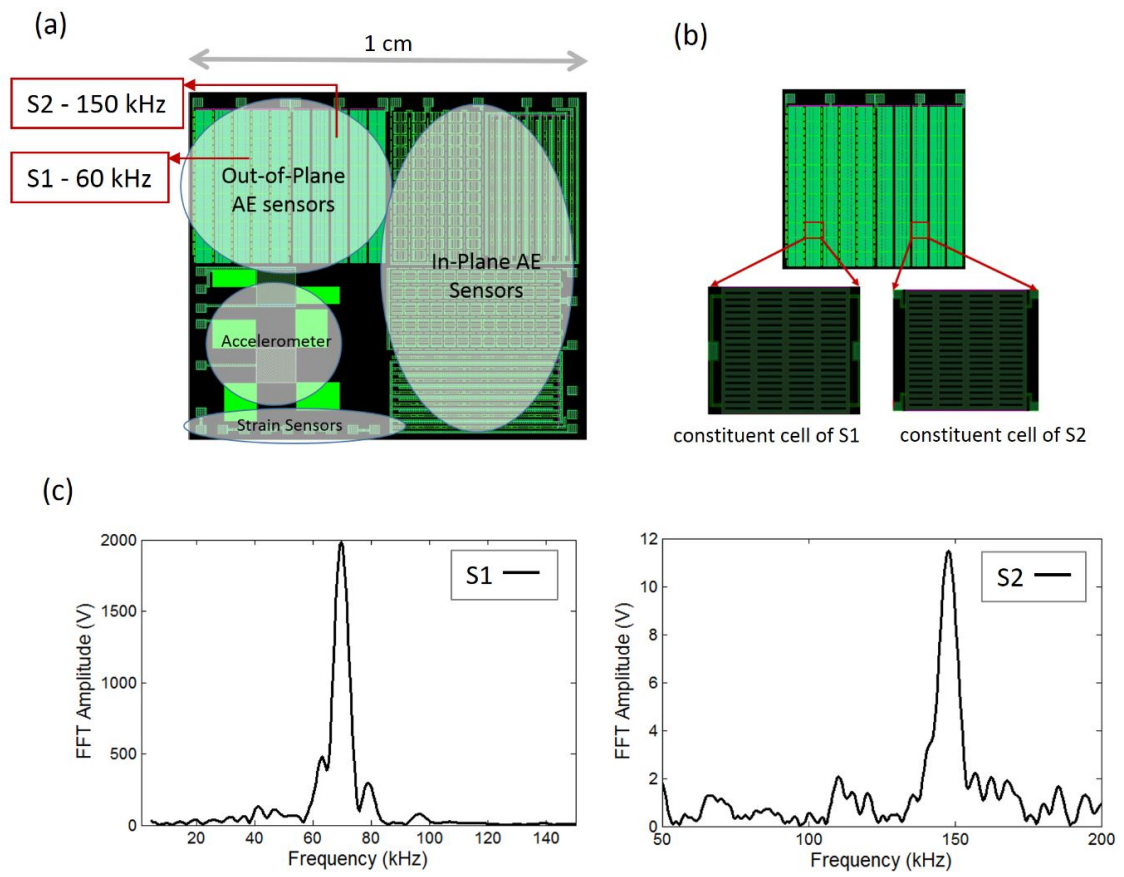


Figure 9. (a) The overview of MEMS device designed by Saboonchi, (b) the constituent cell of each type of sensor, and (c) the frequency domain spectra of the received signal by of S1 and S2

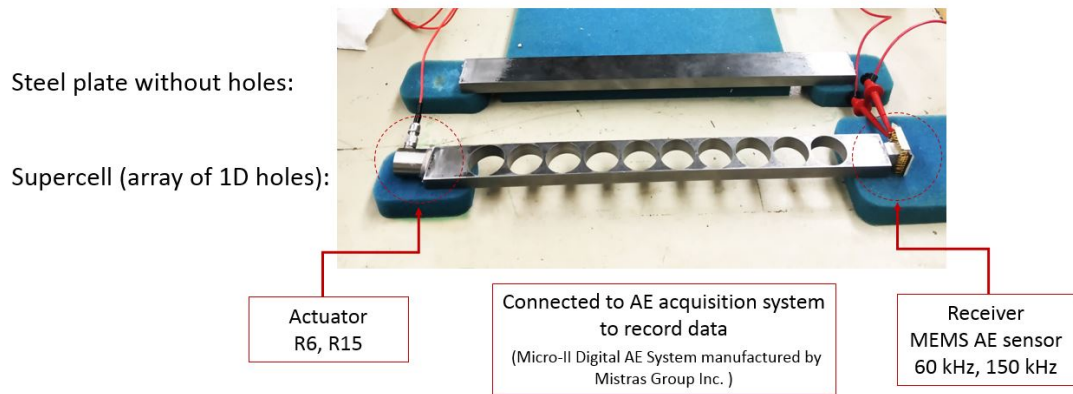


Figure 10. Experimental setup for testing one dimensional PC plate

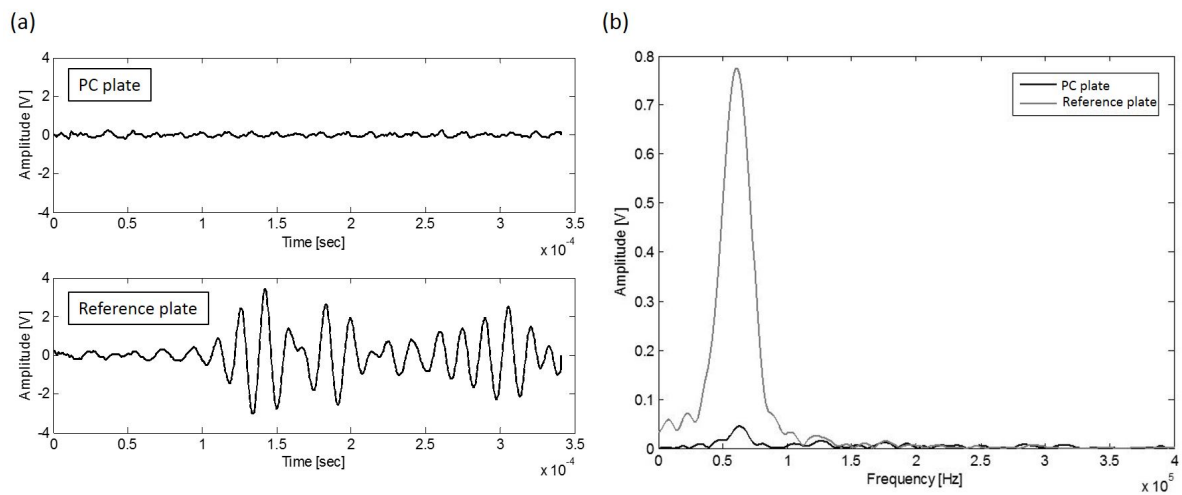


Figure 11. Experimental results, (a) time histories, and (b) frequency spectra for 60 kHz excitation

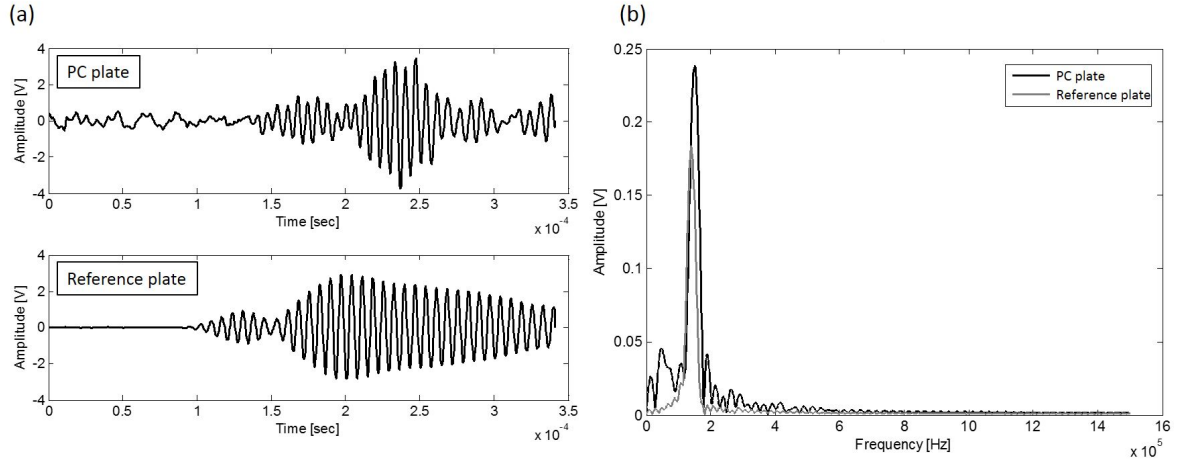


Figure 12. Experimental results, (a) time domain response, and (b) frequency domain response for 150 kHz excitation

The time domain signals and frequency spectra using the S2 sensor are shown in Figure 12. While the presence of the holes in the plate influences the waveform signature, the amplitudes of the PC and the reference plates are similar. The frequency spectra of two plate at 150 kHz shows that the wave outside the band gap propagates through the PC plate.

In order to have a better comparison, the frequency spectra of two MEMS sensors for each plate are plotted together. They are normalized with respect to the reference plate. Figure 13(a) shows the results for the reference plate. Apparently, waves with both frequencies propagate through the reference plate. Figure 13(b) shows the results for the PC plate. The amplitude of 60 kHz excitation is near zero while

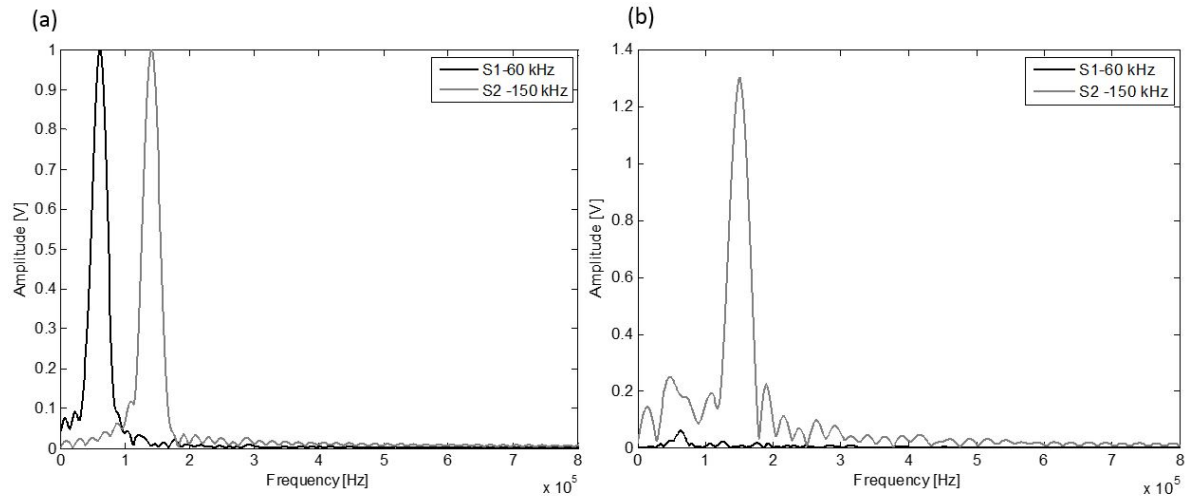


Figure 13. Frequency spectra of (a) the reference plate, and (b) the PC plate

the amplitude of 150 kHz is similar to the reference plate. The PC design blocks the propagation of 60 kHz frequency which is within the band gap range (as shown in Figure 7).

3.3 Summary

In this chapter, the possibility of designing the connection plate of bridges based on analogy to PCs is studied. The perforated PC structure is sought to resemble location of bolts in connections of steel structures. We aimed to design the perforation locations to guide the wave energy released by newly formed cracks to the location of the AE sensors. The numerical models are used to study band gap of the perforated PC plate. The geometry is designed such that it generates a band gap near 60 kHz to operate with MEMS AE sensors tuned to the resonant frequency of 60 kHz . The dispersion curve of

the designed PC provides a band gap from 51 kHz to 74 kHz . It is observed that the band gap range is highly dependent on the geometrical parameters of the structure. The 1D PC plate is fabricated based the dimensions found in numerical studies. The integrated behavior of the current PC design with MEMS AE sensor is experimentally studied. The experimental results of the one dimensional PC plate validate the existence of a band gap near 60 kHz frequency. However, the current designed geometry of the PC plate is not practical for design of a connection plate used in steel structures. Generally, to obtain an acceptable range of band gap, high filling factor is required, which results in holes with very close distances. Therefore, the geometry obtained based on Bragg's scattering phenomenon is not practical for designing gusset plates of bridges. In next chapter, PC plates based on local resonance phenomenon are introduced, which provides more practical geometries to be applied in structures.

CHAPTER 4

NOISE ISOLATION THROUGH PHONONIC CRYSTALS

The content presented in this chapter has been published at the journal of Civil Structural Health Monitoring as "Noise Isolation with Phononic Crystals to Enhance Fatigue Crack Growth Detection using Acoustic Emission", with my research advisor Dr. Didem Ozevin and Ph.D. student Amir Mostavi as the co-authors [1]. Also, parts of the results presented in this chapter is already drafted and will be partially published in the journal as "An Approach towards the Repeatability of Acoustic Emission by Noise Isolation through Phononic Crystals" with my research advisor Dr. Ozevin and Ph.D. student Amir Mostavi as the co-authors.

4.1 Introduction

One of the major challenges of AE method is the influence of secondary sources unrelated to crack growth that interfere with the primary AE events. These secondary sources includes background noise, friction emissions and fretting of bolted connections and etc, which complicate the data processing to separate the relevant data. As described in background literature, many metallic structures have cracks in their service state, which need to be monitored to determine if the crack is propagating or dormant. In current practice, multiple sensors are required to guard the noise source or locate the AE event; however, an intelligent data collecting system can increase the reliability of AE method, by canceling the effect of background noise and focusing the wave field.

In this chapter, noise isolation to monitor a particular location in plate-like structures is developed using two-dimensional PCs such that a single AE sensor is sufficient to monitor the crack activity. The proposed PC is made of cylindrical stubs made of aluminum that are designed to block 150 *kHz* signals. This is the typical frequency used to monitor cracks in metallic structural components which are prevalent in civil and aerospace structures. The designed PC plate works with the mechanism of local resonances in stubs to form a band gap at the desired range of frequencies. The efficiency of the proposed method is demonstrated experimentally through the application of stubbed plate in fatigue testing of compact tension (CT) specimens. The stubs are attached to the CT specimen, except in the path between crack growth direction and sensor position. The developed approach eliminates any post-processing filtering, which typically depends on experimental setup and limits the applicability of experimental results to other test conditions. First, the application of the proposed method is illustrated through an example of AE monitoring of civil structures. Then, numerical studies are presented including the simulation of the proposed PC structure and the CT specimen. The performance of the proposed PC structure is evaluated experimentally through the fatigue testing of CT specimens. Furthermore, the effectiveness of noise isolation with the stubbed PC on the repeatability of AE method for correlating damage characteristics with AE features is studied. In the end, the summary of this chapter is presented.

4.2 Illustration of the Proposed Approach in Steel Structures

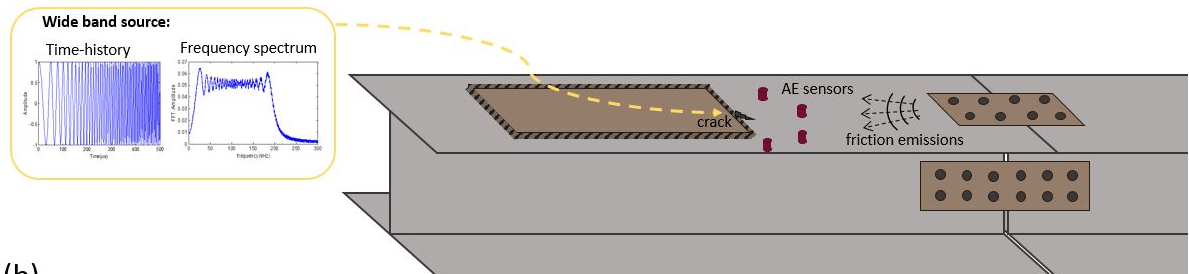
The proposed method is demonstrated through an example of AE monitoring of a civil structure. Many metallic civil structures have cracks in service state which could be found during the maintenance procedure. It is important to monitor the crack activity to ensure that it is dormant. Consider an I-beam as shown in Figure 14(a) with cover plate to increase the bending capacity and splice connection with

bolts, that has a crack at the weld of the cover plate. In current practice, multiple sensors are required around the crack area to monitor the crack activity. If the crack grows, the dynamic motion produces a wide band source that initiates the propagation of elastic waves to be detected by the AE sensors. Typically, resonant type sensors are used for the source localization. However, the friction emissions released from the bolted connection (in this case, the splice connection) negatively influence the received data by the AE sensor. In order to successfully monitor the crack activity, several AE sensors are required. We propose to apply a PC structure to block the unwanted emissions at the resonant frequency of the sensor such that only a single sensor is sufficient to control the crack activity. The PC structure is tuned to the resonant frequency of the AE sensor. Figure 14(b) demonstrates the application of the PC to block the friction emissions coming for the bolted connection (the incoming waves are reflected back).

4.3 Numerical Studies

The PC plate is numerically studied using COMSOL Multiphysics software. Two approaches, similar to Chapter 3, are applied: the unit cell analysis and the transmission loss analysis. First, the unit cell analysis is implemented to study the effect of different materials and dimensions on the dispersion curve of the PC structure. Then, the wave propagation through the proposed geometry is studied to demonstrate the transmission loss at the designed band gap. Additionally, the CT specimen is modeled to have an estimation of the maximum applicable load that initiates the crack growth. The maximum stress value at the selected load range and cyclic frequency are then compared with the S-N curve of the Aluminum 7075 to find the required cycles to grow the crack approximately 7 mm.

(a)



(b)

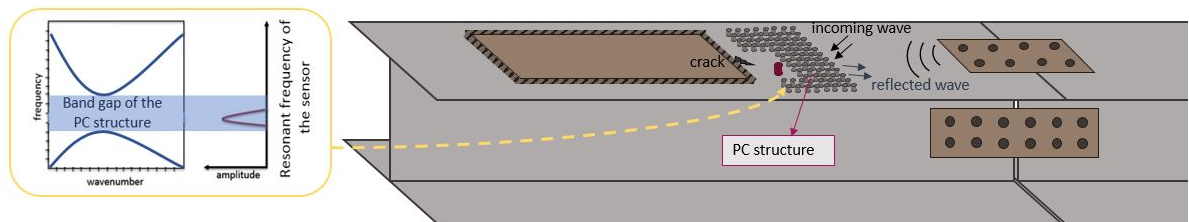


Figure 14. An example of application of the proposed method illustrating the (a) friction emissions generated at the bolted connection and (b) the incoming waves are reflected using the PC structure

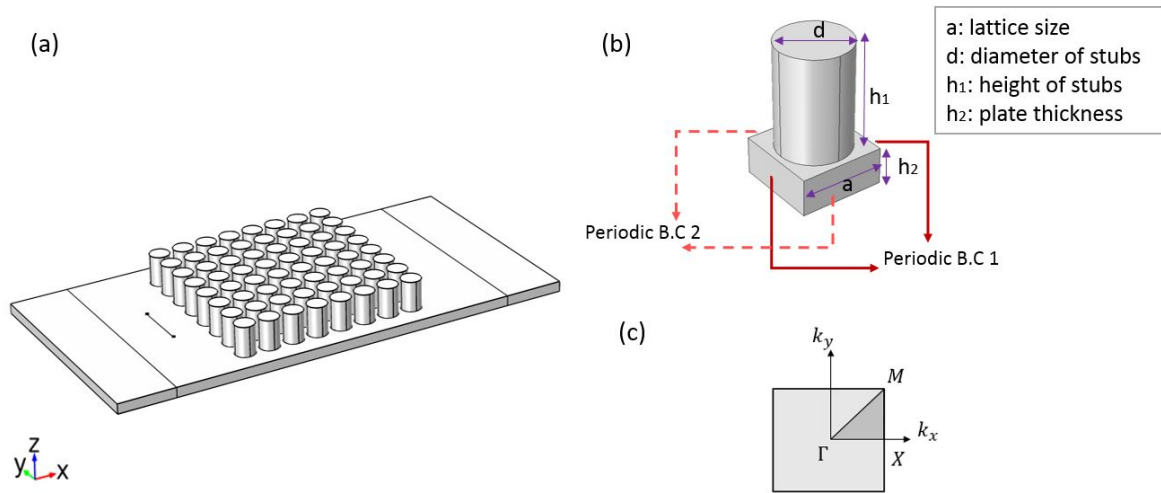


Figure 15. The unit cell analysis of the PC structure, (a) periodic stubbed plate (b) the unit cell of the PC structure, presenting periodic boundary conditions applied on sides of the unit cell, (c) The first IBZ

4.3.1 Phononic Crystal Models

Unit cell Analysis

The PC structure is composed of periodic arrangement of stubs that are attached on the surface of the aluminum plate, as shown in Figure 15 (a). Due to the periodicity, only a unit cell of the structure is modeled and periodic boundary conditions are applied on the sides of the unit cell. It is again a square lattice based on the first IBZ as depicted in Figure 15(c). The detailed description of the unit cell analysis is presented in numerical studies of Chapter 3. The three-dimensional model of the unit cell is prepared in COMSOL, as shown in Figure 15 (b).

The effects of geometrical variables and material properties on the position and width of the band gap have been studied in literature. In general, increasing the ratio of d/a (e.g. diameter of the stub to lattice size) increases the width of the band gap. More details on the effect of filling factor on the width of the band gap can be found at [99]. Also, increasing the height of the stubs increases the width of the band gap up to a specific value and then decreases the width of the band gap. In a study by Wu et al. [100], the evolution of band gap in periodic stubbed plate was discussed. They described the mode transformation in the dispersion curve as the height of the stubs changed. Here, we optimized the band gap width, considering the size restrictions to fit sufficient number of stubs in the CT specimens. The plate thickness of CT specimen is controlled by the ASTM E647-15 standard, which is 3.175 mm (0.125 in). The starting point to select the size of the stubs is based on the wavelength in order to form a band gap that includes 150 kHz . Then, the size of the stubs is varied to tune the band gap to the desired range of frequencies. The geometric variables are the stubs' diameter and height, and the lattice size. The effect of increasing the diameter and height of stubs on the band gap position and its width is studied and presented in Figure 16. Increasing the diameter of the stub (d), increases the width of the band gap frequency range (Figure 16 (a)). As the height of the stubs increases, the band gap starts to form between the third and fourth bands up to a specific ratio of height to lattice size and decreases afterwards. Then, at the ratio of 0.6, the band gap starts to form between sixth and seventh band, as well as the ninth and tenth band. As shown in Figure 16 (b), the maximum of the band gap width is formed when height of stubs is equal to the lattice size.

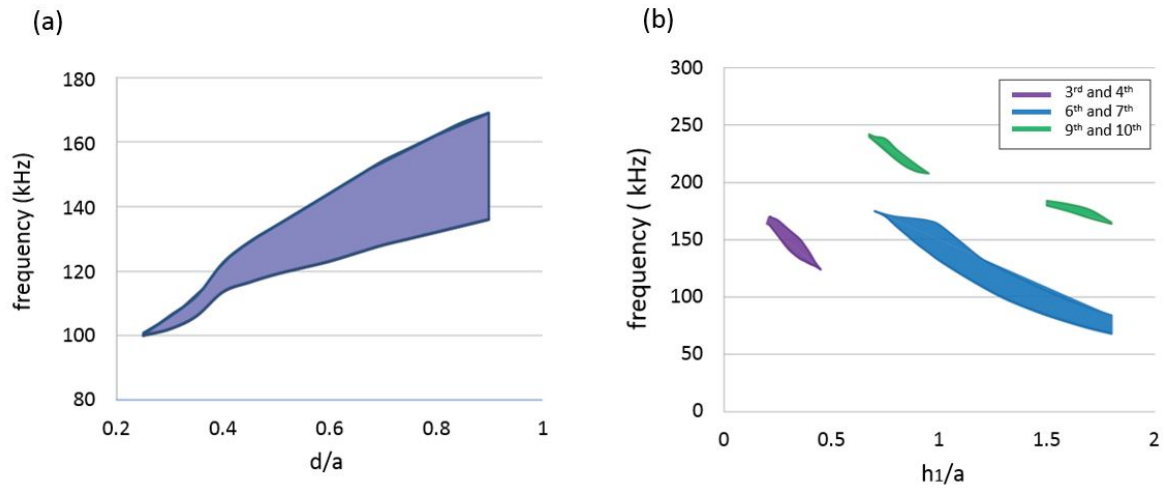


Figure 16. The effect of (a) diameter and (b) height of stubs on the band gap frequency range

The final geometry is made of aluminum 7075 cylinders, with diameter of 7.2 mm and height of 9 mm, placed periodically with lattice size of 9 mm. The band gap diagram of the designed geometry is presented in Figure 17.

Transmission Loss Analysis

A row of stubs is modeled in three-dimensions while symmetry boundary is applied on the side of the beam to form the periodic stubbed plate. The size of the CT specimen restricts the maximum number of stubs to be placed, as a result, only five rows of stubs are modeled. Time dependent study is selected, and a 5-cycle excitation load with central frequency of 150 kHz is applied in z-direction, as illustrated in Figure 18. Free tetrahedral elements are used to mesh this model. As a general rule for time-domain numerical simulations, the mesh resolution is kept at least 20 elements in one wavelength.

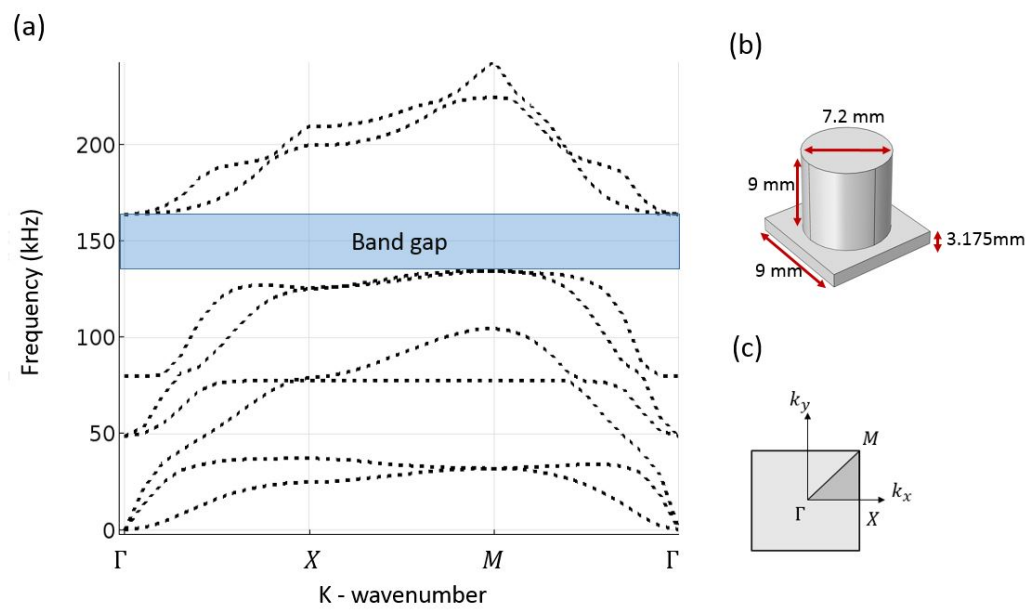


Figure 17. (a) Dispersion curve of the PC plate, indicating the band gap near 150 kHz, (b) the unit cell of the PC illustrating the dimensions of the final design, and (c) the first IBZ of the square lattice

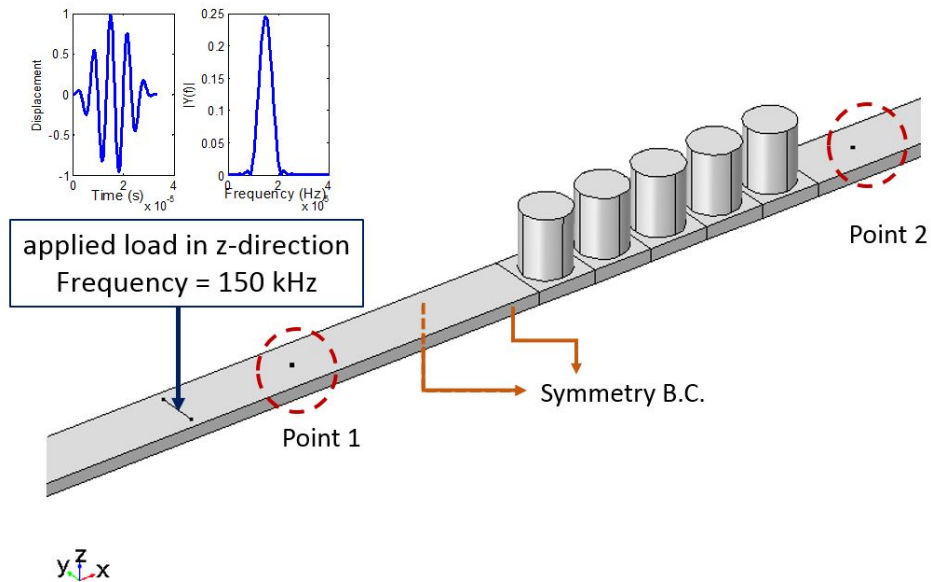


Figure 18. The transmission analysis

The z-components of displacements at points 1 and 2 are extracted, and the waveforms are shown in Figure 19. The amplitude of the waveform decreases significantly at point 2, which indicates blocking of the propagation of 150 kHz frequency through the stubs.

The first pack of the waveform, containing the 5-cycle, is selected to calculate the frequency spectrum of the signal, as presented in Figure 19 (b). The z-components of the displacement field at different times of study are shown in Figure 20. The incoming wave and its reflection are clearly depicted. It is concluded that the local resonance phenomenon is the reason of the band gap formation, as the energy is dissipated through the stubs.

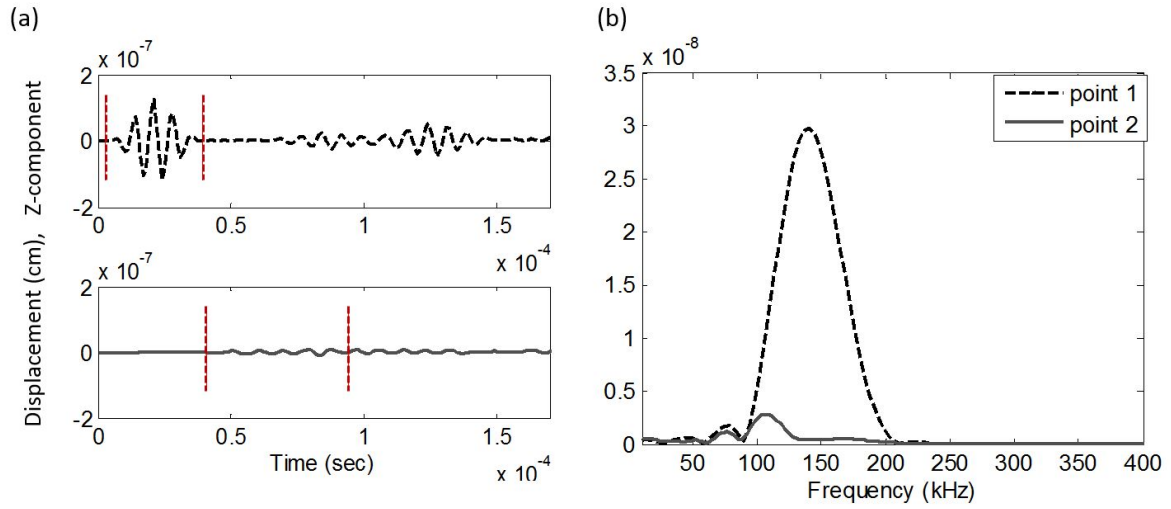


Figure 19. (a) The waveforms extracted at points 1 and 2 (z-component of displacement field), (b) the frequency spectra of the time history waveforms

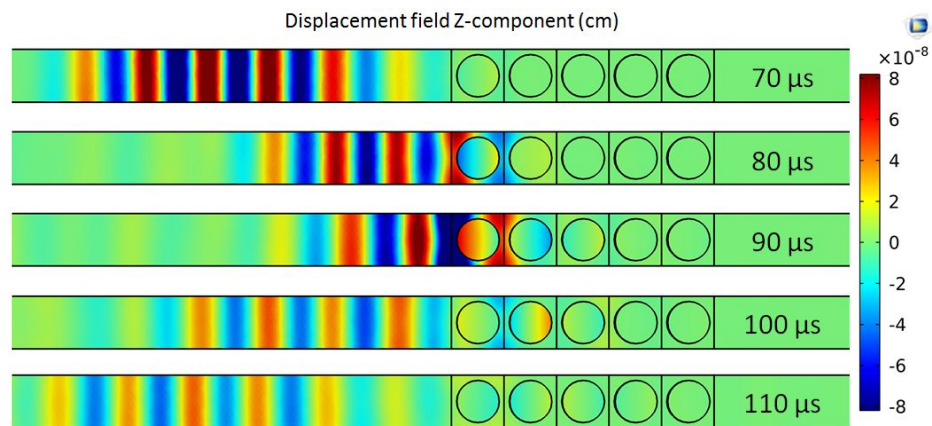


Figure 20. The z-component of displacement field (cm) at different time of study

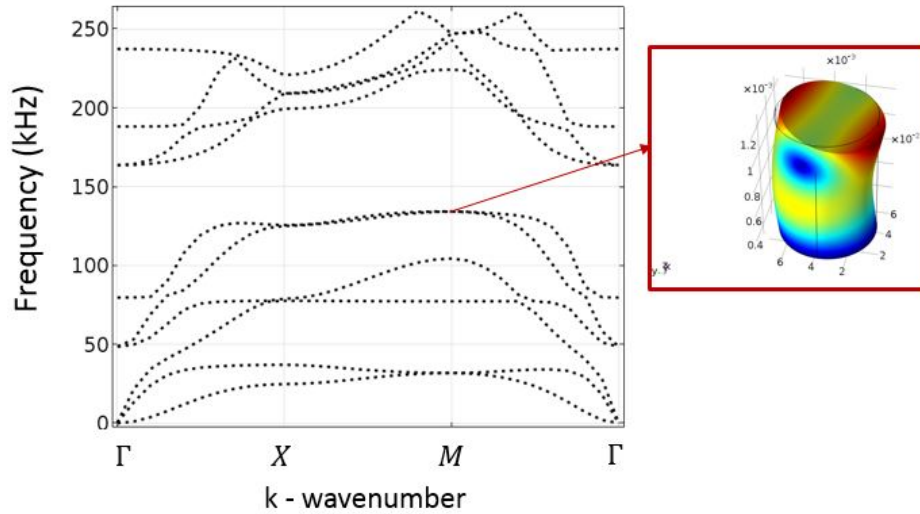


Figure 21. Deformation of the stub at the edge of the band gap

To further investigate the source of band gap formation at 150 kHz excitation, we studied the deformation of the individual stubs at the edge of the band gap. The deformation of the stub at the edge of the band gap is extracted from the unit cell analysis (Figure 21). The band gap starts to form at the sixth band, which demonstrates a flexural bending in the stub. A frequency domain analysis of the stubbed plate is performed to simulate the propagation of the wave through the path between the stubs. The geometry as shown in Figure 22(a) is modeled in three dimensions. An out-of-plane force with central frequency of 150 kHz is applied and the displacement field is evaluated. Comparing the displacement field resulted from the frequency domain study at 150 kHz excitation (Figure 22(b)) with the deformation of the stub at the lower edge of the band gap (figure Figure 21), it is concluded that the band gap is formed due to the resonance of the individual stub.

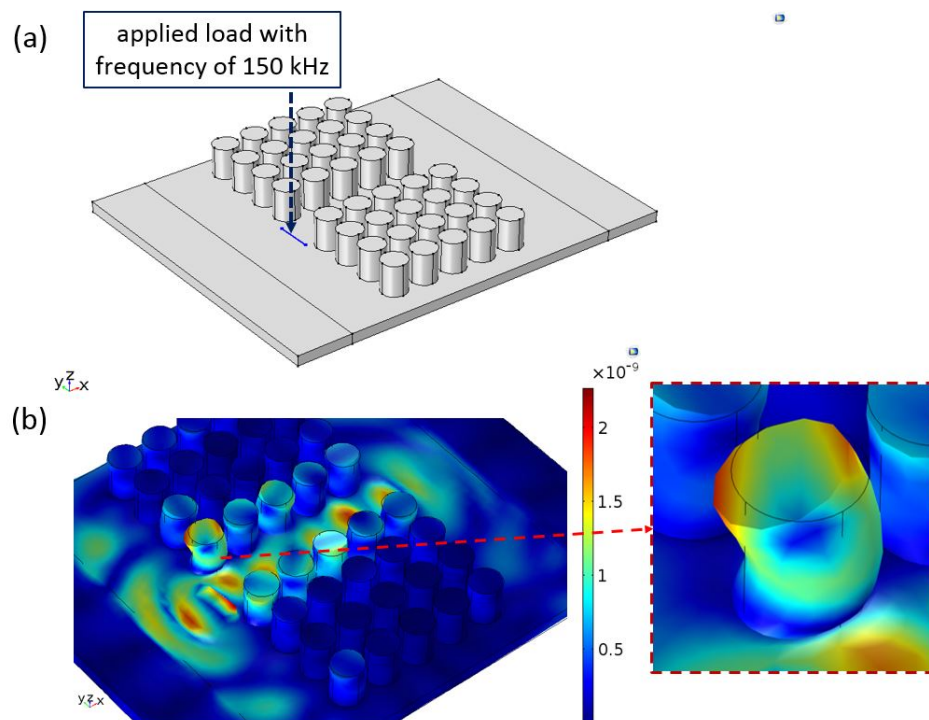


Figure 22. The results of frequency domain analysis demonstrating the wave propagation through a path between the stubs, (a) three-dimensional geometry modeled in COMSOL, (b) the deformation of the stubs at 150 kHz excitation

4.3.2 CT Specimen Model

Standard CT specimens are machined out of 3.175 mm (0.125 in) thick aluminum 7075-T6 plate according to the ASTM E647-15 standard, as shown in Figure 23(a). Numerical model and the S-N curve of aluminum 7075-T6 reported in literature are used to have an estimate of the required number of cycles to initiate the fatigue crack at the selected load range and fatigue frequency [101]. Based on the S-N curve, the load range leading to 300 MPa at the notch tip results in crack initiation in the specimen after about 8000 cycles. The CT specimen is modeled in COMSOL to determine the maximum stress induced at the notch tip as well as the stress intensity factor (K), to identify if the applied load is sufficient to initiate and grow the crack. When K is equal to the critical fracture toughness of the material, K_{Ic} which is a material property, fracture occurs [102]. The J-integral method is used to calculate K , by defining a two-dimensional line integral along a contour defined around the crack tip. The CT geometry, as shown in Figure 23(b) is modeled in two dimensions to find the maximum stress at the crack tip. A stationary study is performed and free triangular is chosen to mesh the geometry. The predefined extra fine mesh size in COMSOL was selected to mesh the area around the crack tip, while fine mesh size was selected to mesh the rest of the geometry. A contour is defined surrounding the crack tip in order to calculate the J-integral, as shown in Figure 23(b). The J-integral is related to stress intensity factor by:

$$J = \frac{K_I^2}{E} \quad (4.1)$$

where E is the Young's Modulus of the material. The force of 1500 N is applied on the surface of each hole. The von-Mises stress distribution is plotted in Figure 23(b). The maximum stress value at

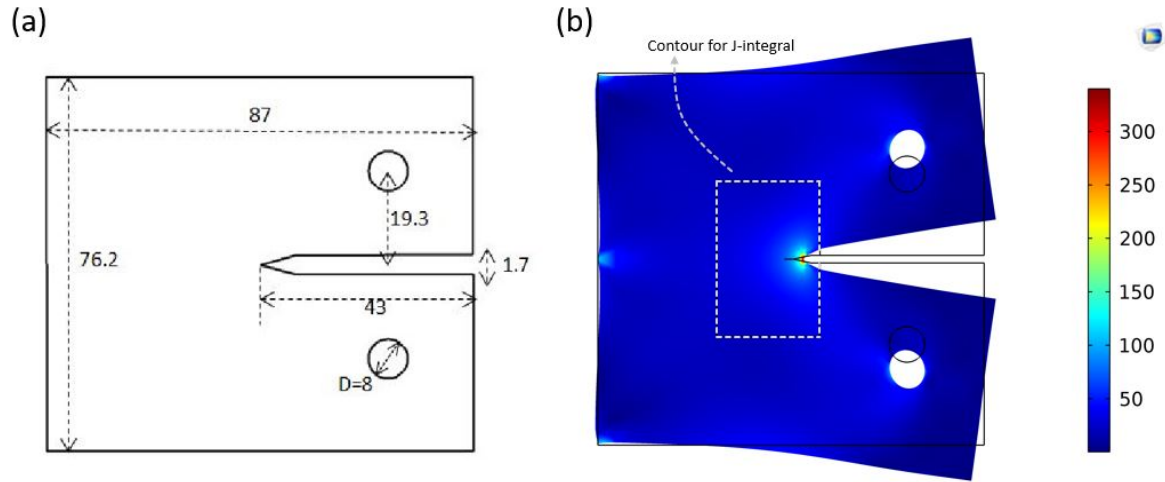


Figure 23. (a) The standard CT specimen with dimensions in (*mm*), and (b) the von Mises stress (*MPa*) distribution in CT specimen

the notch tip is calculated as 330 MPa . The value of stress intensity factor is calculated as $16 \text{ MPa}\sqrt{\text{m}}$.

Based on literature, the calculated K_I results in about 7 mm crack length after 12000 cycles.

4.4 Experimental Study

4.4.1 Experimental Setup

The performance of the designed stubbed plate in blocking friction emissions and enhancing the crack detection ability of the AE method is demonstrated experimentally using the CT specimen and the PC modeled in numerical studies. Two sets of CT specimens are used: the plain CT specimen, and the stubbed CT specimen as shown in Figure 24 (a) and (b), respectively. The stubbed CT specimen has aluminum cylinders with diameter of 6.35 mm and length of 9 mm machined out of aluminum

7075-T6 rod and mounted on the specimen surface by adhesive.

The fatigue testing is performed using the Instron 8500 Servo-hydraulic fatigue testing machine. A sinusoidal stress load with a cycle rate of 2 Hz , in load-control, tension-tension mode is applied. The maximum and minimum tension amplitudes are 1500 N and 200 N , respectively (with the stress ratio of $R=0.13$). The overall experimental setup is shown in Figure 25. The AE data is collected employing a PCI-8 data acquisition system manufactured by Mistras Group Inc. Two piezoelectric type AE sensors are mounted on the surface of the specimens to record the AE activities above the pre-defined threshold: R15 sensor (with the central frequency of 150 kHz) and R6 sensor (with the central frequency of 60 kHz). The fatigue test is performed with the same conditions for both specimens up to about 13000 cycles to propagate the crack length of about 6 mm . After the fatigue tests, the accurate length of the crack for each specimen is measured by Sonoscan Gen 6 C-SAM acoustic microscope. The specimens are placed in the ultrasonic immersion tank filled with distilled water. An ultrasonic transducer with 50 MHz center frequency is used to take the C-scan images of the specimens, as shown in Figure 26.

The sensors are bonded on the opposite surfaces of the specimens using super glue and connected to 40 dB gain pre-amplifiers with 20 kHz high-pass filter. R6 sensor is connected to channel one with 50 dB threshold and additional digital filter of 20-400 KHz . R15 sensor is connected to channel two with 45 dB threshold and additional digital filter of 100-200 KHz . The AE waveforms are recorded with 3 MHz sampling frequency. An optical microscope with a magnification rate of 40X is applied during the fatigue test to monitor the crack initiation and measure the crack length to an accuracy of 0.05 mm .

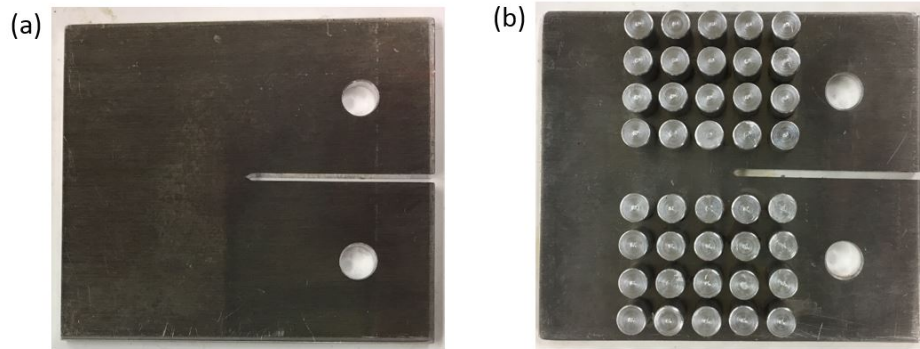


Figure 24. (a) The plain CT specimen, (b) the stubbed CT specimen

4.4.2 Experimental Results

4.4.2.1 Cumulative AE Energy Behavior with Respect to Crack Size

The cumulative energy of AE hits, as well as the cumulative number of hits resulted from the plain and stubbed CT specimens are presented in Figure 27. The results indicate that the stubs do not influence the AE hits received by R6 sensor, while they decreased the received AE hits of R15 sensor by two orders of magnitude. The cumulative number of hits obtained from R15 sensors for the stubbed CT specimen (Figure 27 (d)) decreases 98 percent as compared to the plain CT specimen (Figure 27 (b)). While the crack activity is clearly observed by the sudden discrete increase of AE energy in Figure 27 (b), the number of AE hits decreases considerably. This implies the potential effect of stubs in blocking the friction emissions form the grips.

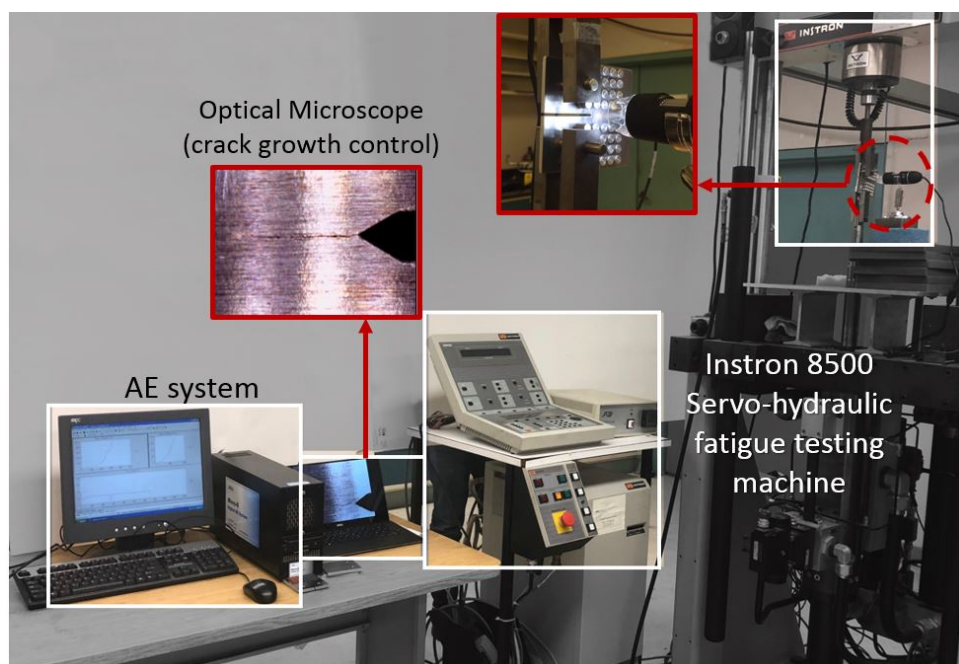


Figure 25. Experimental setup, demonstrating the Servo-hydraulic fatigue testing machine, the data acquisition system to monitor AE signals, and the optical microscope to control crack initiation and growth

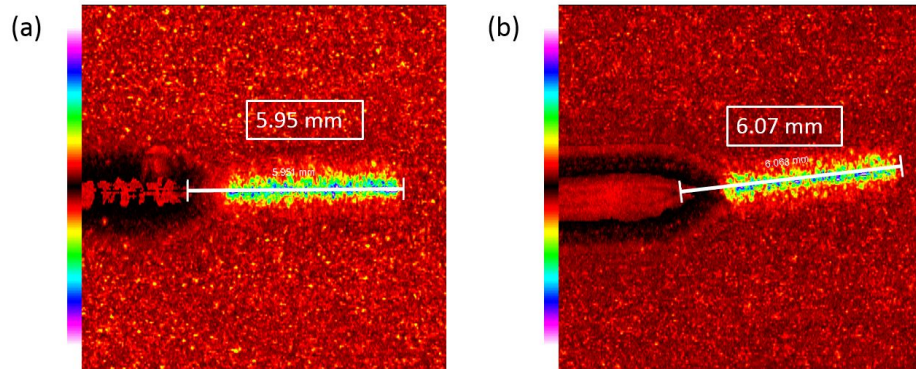


Figure 26. C-scan images of the (a) plain and (b) stubbed CT specimens after the fatigue testing

Further, the measured crack length, obtained from the optical microscope, is plotted along with the cumulative energy of AE hits received by R15 sensor for the plain and stubbed CT specimens, as shown in Figure 28. The crack propagation is well correlated with the changes in AE energy received by the R15 sensor for the stubbed CT specimen without any post-filtering. It confirms that the crack activities coming from the notch area are collected by the sensor properly. In contrast, the results of the plain CT specimen does not show significant correlations. This observation confirms that some irrelevant events are removed from the AE data received by the R15 sensor in the presence of stubs.

4.4.2.2 Comparison of AE Waveforms

The time-domain signals received by the R15 sensor at different times of fatigue tests for the plain and stubbed CT specimens are presented in Figure 29. It is observed that the pre-trigger section of the received waveforms are less noisier in the presence of stubs compared to the plain CT specimen. It

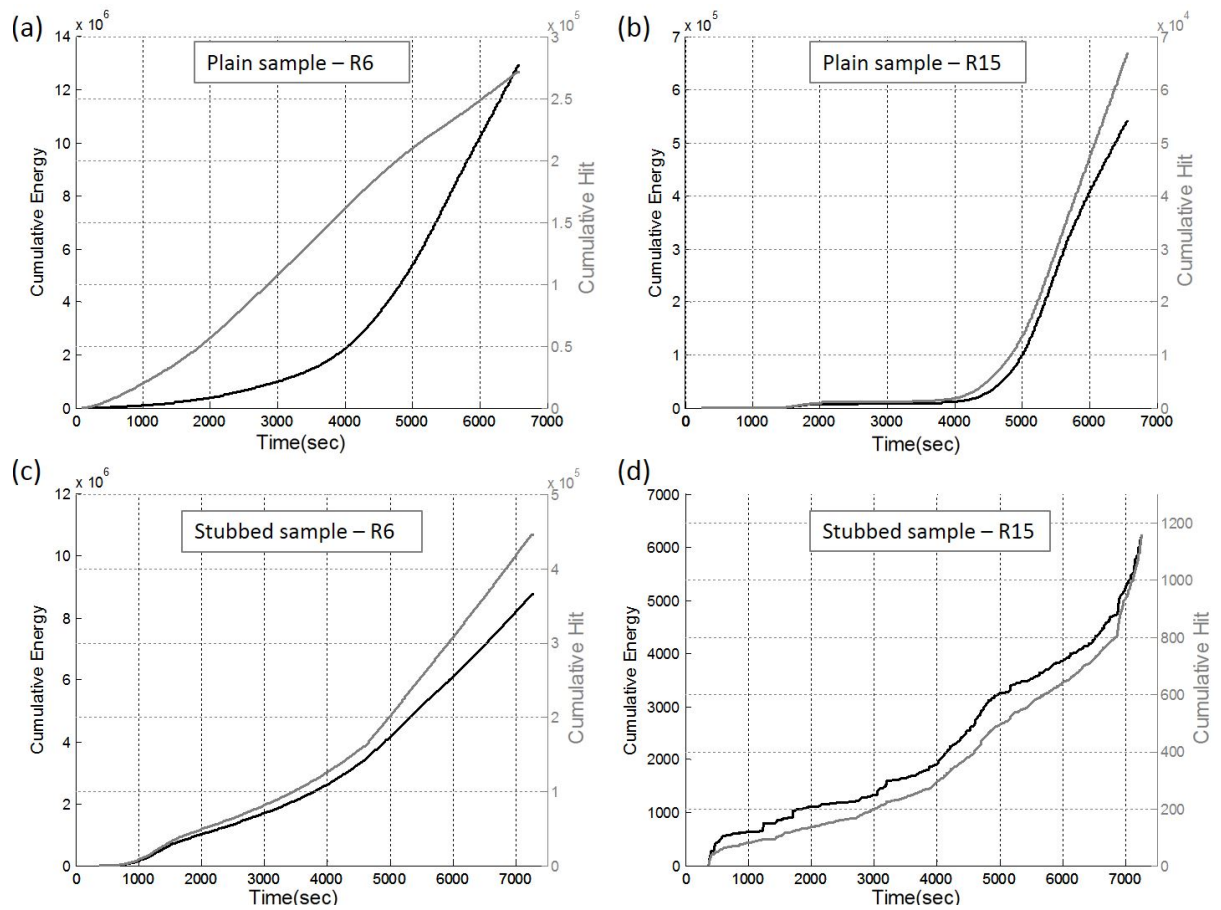


Figure 27. Cumulative AE energy and hit during the fatigue tests obtained from (a,b) the plain CT specimen and, (c,d) the stubbed CT specimen. (a,c) received by R6 sensor (b,d) are received by R15 sensor

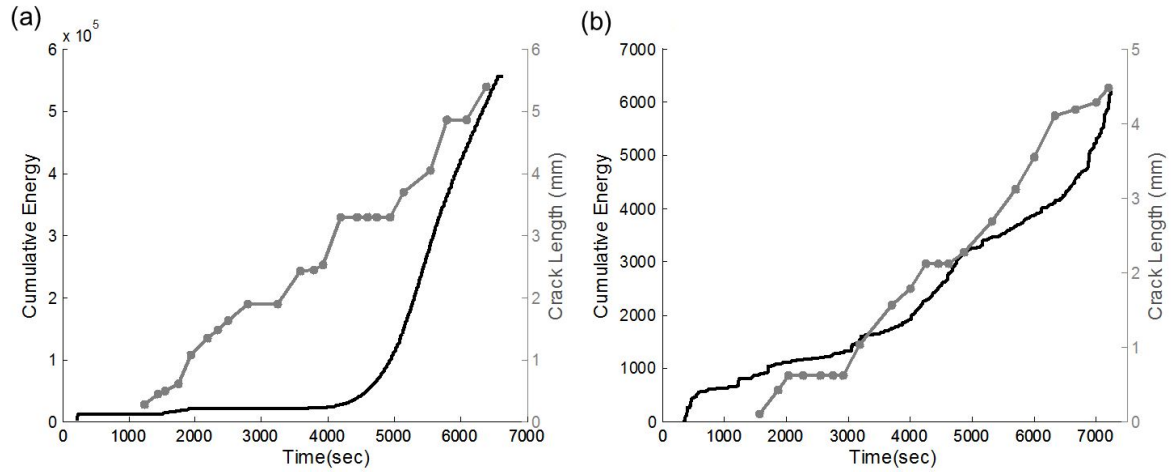


Figure 28. Cumulative AE energy during the fatigue test received by R15 sensor along with the crack length measured by optical microscope, (a) the plain CT specimen and, (b) the stubbed CT specimen.

is important to note that AE signals recorded from the plain CT specimen have lower signal to noise ratio than the stubbed CT specimen while all the experimental conditions (e.g., fatigue characteristics, sensor types, data acquisition setting) are kept the same. This can be explained by two approaches: (a) the experimental variability, and/or (b) blocking the friction emission provides the recording of correct signal initiation caused by crack growth. However, as shown in Figure 28, both specimens have similar crack growth rate; therefore, similar AE amplitudes are expected. The presence of stubbed plates is interpreted as improving the detection of accurate representation of AE signal released directly from the crack tip.

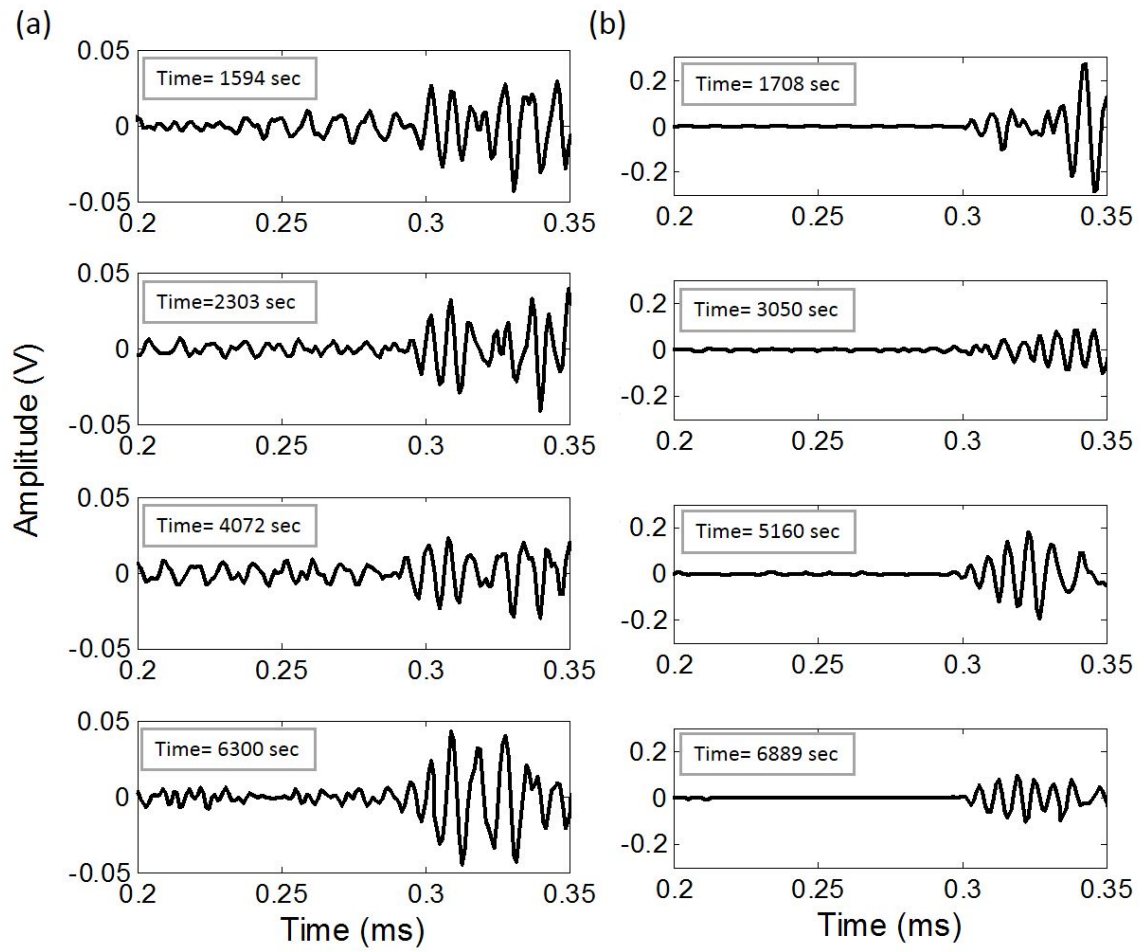


Figure 29. The initial cycles of received AE waveforms in different times of the fatigue test for (a) the plain CT specimen, and (b) the stubbed CT specimen.

To furthermore evaluate the influence of PCs, the frequency distribution of AE event amplitudes received by R15 sensor for the plain and stubbed CT specimens are compared (Figure 30). The results show that the lower-amplitude (45-48 dB) signals are reduced by two orders of magnitude in the stubbed CT specimen, while the higher-amplitude (50-80 dB) signals are found to have approximately the same distribution in both specimens (Figure 30 (c)). As a result, the distribution of the data are shifted toward higher amplitudes, indicating that the PCs efficiently block the lower amplitude events mainly associated with the friction in the grips.

4.5 The Repeatability of Acoustic Emission to Detect Fatigue Crack Growth

The repeatability on correlating damage characteristics with AE features is a challenging problem due to the complexity of AE signal detection process, the influence of geometric and materials compositions and the variables in data acquisition setting especially sensor type, threshold and analog/digital filters applied. The interference of secondary sources such as friction with primary sources such as crack growth also negatively affects the correlation of AE features and crack characteristics. In this section, the effectiveness of noise isolation using stubbed PC on repeatability of AE method to correlate damage characteristics with AE features is studied.

For this purpose, the experimental fatigue test is repeated employing a second set of specimens: plain and stubbed CT specimens, identical to the previous samples. However, different thresholds are used in these experiments to study the influence of threshold on the AE-fatigue crack correlation. To compare the results of two experiments, the nomenclature as presented in Table I is used to identify the specimen types and the corresponding data acquisition variables.

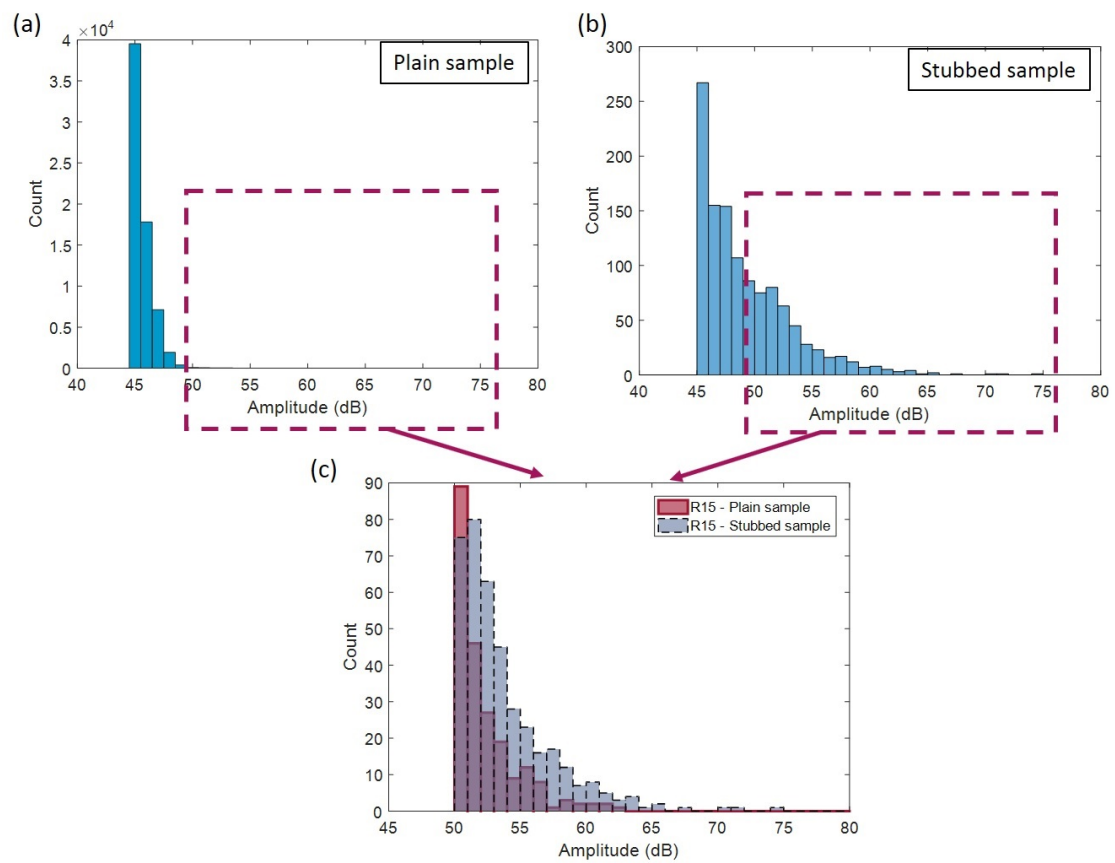


Figure 30. Histogram of AE hit amplitudes for (a) the plain CT specimen, and (b) the stubbed CT specimen.

TABLE I
SPECIMEN NAMES AND THEIR DATA ACQUISITION SETTING

Sample Name ^(a)	Type	Sensor	Threshold (dB)	Filter (kHz)	Number of Cycles	Final crack Length (mm)
PL1	Plain	R6	50	20-400	12800	5.95
		R15	45	100-200		
ST1	Stubbed	R6	50	20-400	13600	6.07
		R15	45	100-200		
PL2	Plain	R6	45	20-400	12800	6.8
		R15	40	100-200		
ST2	Stubbed	R6	45	20-400	13000	6.6
		R15	40	100-200		

(a) PL: plain specimen, ST: stubbed specimen.

The cumulative AE hits and AE energy resulted from the second set of specimens (PL2 and ST2) are presented in Figure 31. Similar to the results of the first set, it is observed that the cumulative hits and energy received by R15 from the stubbed specimen decreases significantly compared to the plain specimen, while the cumulative hits and energy received by R6 do not show remarkable changes.

A post-test amplitude filter (45 dB for R15 sensor and 50 dB for R6 sensor) is applied to the second set in order to have similar threshold as the first set. F-PL2 and F-STL2 indicates the filtered results of the plain and stubbed specimens from the second set, respectively. It is observed that the cumulative AE hits received by R15 sensor is not repeatable in the plain specimens (Figure 32 (a)), while the cumulative AE hits received by R15 from the stubbed specimens agree well with each other (Figure 32 (b)), indicating that the PC structure efficiently reduces the random errors originated from the background noises. No repeatable behavior is observed in the cumulative AE hits received by the R6 sensor neither

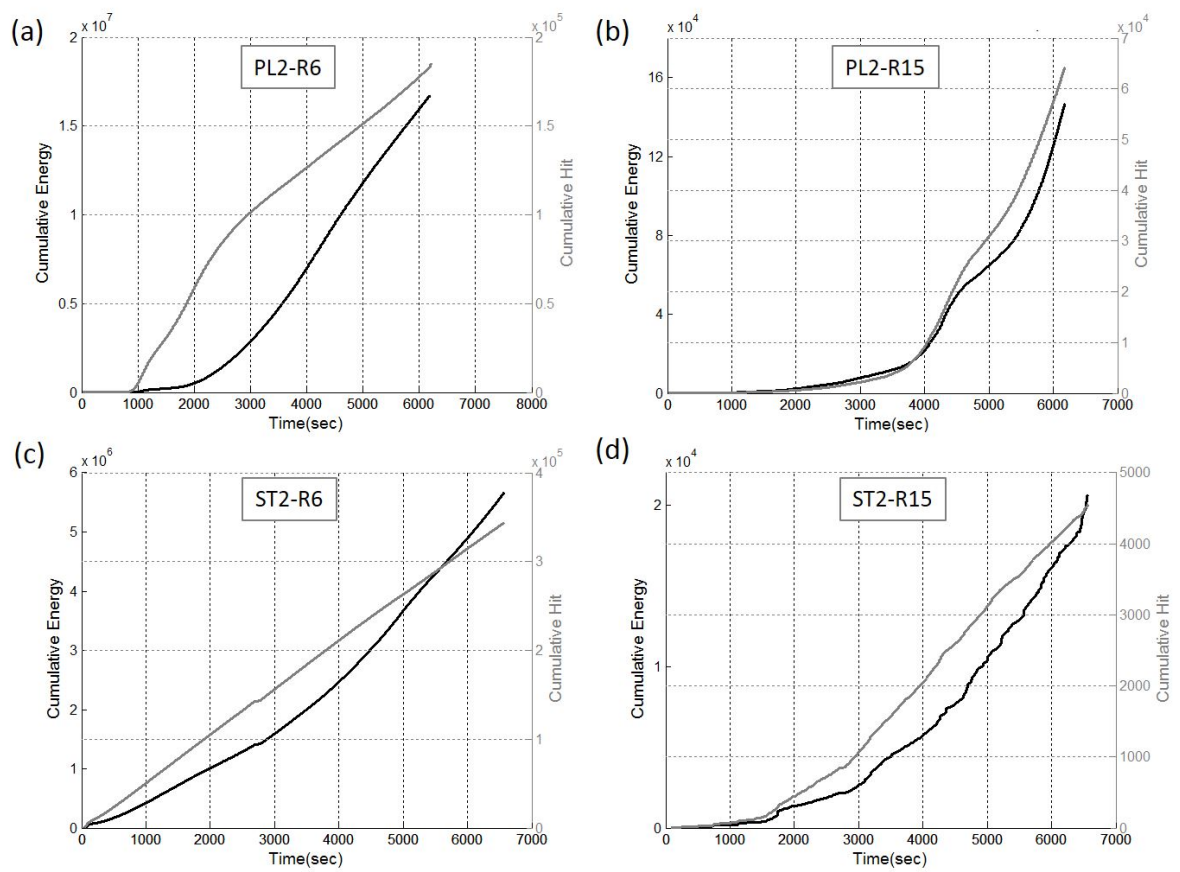


Figure 31. Cumulative AE energy and hits obtained from (a,c) PL2 and, (b,d) ST2. (a,b) show the results received by R6 sensor, and (c,d) show the results received by R15 sensor

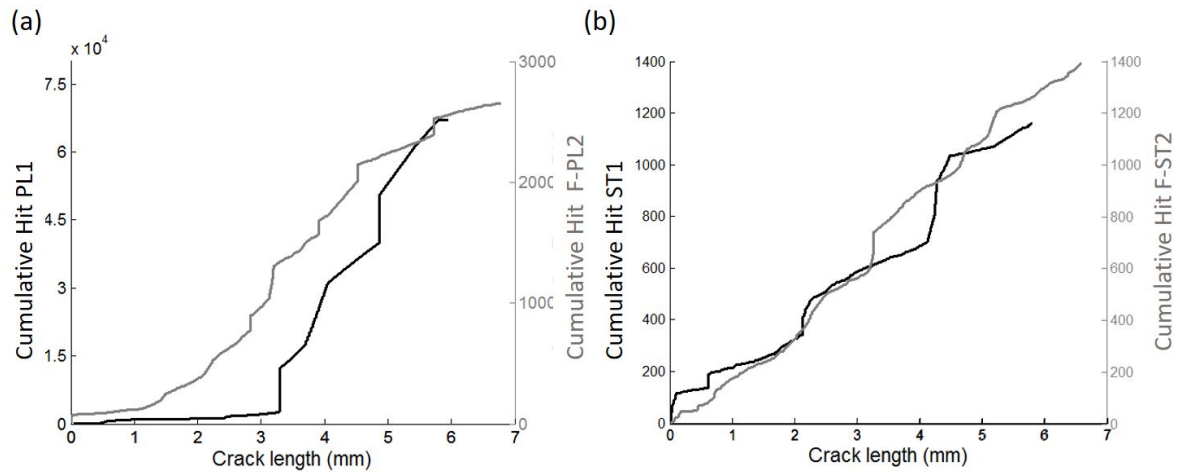


Figure 32. Cumulative AE hits obtained from (a) PL1 and F-PL2, and (b) ST1 and F-ST2 received by the R15 sensor with the synchronized threshold of 45 dB.

in the plain specimens nor in the stubbed specimens (Figure 33). It is important to note that the vertical scales of Figure 32 (a) and Figure 33 are different while the same vertical scales are used to represent ST1 and F-ST2 in Figure 32 (b).

To further analyze the effectiveness of the PC structure, an incrementally increasing post-test amplitude filter is applied to the second set of experiments (PL2 and ST2 specimens). It is revealed that by increasing the amplitude filter of the received data by R15 from 40 dB to 50 dB, the cumulative AE hits from PL2 decreases by almost two orders of magnitude (Figure 34 (a)), while the cumulative AE hits from ST2 decreases by approximately one order of magnitude (Figure 34 (b)). On the other hand,

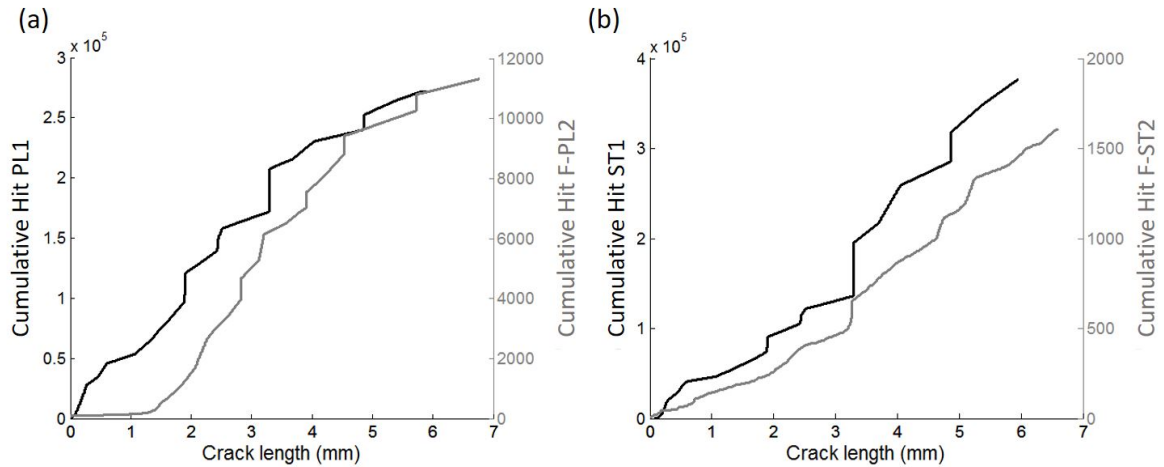


Figure 33. Cumulative AE hits obtained from (a) PL1 and F-PL2, and (b) ST1 and F-ST2 received by the R6 sensor with the synchronized threshold of 50 dB.

as expected, the PC structure did not mitigate the influence of threshold to the data received by the R6 sensor (Figure 35).

4.6 Summary

The AE method to monitor crack activities in real-time monitoring of structures confronts difficulties due to the influence of background noise. The two-dimensional PC structure is proposed to reduce the influence of background noise. The performance of the designed PC structure is demonstrated numerically and experimentally through the fatigue testing of aluminum standard compact tension specimens. The cumulative energy of AE obtained from the stubbed CT specimen shows better correlation with the crack growth, compared to the plain CT specimen without any post-processing filtering. The number of

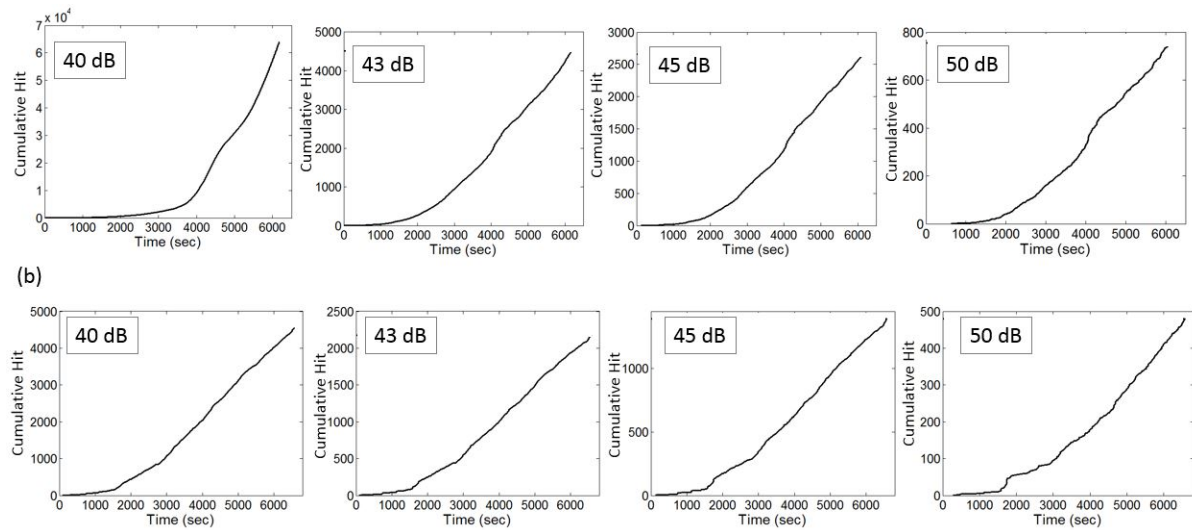


Figure 34. Cumulative AE hits received from the R15 sensor with different amplitude filters for (a) PL2 and (b) ST2 specimens.

AE hits are decreased by two order of magnitudes, while the crack activity is clearly observed, which implies the effect of stubs in reducing the secondary sources unrelated the crack growth. The developed crack detection methodology allows using one AE sensor with periodic stubs placed around the sensor to block the secondary emissions to monitor the behavior of known cracks in structures and reduces the recording of AE hits and the data file, which is crucial to combine the AE method with wireless technology.

Besides, the repeatability of AE cumulative activities to correlate with the fatigue crack growth is demonstrated effectively by minimizing the influence of secondary emissions. It is shown that while threshold-dependent features (e.g., energy, duration) cannot be controlled by simple post-test amplitude

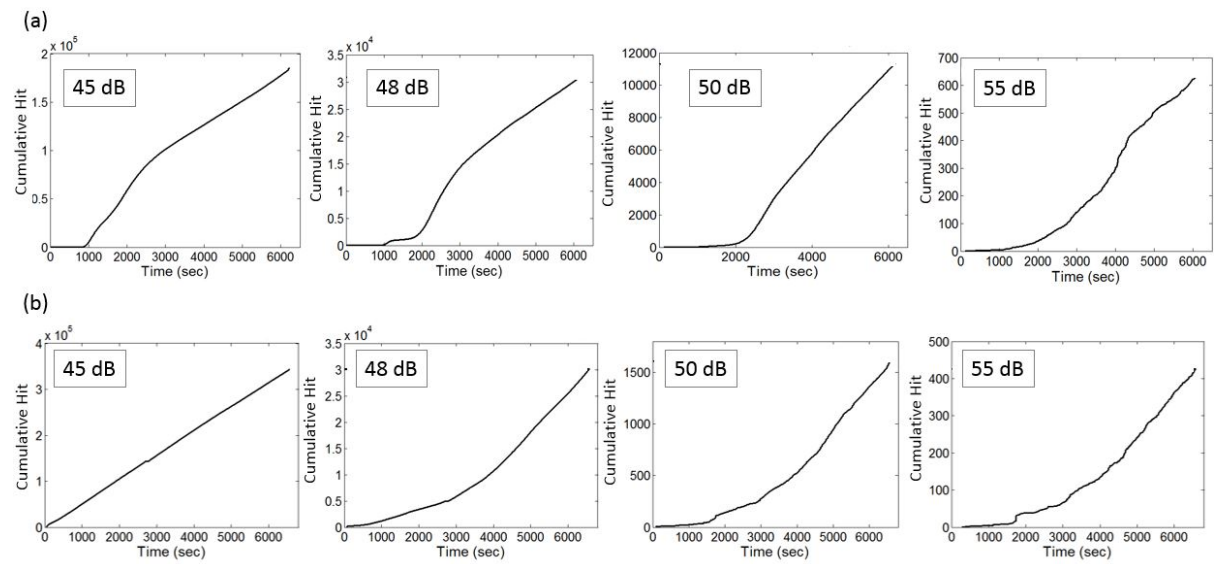


Figure 35. Cumulative AE hits received from the R6 sensor with different amplitude filters for (a) PL2 and (b) ST2 specimens.

filter, the cumulative AE hits and amplitude distribution have repeatable patterns in relation to the crack growth.

CHAPTER 5

PIEZOELECTRIC MEMS AE SENSORS

The content presented in this chapter has been published at the Journal of Sensors and Actuators A: Physical as "Piezoelectric MEMS Acoustic Emission Sensors", with my research advisor Dr. Didem Ozevin and Ph.D. student Hanie Kazari as the co-authors [2].

5.1 Introduction

The other component of the proposed AE system is the piezoelectric MEMS AE sensors that provides a highly narrow band response, to be tuned to the band gap of the PC structures. In this chapter, the design and characterization of piezo-MEMS sensors are presented. The designed main layout consist of four distinct sub-layouts, where each sub-layout include different sensors for AE and UT applications. The sensors are manufactured using PiezoMUMPs by MEMSCAP foundry. The PiezoMUMPs process is a 5-masks level SOI patterning and etching process, which includes deposition of $0.5\ \mu\text{m}$ AlN to form piezoelectric layer [92]. After manufacturing, each layout are packaged separately for performing experimental studies. A general description of the four layouts is presented in section 5.2. However, we only only focus on two of the Piezo-MEMS AE sensors and present the studies performed on them in the rest of the chapter. The sensors are numerically modeled using COMSOL Multiphysics software to tune them for the desired resonance frequencies. The details of design and manufacturing steps, and the numerical results are presented in section 5.3. Then, the fabricated sensors are packaged and the electrical connections are made through wire bonding. The performance of the piezo-MEMS AE sensors is

demonstrated through electromechanical and mechanical characterization experiments, as presented in section 5.4. Finally, the piezo-MEMS AE sensors are compared with the conventional piezoelectric AE sensors, followed by the summary of this chapter.

5.2 Description of Piezo-MEMS Device

The main designed layout is a $1\text{ cm} \times 1\text{ cm}$ area and made of four distinct sub-layouts. Each layout works as a separate device containing different types of sensors for different applications, including resonant AE sensors and ultrasonic transducers (UT), as shown in Figure 36. Layout 1 is an array of UT, where each unit cell is tuned to the resonant frequency of 1 MHz and is connected to the adjacent unit cells through silicon bridges. Individual unit cell can be used for detection or excitation through the provided pads. Layout 2 consists of four resonant AE sensors with different resonant frequencies (as indicated in Figure 36). In this chapter, we focus only on two of the piezo-MEMS AE sensors of this layout: the low-frequency (LF) design that is tuned to 40 kHz and the high-frequency (HF) that is tuned to 200 kHz . Layout 3 consists of two piezo-MEMS AE sensors, an array of 1 MHz UT, and two strain gauges that works with the transduction principle of piezoresistivity. Layout 4 consists of ultrasonic transducers tuned to 1 and 2 MHz , and two strain gauges.

5.3 Sensor Design

5.3.1 Manufacturing Process

As described above, the sensors are manufactured using the PiezoMUMPs provided by MEMSCAP foundry [92], in which thin-film piezoelectric devices are micromachined on a 150 mm (100) oriented silicon-on-insulator (SOI) wafer. The manufacturing process is described below as illustrated in Figure 37, via the cross-sectional view of the device.

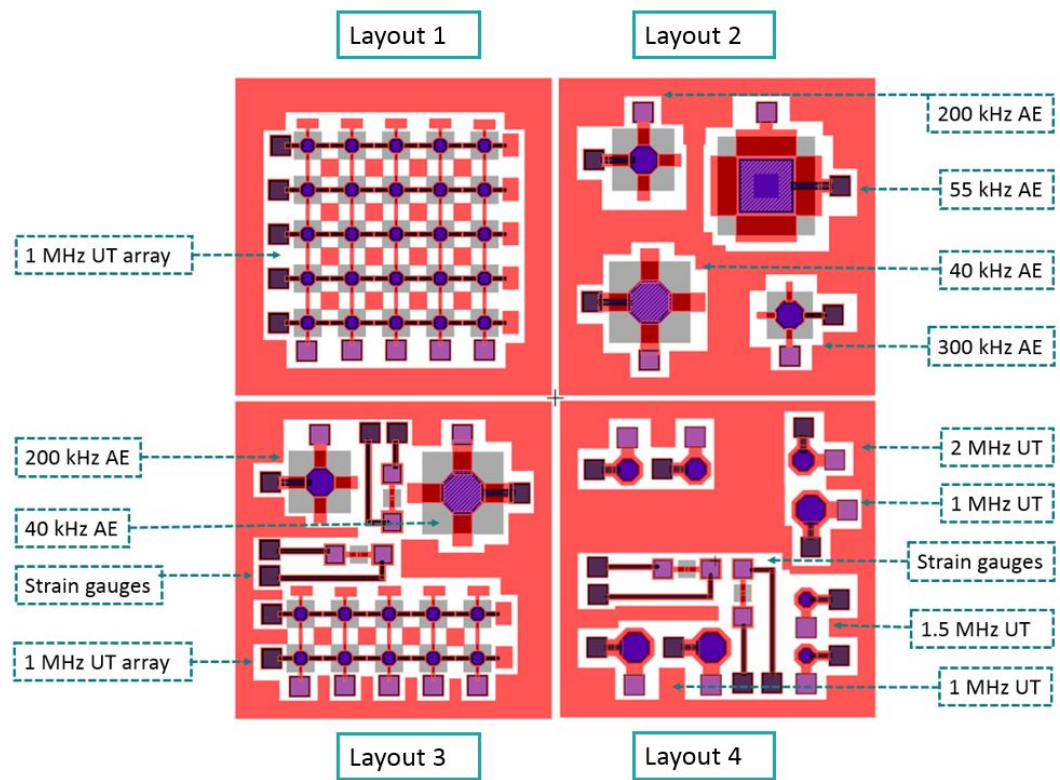


Figure 36. The designed device layout, indicating four sub-layouts

1. The top surface of the silicon layer is doped using n-type doping. A phosphosilicate glass (PSG) layer is deposited and annealed at 1050°C in Argon (this layer is then removed through wet etching).
2. A thermal oxide layer of 2000 Angstrom is grown and lithographically patterned through a first level mask. The thermal oxide layer provides isolation between the SOI, the AlN and the pad-metal layers.
3. A 0.5 μm of AlN is deposited over the wafer by reactive sputtering, and then lithographically patterned through a second level mask.
4. The pad-metal layer is deposited. The layers of 20 nm of chrome and 1 μm of aluminum are deposited and patterned through a liftoff process. The pad-metals form the electrodes for electrical connections.
5. In a fourth mask level, the silicon and the oxide layer are lithographically patterned and etched through deep reactive ion etching. A special recipe eliminates any undercutting of silicon layer when the etch reaches the buried oxide.
6. A protection material made of polyimide coat is provided to the top surface in order to hold the wafer together through subsequent trench etching.
7. The substrate layer is lithographically patterned from the bottom using a fifth mask level. The bottom side oxide layer is removed using reactive ion etching, and deep reactive ion etching is used to etch completely the substrate layer.

8. Finally, a dry etch process is used to strip the front side protection material. This process releases any mechanical structures in the silicon layer that are located over through-holes defined in the substrate layer.

5.3.2 Final Sensor Design

The sensing layer consists of a thin-film piezoelectric layer sandwiched between the pad metal layer and the doped silicon layer. AlN is used as the piezoelectric material with the electrical and mechanical properties as presented in Table II [103; 104; 105; 106]. Here, $e_{31,f}$ is intrinsic effective piezoelectric coefficient, ϵ_0 is vacuum permittivity, $\epsilon_{33,f}$ is relative dielectric coefficient and d_{33} and d_{31} are polarization coefficients caused by per unit of mechanical stress. The value of coefficient $e_{31,f}/\epsilon_0\epsilon_{33,f}$ for AlN is higher than PZT, so it is preferred for sensing applications [82]. Besides, the residual stresses are avoided through the deposition process, as AlN does not require annealing procedure. The design of piezoelectric MEMS device is controlled through the design rules provided by the PiezoMUMPs Design Handbook published by MEMSCAP foundry [92]. While the thicknesses of the layers are restricted by the manufacturing process, the planar dimensions are flexible but bounded with the design rules. The dimensions are varied to tune the fundamental frequency to 40 kHz (for LF sensor) or 200 kHz (for HF sensor). The microstructural layers consist of doped silicon, AlN and metal layer which are working as the bottom electrode, sensing layer and top electrode, respectively. Each design consists of a mass-spring system where a movable plate is connected with four partially clamped beams to the substrate. The mass and stiffness are controlled through the geometry of the beams and diaphragm to tune the sensors to the desired frequencies. For the design of the LF sensor, a reasonable beam and diaphragm geometry could not be achieved due to the restrictions of the design rules. Therefore, the back-surface

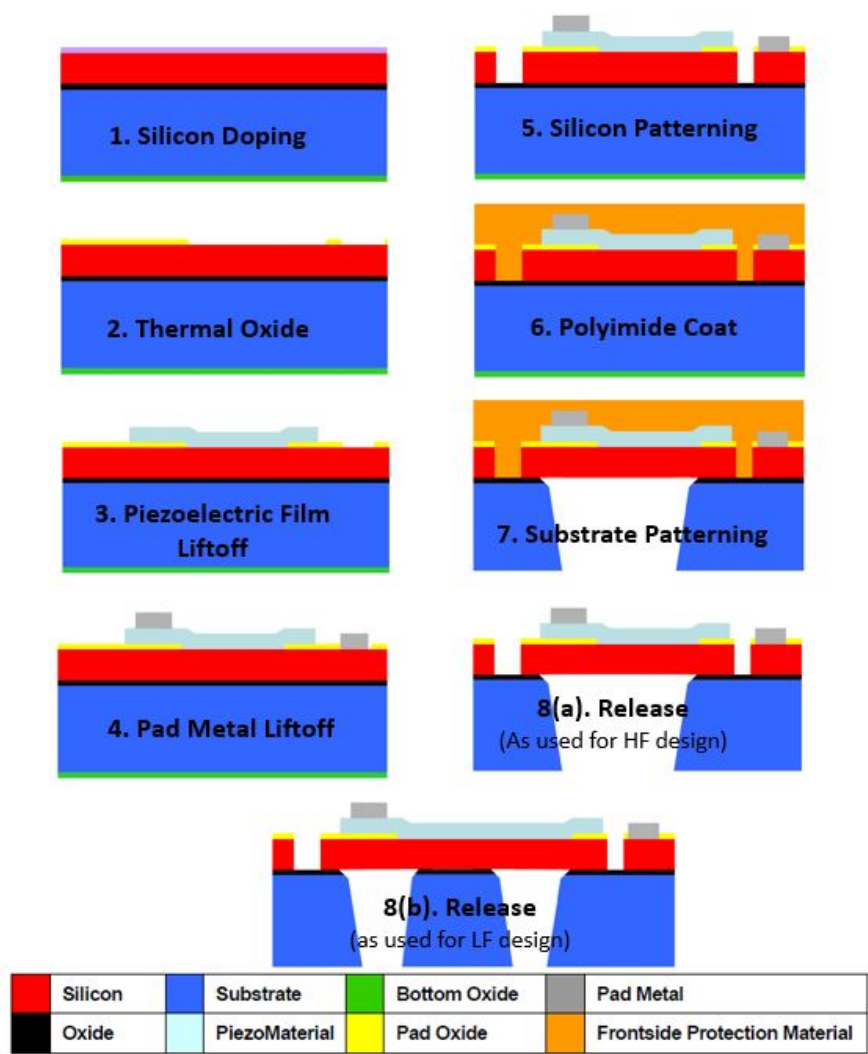


Figure 37. Summary of the PiezoMUMPs

TABLE II
ELECTRICAL AND MECHANICAL PROPERTIES OF TWO COMMON PIEZOELECTRIC
MATERIALS (ALN AND PZT)

Coefficient	$e_{31,f}(cm^{-2})$	$d_{33}(pmV^{-1})$	$d_{31}(pmV^{-1})$	$e_{31,f}/\epsilon_0\epsilon_{33,f}$
AlN	-1.05	3.9	2.78	-11.3
PZT	-8 to -12	60 to 130	171 to 274	-7 to -1.8

etching is utilized for forming an additional mass to the doped silicon layer, which consists of entire silicon substrate. The cross-sectional views and dimensions of the sensors, deposited layers, etched areas as well as the planar view of the designed sensors in the L-Edit are presented in Figure 38. The HF sensor operates in 31-mode where the applied stress in direction 3 is converted into the electrical voltage in direction 1. The LF sensor operates in 33-mode where the applied stress in direction 3 is converted into the electrical voltage in direction 3. The conversion mode is further discussed in the numerical studies section. The scanning electron microscope (SEM) images of the piezo-MEMS sensors are presented in Figure 39. The SEM images indicate successful etching process of the octagonal shape for both sensors and the large mass for the LF sensor.

5.3.3 Numerical Studies

The main design variable is the resonant frequency of the sensors. The fundamental frequency of each sensor in z-direction is correlated to its modal stiffness and mass by the ratio of $\sqrt{k/m}$. The resonant frequency can be only adjusted by changing the length, width or the geometry of diaphragm and suspending mass, because the material properties and thickness of each layer are restricted by the fabri-

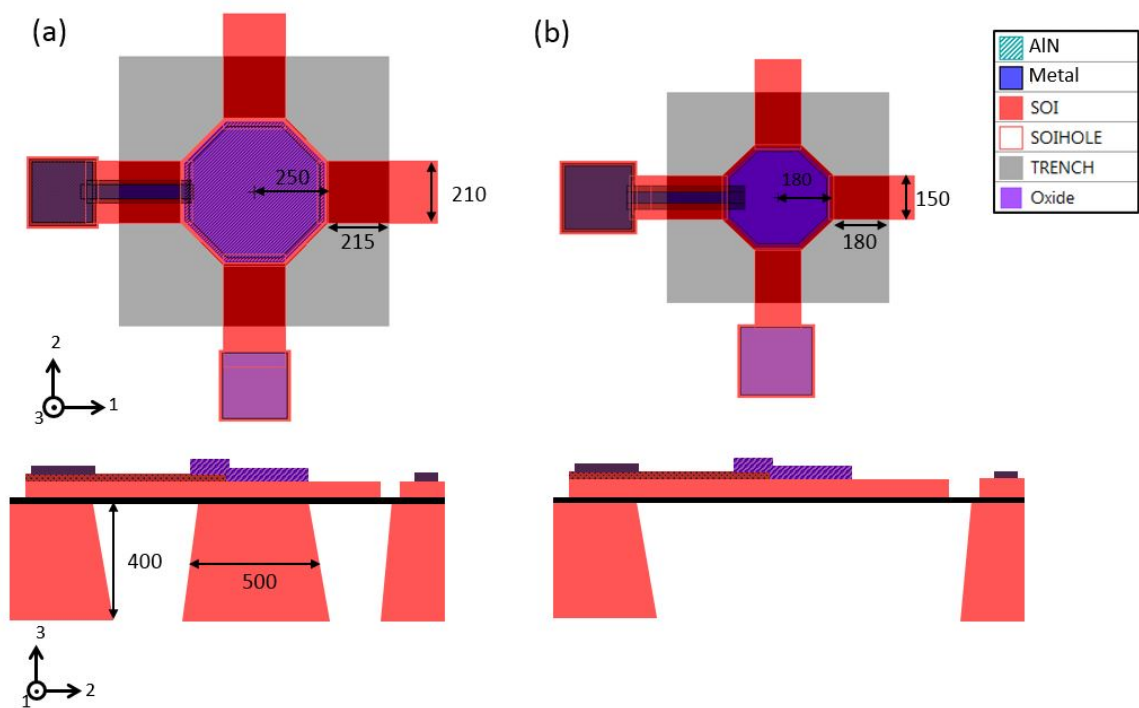


Figure 38. L-Edit plots illustrating the planar view of the sensors designed for (a) 40 kHz (LF) and (b) 200 kHz (HF), along with the schematic cross-sectional view of each sensor (unit: μm)

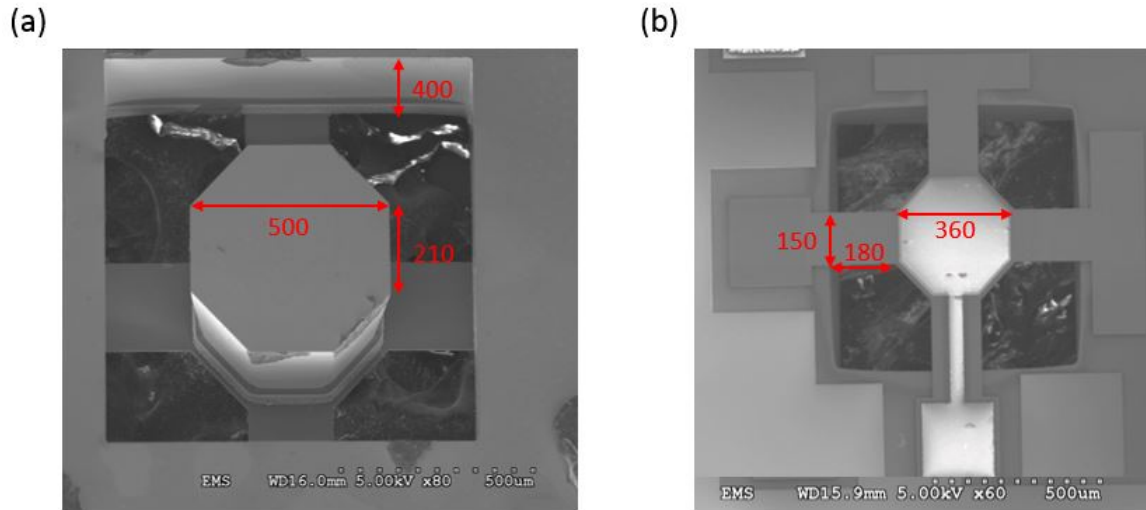


Figure 39. SEM images of (a) LF and (b) HF sensors (unit: μm)

cation process rules. The diaphragm and the suspending mass are simulated in COMSOL Multiphysics software implementing solid mechanics module. The eigenfrequency analysis is performed in order to find the fundamental mode shapes and frequencies. The thickness of the silicon layer is $10 \mu m$ while the thickness of the AlN and oxide layers are $0.5 \mu m$ and $1 \mu m$, respectively. Since the thickness of the silicon layer is dominated in the entire device layers, only silicon layer is used in the models. The material properties of the silicon used in the numerical models are listed in Table III.

Generally, a square shape diaphragm has higher fill factor; however, in terms of stress distribution, it does not have uniform stress specially at the edges where high stress concentration can be observed. Another geometric option is circular geometry. Based on the manufacturing design rules, there are

TABLE III

MATERIAL PROPERTIES OF SI AND ALN AS USED IN NUMERICAL SIMULATION

Material	Density, $\rho(kg.m^{-3})$	Young's Modulus, $E(GPa)$	Poisson's ratio, ν
Si	2330	156	0.125
AlN	3300	320	0.24

restrictions in resolution of the circular shapes. An octagonal shape diaphragm is sought as the solution, as it is the closest polygon to circle and satisfies minimum beam dimensions of the design rules. The dimensions of the beams and octagonal shapes are listed in Table IV. To design the low frequency sensor, it is needed to have either lower beam stiffness or higher suspending mass. The highest possible size of the beams is restricted by the manufacturing design rules. Therefore, the lower frequency sensor is designed by increasing the suspending mass. The full thickness suspended structures can be defined through the substrate layer of the SOI wafer during the trench patterning procedure (step no. 7 of the manufacturing section). The full thickness suspended mass with octagonal shape is provided during the reactive-ion etching process. The thickness of the mass is the same as the substrate which is $400\ \mu m$. The fundamental frequencies of the LF and HF sensors obtained from the numerical simulations are presented in Figure 40. Both the LF and HF designs are moving in z-direction with the fundamental frequencies of $40\ kHz$ and $200\ kHz$, respectively. The second mode shapes of the sensors are presented as well, which are obtained as $41\ kHz$ and $450\ kHz$ for the LF and HF sensors, respectively. It is noticed that the first two modes of the LF sensor are close.

TABLE IV

BEAMS AND OCTAGONAL DIMENSIONS			
Sensor	Beam dimensions ($\mu m \times \mu m$)	Beam cross section ($\mu m \times \mu m$)	Octagonal side (μm)
LF	210 \times 215	10 \times 210	210
HF	150 \times 180	10 \times 150	150

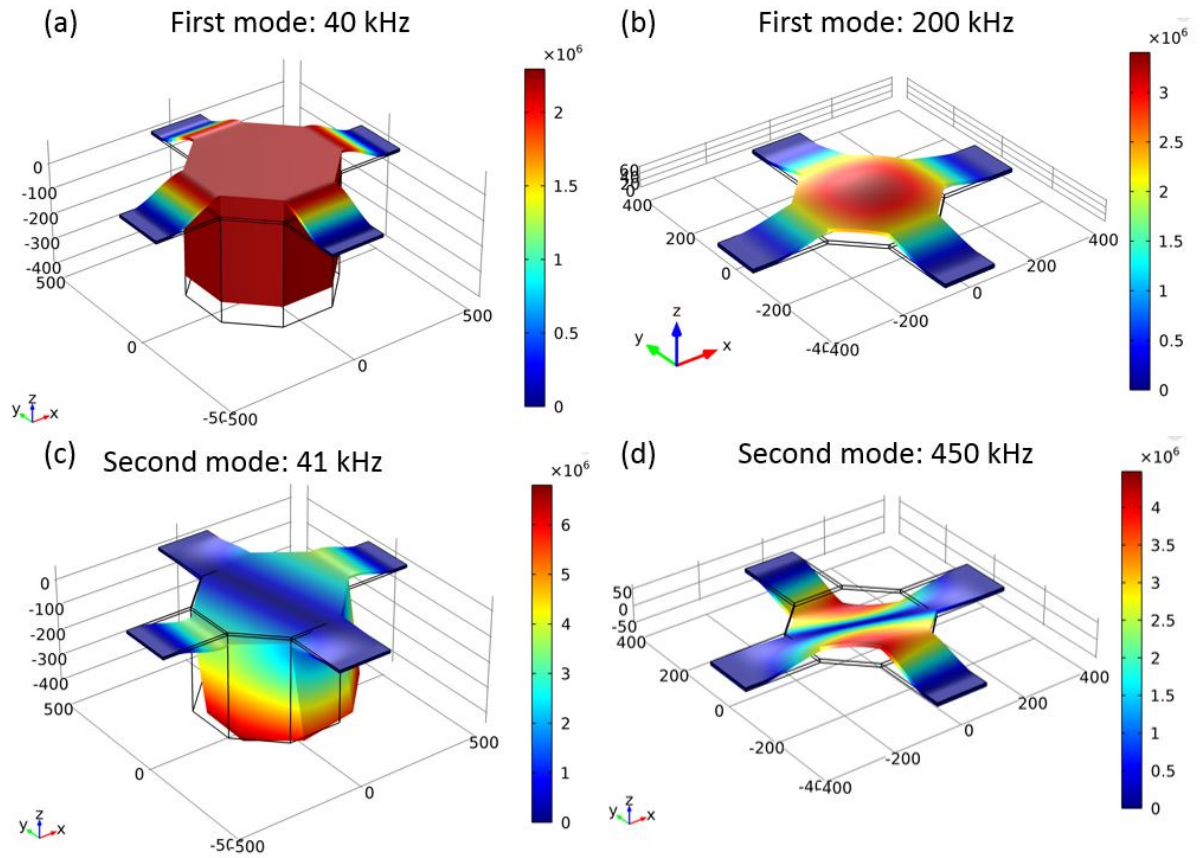


Figure 40. The first and second mode shapes of LF (a,c) and HF (b,d) sensors

The second numerical model is conducted for the LF sensor using transient analysis in time domain to find the input-output conversion. The model uses the built-in piezoelectric device interaction in COMSOL, which contains two fundamental physics interfaces: solid mechanics and electrostatics. A thin layer of AlN ($0.5 \mu m$) is added on top of the silicon layer to simulate the piezoelectric domain. A wide-band load is introduced as a chirp signal, as the input mechanical force, which contains a range of frequencies from $10 kHz$ to $100 kHz$. Free tetrahedral elements are used to mesh the model. The mesh resolution is kept at least 20 elements in one wavelength of the highest frequency to achieve acceptable accuracy [98]. The effect of damping is not considered in this study. Figure 41 illustrates the piezoelectric layer, and the ground and terminal boundaries as defined on the bottom and top surfaces of the AlN. The input force and the output voltage received from the terminal layer and their frequency spectra are plotted in Figure 42. It is observed that the output voltage has a narrow-band response at $40 kHz$ which confirms the designed frequency response of the LF sensor (Figure 42(d)). Moreover, total displacement of the LF sensor at six different times in a typical cycle of oscillation is shown in Figure 42(e), which illustrates the out-of-plane movement of the sensor. It is worth noting that the movement of the LF sensor causes inertial force in the AlN layer, which is the main driving force leading to the production of current. There is no bending in the AlN layer as opposed to the diaphragm design of the HF sensor. The electric field polarization is parallel to the stress distribution in the AlN layer, as a result, the d_{33} mode should be considered for the LF sensor. The HF sensor converts mechanical movement into electrical current due to diaphragm deformation. The diaphragm is bended at the operational frequency (the curved shape is illustrated in the results of the eigenfrequency study), d_{31} is the piezoelectric conversion mode of the HF sensor.

Boundary load:

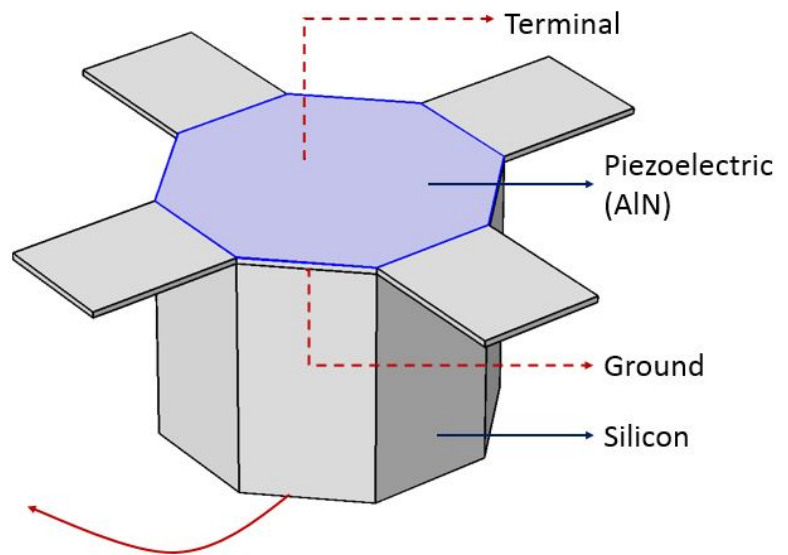
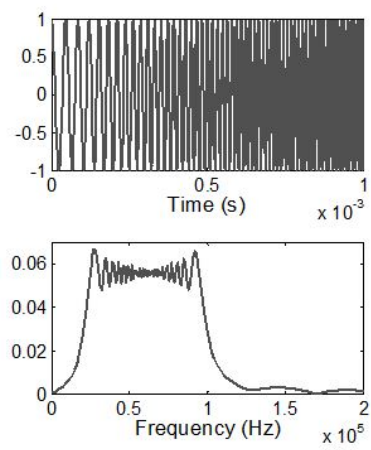


Figure 41. The time-domain numerical simulation of the LF sensor, illustrating the defined AlN and silicon layers, the ground and terminal surfaces and the applied load

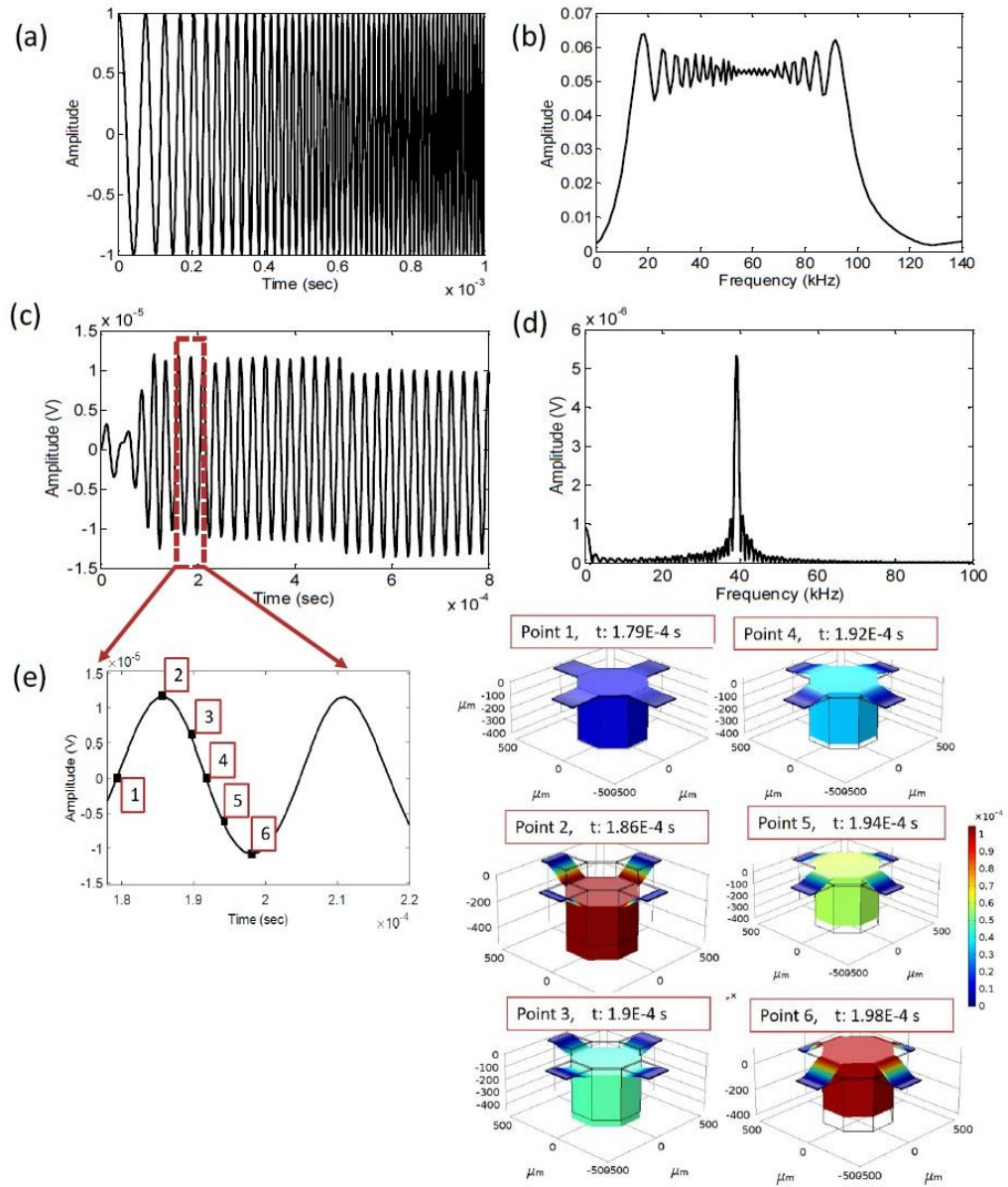


Figure 42. Time-domain numerical analysis of the LF sensor, (a) the waveform of the applied chirp, (b) the frequency spectrum of the applied chirp signal, (c) the waveform of the received signal and (d) the frequency spectrum of the received signal, (e) the displaced shapes at six different time positions

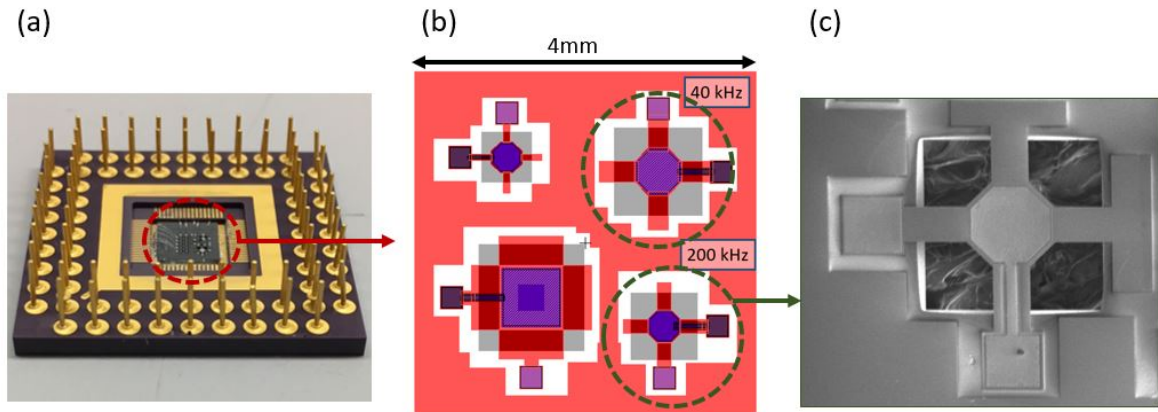


Figure 43. (a) The packaged piezo-MEMS device (b) the L-Edit image of the MEMS chip that includes LF and HF sensors (c) the SEM image of the HF sensors

5.4 Characterization Experiments

The fabricated piezo-MEMS device is mounted on a ceramic package using a two-part silver epoxy, and the electrical connections are made through wire bonding. The packaged device is shown in Figure 43 (a). The L-Edit image of the MEMS chip is used to illustrate the LF and HF sensors on the packaged device in Figure 43 (b), and the SEM image of the HF sensors is shown in Figure 43 (c). The electromechanical characterization of the packaged device is evaluated through measuring impedance, resistance, inductance, and passive and motional capacitances of the LF and HF sensors.

5.4.1 Electromechanical Characterization

The main parameters to characterize piezo-MEMS are electrical and mechanical bandwidths and sensitivity. Here, effective coupling coefficient, K_{eff} , which is defined as the ratio of transduction be-

tween mechanical and electrical energy, is computed to evaluate the overall performance of the sensors. The admittance of each sensor is measured using impedance analyzer (Agilent Technologies, 4294A Precision Impedance Analyzer), by sweeping a range of frequencies. The measured admittance values, in the forms of magnitude and phase, are presented in Figure 44. When the sweeping frequency matches the resonance frequency of the sensor, the impedance is amplified due to electromechanical coupling. The measured resonant frequencies along with the numerical resonant frequencies are tabulated in Table V. The LF sensor as observed in the phase plot (Figure 44) has two peaks. This is correlated with the fact that the first two modes of vibration of the LF design are close, as observed in the numerical simulation (Figure 40(c)).

In this study, the equivalent circuit as shown in Figure 45 is utilized to represent the parameters to evaluate the electromechanical performance of the fabricated piezo-MEMS AE sensors [107]. The required components, including passive capacitance C_0 , motional capacitance C_m , motional inductance L_m and motional resistance R_m are measured using impedance analyzer. The measured C_0 and C_m for the LF sensors are both $4.59 \times 10^{-11} F$, and for the HF sensor are $3.61 \times 10^{-11} F$ and $4.76 \times 10^{-11} F$, respectively. The K_{eff} coefficient is correlated to the electrical and mechanical parameters by the following relation [107]

$$K_{eff}^2 = \frac{C_m}{C_m + C_0} \quad (5.1)$$

The value of K_{eff} is calculated as 75.4% for the HF sensor and 70% for the LF sensor. Another important parameter in MEMS resonators is Q-Factor, which is defined as the ratio of energy stored in the system to energy dissipated per cycle, and measured by the impedance analyzer. The Q-Factor

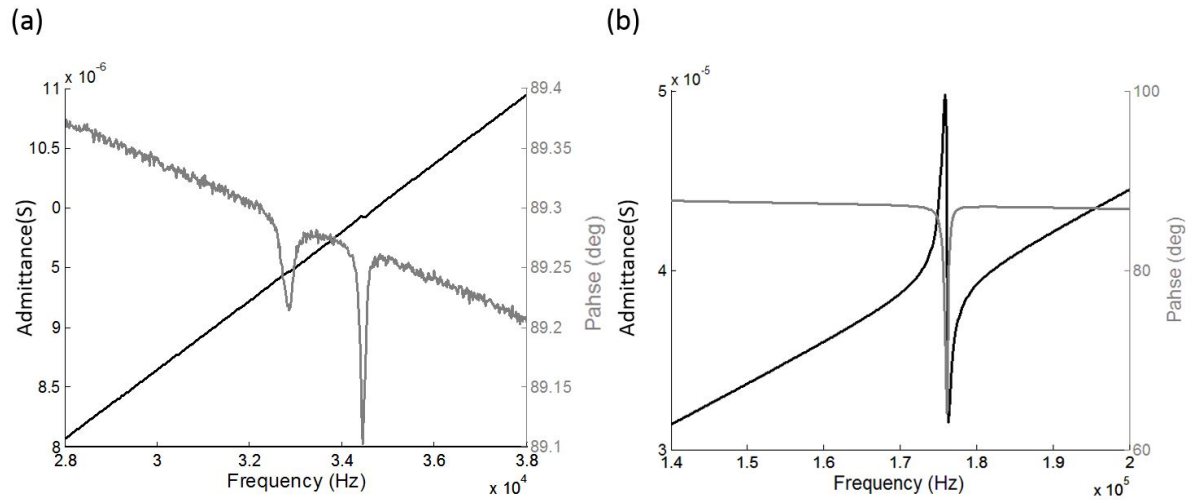


Figure 44. Admittance results of the (a) LF and (b) HF sensors

values are measured as 71 and 1.98 for the LF and the HF, respectively. High Q-Factor for the LF sensor indicates a very low damping ratio.

5.4.2 Mechanical Characterization

The performance of the sensors is studied using an excitation signal from the conventional piezoelectric transducer R6 or R15. R6 and R15 are resonant type piezoelectric AE transducers made of bulky piezoelectric ceramics, having resonant frequencies at 60 kHz and 150 kHz, respectively, and are manufactured by Mistras Group Inc. The MEMS package is directly attached to the surface of the R6 and R15 transducers to excite the out-of-plane motion of the piezoelectric layers of the LF and HF sensors, respectively, using vacuum grease as the couplant. The sensors are connected to the AE data acquisition

TABLE V
EXPERIMENTAL AND NUMERICAL RESONANT FREQUENCIES

Sensor	Experimental (kHz)	Numerical (kHz)
LF	35	40
HF	175	200

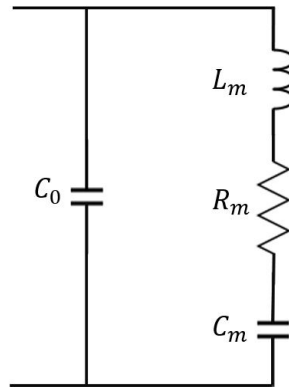


Figure 45. Equivalent circuit model used to describe the electromechanical response of piezo-MEMS

system manufactured by Mistras Group Inc., and a built in software is used to generate a 5-cycle sine wave with the desired frequency using experimental setup as shown in Figure 46. First, the R6 transducer is used for generating the excitation signal ranged from 10 kHz to 40 kHz with the increments of 1 kHz , and the LF sensor is used to receive the signal. Then, the R15 transducer is used for generating the excitation signal ranged from 120 kHz to 220 kHz with the increments of 5 kHz , and the HF sensor is used to receive the signals. The sampling frequencies are set as 1 MHz and 3 MHz for the LF and HF sensor experiments, respectively. The time domain signals along with their frequency spectra for the selected excitation frequencies near the resonant frequency of each sensor are presented in Figure 47 and Figure 48 for the LF and HF sensors, respectively. The maximum amplitudes of the time history from all the received signals are extracted and plotted in Figure 49. The maximum amplitude of each sensor is near the designed resonant frequency, which is about 32 kHz for the LF sensor and 170 kHz for the HF sensor, similar to the electrochemical results as shown in Table V. The LF sensor has very narrow bandwidth, which is important to apply the advanced source localization algorithms [108]. As obtained by the electromechanical experiments, the LF sensor has higher Q-factor (i.e. lower damping) than the HF sensor. However, the low damping of the LF sensor causes significant ringing, which may interfere with the AE signals released by short time differences.

5.5 The Comparison of Conventional Piezoelectric and Piezo-MEMS AE Sensors

The behaviors of conventional piezoelectric and the designed piezo-MEMS AE sensors are compared under the same excitation signal generated on a plate-like structure. The LF sensor is compared with the R6 sensor using an excitation at 30 kHz . The sensors are attached to the surface of a composite plate with thickness of 5 mm using vacuum grease and connected to the AE data acquisition

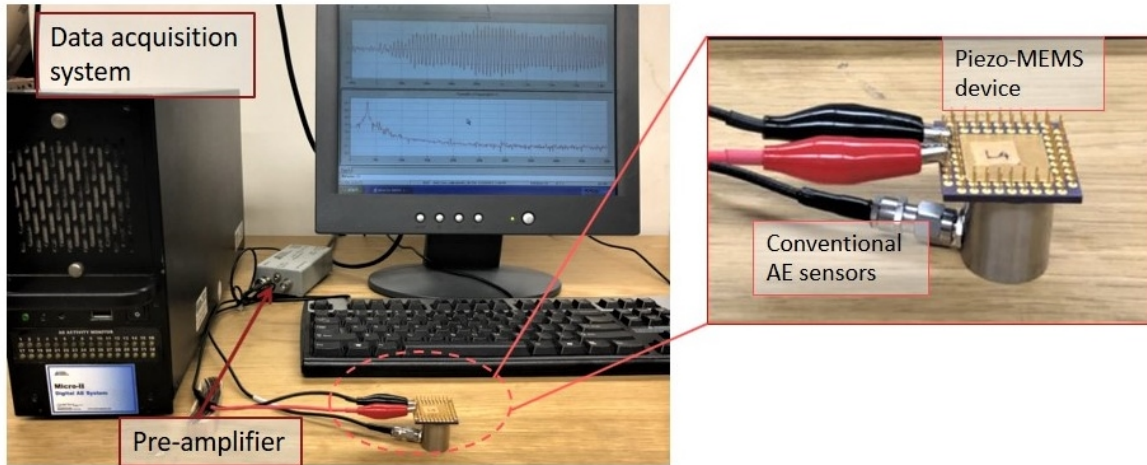


Figure 46. Experimental setup for mechanical characterization of the LF and HF sensors using face-to-face excitation by conventional AE transducers

system using a 40 dB pre-amplifier, as shown in Figure 50. Another R6 transducer is used to excite a 5-cycle sine wave signal at the frequency of 30 kHz . The same experiment is repeated for the HF and R15 sensors using another R15 transducer to generate the excitation signal near 170 kHz . The time history waveforms and their frequency spectra are presented in Figure 51. The shapes of signals in both conventional piezoelectric and piezo-MEMS AE sensors are similar; however, the amplitudes of the received signals by the conventional piezoelectric AE sensors are two orders of magnitude higher than the piezo-MEMS AE sensors. However, it is important to note that a unit cell sensor is utilized to design each piezo-MEMS AE sensor. For example, the size of the LF sensor is about $1 \times 1 \text{ mm}^2$. The sensitivity of the piezo-MEMS sensors can be improved by coupling a number of unit cells. The

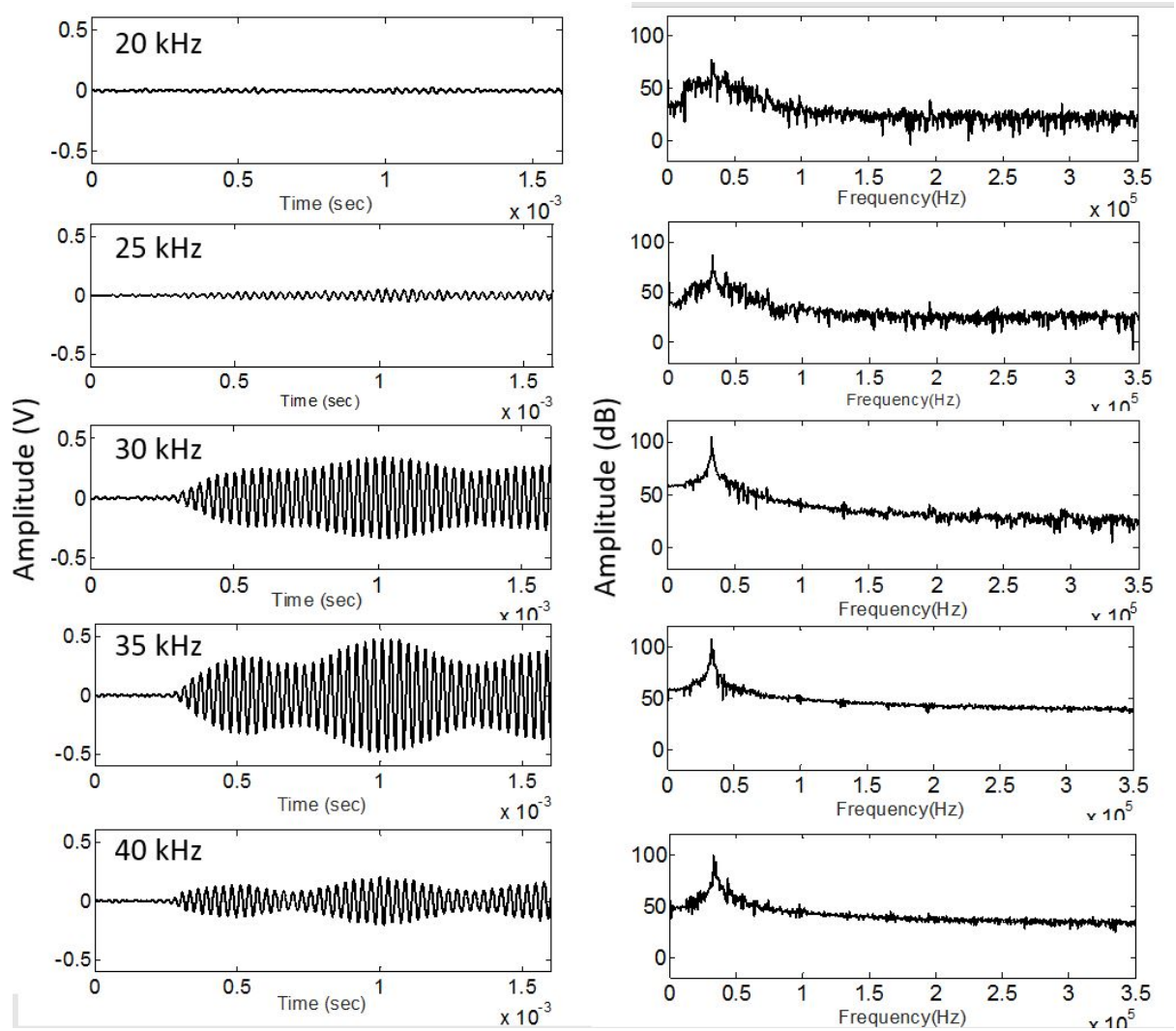


Figure 47. The LF sensor responses at different excitation frequencies (a) time history signals and (b) their frequency spectra

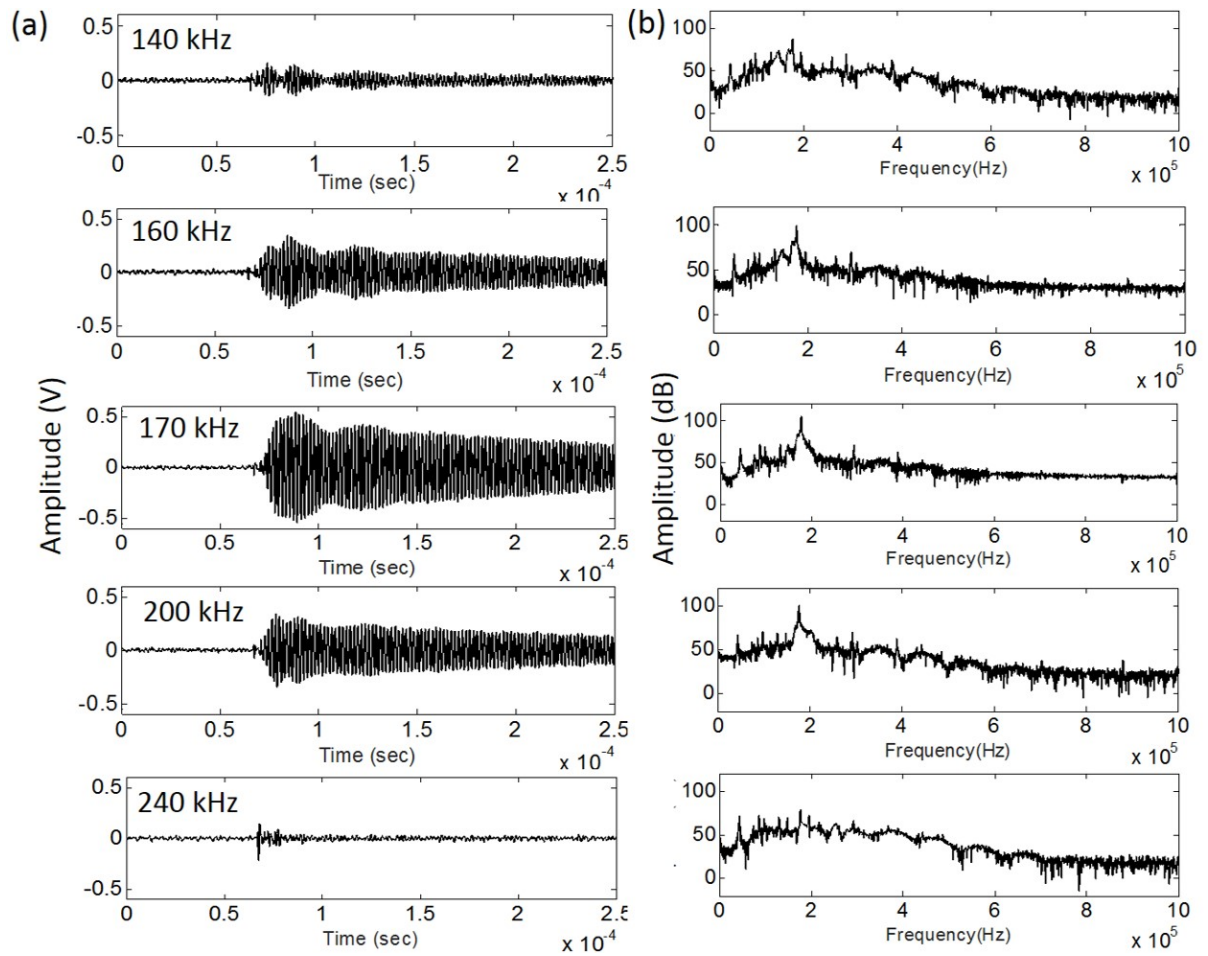


Figure 48. The HF sensor responses at different excitation frequencies (a) time history signals and (b) their frequency spectra

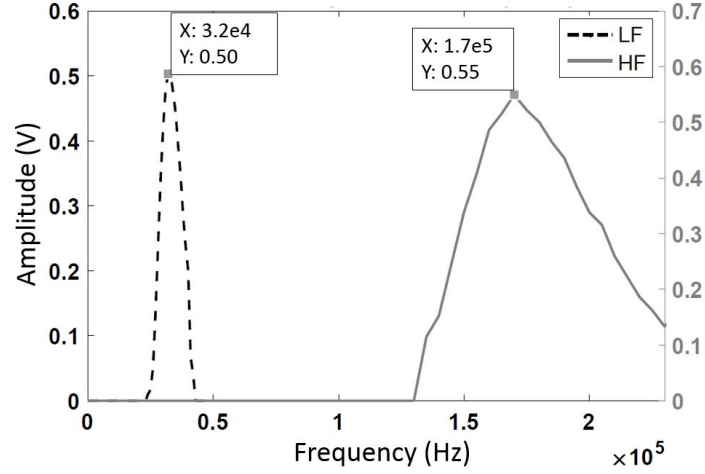


Figure 49. The peak amplitudes of time history signals due to different excitation frequencies

coupling of about one hundred LF sensors, in a 10×10 array (1 cm^2 area), is sufficient to reach to the sensitivity of conventional piezoelectric AE sensors. The comparison of conventional piezoelectric and piezo-MEMS AE sensors including their dimensions is summarized in Table VI in which thickness includes the packaging of each sensor as well, and total size represents total volume. The comparison of the amplitude/size as shown in Table VI indicates that the HF sensor has superior behavior as compared to the conventional piezoelectric AE sensor.

5.6 Summary

The piezo-MEMS AE sensors are developed using piezoMUMPs provided by MEMSCAP, which have advantage over the capacitive type MEMS AE sensors due to no DC power requirement to operate. Two MEMS sensors from layout 4 are studied in this chapter, with the design resonant frequencies of

TABLE VI

THE COMPARISON OF CONVENTIONAL PIEZOELECTRIC AND PIEZO-MEMS AE SENSORS

Sensor	Diameter/ Width (mm)	Thickness (mm)	Total size (mm ³)	Maximum signal amplitude (V)	Amplitude/Size (mV/mm ³)
R6	19.05	22.35	6373	5.368	0.84
LF	0.9	1	0.81	0.039	48.51
R15	19.05	22.35	6373	7.939	1.24
HF	0.7	1	0.49	0.049	99.59

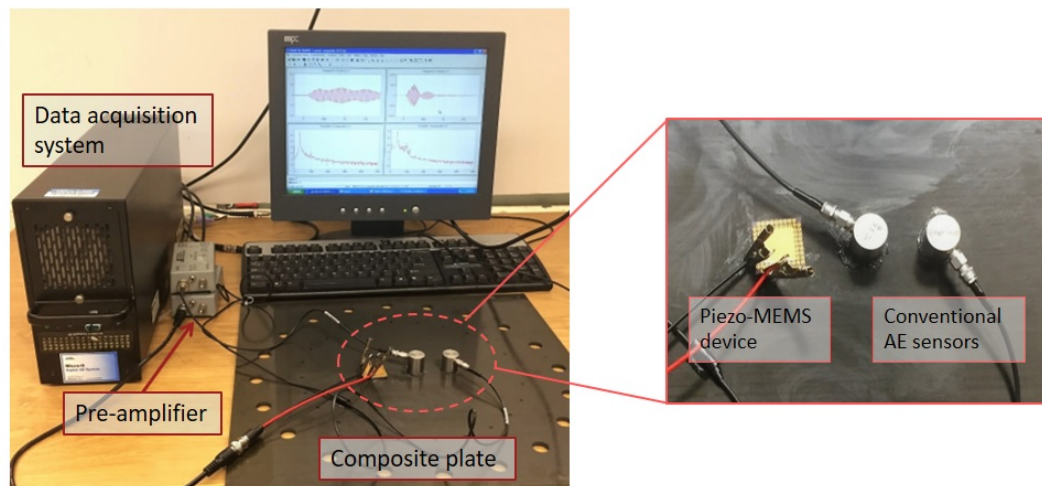


Figure 50. Experimental setup for the comparison of conventional piezoelectric AE sensors and piezo-MEMS AE sensors

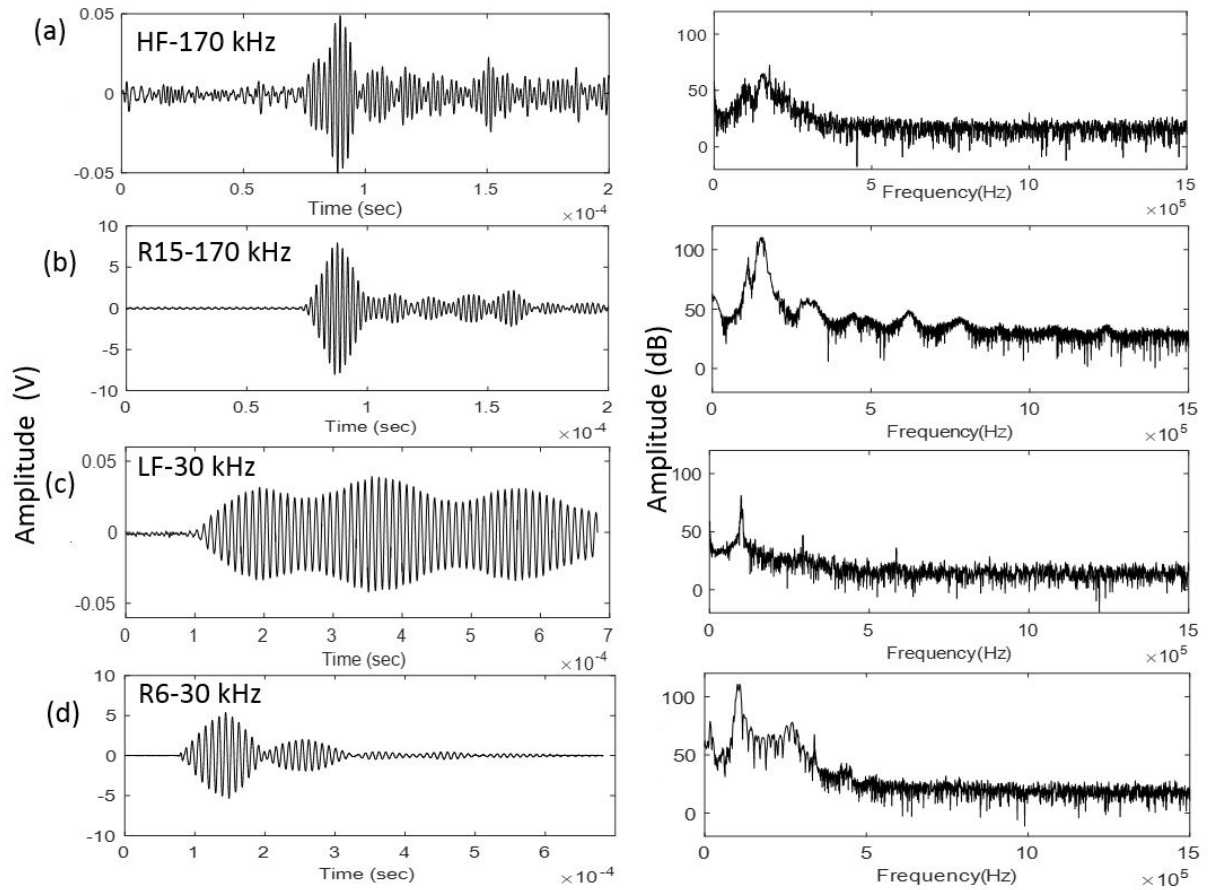


Figure 51. The time history signals and their frequency spectra obtained from (a) HF (piezo-MEMS AE sensor), (b) R15 (conventional AE sensor), (c) LF (piezo-MEMS AE sensor), (d) R6 (conventional AE sensor)

40 kHz (LF sensor) and 200 kHz (HF sensor). The LF sensor is uniquely designed with a mass of entire silicon substrate in order to reduce the overall size of sensor while tuning it to lower frequency. However, the first two modes of vibration of the LF sensors are close, as observed in the numerical models and electromechanical experiments. The numerical simulation of the LF sensor in time-domain demonstrates the narrow-band response of the sensor at the designed frequency, as well as the out-of-plane motion of the sensor. It is observed that no bending occurs in the AlN layer of the LF sensor. As a result, it is concluded that the development of inertial force causes the conversion of mechanical signal into electrical current. The electric field polarization is parallel to the stress distribution in the AlN layer of the LF sensor and d_{33} mode is the dominant mode of piezoelectric conversion. The diaphragm motion is the driving force of the HF sensor, as a result, d_{31} is the dominant mode of piezoelectric conversion.

The LF sensor demonstrates high Q-factor, leading to low damping and very narrow frequency bandwidth, which is important for source localization. The electrical and mechanical characterization experiments indicate an acceptable performance of the designed sensors. The sensitivities of piezo-MEMS sensors taking into account their sizes are comparable to conventional piezoelectric sensors. To increase the sensitivity of the designed piezo-MEMS AE sensors, a group of 100 unit cells can be connected in a 10×10 array (occupying 1 cm^2 area) to reach to the sensitivity of conventional AE sensors.

CHAPTER 6

CONCLUSIONS AND FUTURE WORK

6.1 Conclusions

The overall objective of this research was to advance current AE method through integrating phononic crystals (introduced naturally at the design stage or artificially to existing structures) and piezoelectric MEMS sensors. The research had three major parts to achieve the objective: designing PCs for (i) wave focusing through perforated PC and (ii) noise isolation through stubbed PC, and (iii) designing highly narrow band piezoelectric MEMS AE sensors. The major findings of three parts are presented as follows.

- (i) Perforated PC plate: The goal was to design the connection plate of bridges based on analogy to PC, such that the bolts' locations could guide the wave energy released by newly formed cracks to the location of the AE sensors. Numerical study based on unit cell analysis was performed to calculate the dispersion curve of the PC structure and find the range of frequency band gap. The geometry was designed such that it generated a band gap near 60 kHz to operate with MEMS AE sensors tuned to the resonant frequency of 60 kHz . The dispersion curve of the designed PC plate indicated a band gap range from 51 kHz to 74 kHz . The band gap range was highly dependent on the geometrical parameters of the structure. It was concluded that a high filling factor is required to form a complete band gap, which would result in close distance between the holes through the plate. The 1D PC plate was fabricated based the dimensions found in numerical studies. The band

gap formation was demonstrated through experimental studies, where the capacitive MEMS AE sensor with resonant frequency of 60 *kHz* was employed. The transmission of the wave through the perforated PC plate at the targeted frequency demonstrated the low amplitude compared to the reference plate. However, the lattice size of the PC plate was not practical for the design of gusset plates in truss bridges.

- (ii) Stubbed PC plate: The goal was to eliminate the influence of background noise by blocking the unwanted signal through the stubbed PC. A 2D stubbed PC was designed to form a band gap near 150 *kHz*. The performance of the designed PC structure was demonstrated numerically and experimentally through the fatigue testing of standard compact tension specimens made of Aluminum 7075. The cumulative energy of AE obtained from the stubbed CT specimen showed better correlation with the crack growth, compared to the plain CT specimen without any post-processing filtering. The number of AE hits were decreased by two orders of magnitudes, while the crack activity was clearly observed, which implied the effect of stubs in reducing the secondary sources unrelated to the crack growth. The developed crack detection methodology allows using one AE sensor with periodic stubs placed around the sensor to block the secondary emissions to monitor the behavior of known cracks in structures and reducing the recording of AE hits and the data file, which is crucial to combine the AE method with wireless technology. Besides, the repeatability of AE cumulative activities to correlate with the fatigue crack growth was demonstrated effectively by minimizing the influence of secondary emissions. It was shown that while threshold-dependent features (e.g., energy, duration) could not be controlled by simple post-test amplitude filter, the

cumulative AE hits and amplitude distribution had repeatable patterns in relation to the crack growth.

- (iii) Piezoelectric MEMS AE sensors: While capacitive MEMS AE sensors were successfully demonstrated to operate with the PC plate in the first part, they required DC power, which was not practical for field applications where power source was limited. The piezo-MEMS AE sensors were designed, and manufactured using piezo-MUMPs provided by MEMSCAP, which had advantage over the capacitive type MEMS AE sensors due to no DC power requirement to operate. While the MEMS device included AE and Ultrasonic transducers in addition to piezoresistive strain sensors, two piezo-MEMS AE sensors were studied thoroughly in this research (compatible with the band gap ranges of PC designs). Piezo-MEMS AE sensors had the design resonant frequencies of 40 *kHz* (LF sensor) and 200 *kHz* (HF sensor). The LF sensor was uniquely designed with a mass of entire silicon substrate in order to reduce the overall size of sensor while tuning it to lower frequency. However, the first two modes of vibration of the LF sensors were close, as observed in the numerical models and electromechanical experiments. The numerical simulation of the LF sensor in time-domain demonstrated the narrow band response of the sensor at the designed frequency, as well as the out-of-plane motion of the sensor. It was observed that no bending occurred in the AlN layer of the LF sensor. As a result, it was concluded that the development of inertial force caused the conversion of mechanical signal into electrical current. The electric field polarization was parallel to the stress distribution in the AlN layer of the LF sensor and d_{33} mode is the dominant mode of piezoelectric conversion. The diaphragm motion was the driving force of the HF sensor, as a result, d_{31} was the dominant mode of piezoelectric

conversion. The LF sensor demonstrated high Q-factor, leading to low damping and very narrow frequency bandwidth, which was important for source localization and matching with the narrow band gap of PCs. The electrical and mechanical characterization experiments indicated an acceptable performance of the designed sensors. The sensitivities of piezo-MEMS sensors taking into account their sizes were comparable to conventional piezoelectric sensors.

6.2 Future Work

The future work of this study includes improvements in the design of PCs and the piezo-MEMS sensors considering the feasibility of the application in addition to the expansion of the PC applications to pipeline structures. The future work is as follows:

- More studies will be conducted to find a more practical design of a PC plate which can resemble the bolted connection plates in bridges. The designed perforated PC plate is made of square lattice, which requires high filling factor. The other lattice types such as hexagonal and honeycomb provides larger distances between the holes. The effects of different types of lattices and adding a material with different elastic properties inside the hole will be investigated.
- The present study demonstrated the successful implementation of PCs for noise isolation in AE monitoring of the crack activity in a laboratory controlled fatigue testing of aluminum CT specimens. In future, the performance of the designed PC can be evaluated in field applications. The designed PC can be employed for crack activity monitoring of an existing crack in field to evaluate the performance of the designed PC and assess the single sensor approach in comparison with the conventional multi-sensor approach.


- The stubbed PC will be fabricated using additive manufacturing techniques. 3D printing the PC in a form of patch to be attached to the surface of a structure not only facilitates the fabrication process, but also simplifies the procedure to customize it for different sensors and applications.
- In current experimental testing of PCs for noise isolation, conventional AE sensors are employed. The conventional AE sensors are resonant types; however, they have a certain response bandwidth. In future, the piezo-MEMS AE sensors designed in this research will be employed for sensing. The designed piezo-MEMS AE sensors demonstrate a highly narrow band response, which is significant for the engineered AE approach. Either the geometry of the PC or piezo-MEMS sensor will be exploited to tune to the resonant frequency response of the sensor or the frequency band gap of the PC.
- In this study, the band gap formation and waveguiding behavior is basically studied in homogeneous plate-like structures. The approach will be extended to other structural designs, such as pipelines and aerospace components. The wave propagation and wave modes through cylindrical shape and composite materials are different from plate-like structures. Proper unit cell will be employed for the cases of (a) non-flat surface and (b) heterogeneous materials, and the resulting dispersion curve will be used to tailor the geometry to obtain the desired band gap. A PC can be designed for waveguiding and signal amplifications in hotspots such as the welding line in pipelines.
- The sensitivities of the designed piezo-MEMS AE sensors taking into account their sizes are comparable to conventional piezoelectric sensors. To increase the sensitivity of the designed piezo-

MEMS AE sensors, a group of 100 unit cells will be connected in a 10×10 array (occupying 1 cm^2 area) to reach to the sensitivity of conventional AE sensors.

APPENDICES

Appendix A

COPYRIGHT PERMISSION



Copyright
Clearance
Center



[Home](#)
[Account Info](#)
[Help](#)




Title: Noise isolation with phononic crystals to enhance fatigue crack growth detection using acoustic emission

Author: Minoo Kabir, Amir Mostavi, Didem Ozevin

Publication: Journal of Civil Structural Health Monitoring

Publisher: Springer Nature

Date: Jan 1, 2018

Copyright © 2018, Springer-Verlag GmbH Germany, part of Springer Nature

Logged in as:
Minoo Kabir
University of Illinois at Chicago

[LOGOUT](#)

Order Completed

Thank you for your order.

This Agreement between University of Illinois at Chicago -- Minoo Kabir ("You") and Springer Nature ("Springer Nature") consists of your license details and the terms and conditions provided by Springer Nature and Copyright Clearance Center.

Your confirmation email will contain your order number for future reference.

[printable details](#)

License Number	4380301318096
License date	Jul 01, 2018
Licensed Content Publisher	Springer Nature
Licensed Content Publication	Journal of Civil Structural Health Monitoring
Licensed Content Title	Noise isolation with phononic crystals to enhance fatigue crack growth detection using acoustic emission
Licensed Content Author	Minoo Kabir, Amir Mostavi, Didem Ozevin
Licensed Content Date	Jan 1, 2018
Type of Use	Thesis/Dissertation
Requestor type	academic/university or research institute
Format	print and electronic
Portion	full article/chapter
Will you be translating?	no
Circulation/distribution	<501
Author of this Springer Nature content	yes
Title	Engineered Acoustic Emission Sensing in Metallic Structures by\\ Phononic Crystals and MEMS Sensors
Instructor name	Didem Ozevin
Institution name	University of Illinois at Chicago
Expected presentation date	Aug 2018
Requestor Location	University of Illinois at Chicago 842 West Taylor St. ERF2095 CHICAGO, IL 60607

Appendix A (continued)



RightsLink®

[Home](#)
[Create Account](#)
[Help](#)




Title: Piezoelectric MEMS Acoustic Emission Sensors

Author: Mino Kabir, Hanie Kazari, Didem Ozevin

Publication: Sensors and Actuators A: Physical

Publisher: Elsevier

Date: 15 August 2018

© 2018 Elsevier B.V. All rights reserved.

LOGIN

If you're a copyright.com user, you can login to RightsLink using your copyright.com credentials. Already a **RightsLink user** or want to [learn more?](#)

Please note that, as the author of this Elsevier article, you retain the right to include it in a thesis or dissertation, provided it is not published commercially. Permission is not required, but please ensure that you reference the journal as the original source. For more information on this and on your other retained rights, please visit: <https://www.elsevier.com/about/our-business/policies/copyright#Author-rights>

[BACK](#)
[CLOSE WINDOW](#)

Copyright © 2018 [Copyright Clearance Center, Inc.](#) All Rights Reserved. [Privacy statement](#). [Terms and Conditions](#).
Comments? We would like to hear from you. E-mail us at customercare@copyright.com

Appendix A (continued)

Subject: Reprint Permission

From: Me (minoo.kabir@gmail.com)

To: reprint-permission@spie.org

April 17, 2018

Dear Publisher,

I'm a Co-Author of the following paper. I need to use some of the content published in this paper as a part of my dissertation and I need a written permission for that purpose.

Kabir, M. and Ozevin, D., "Integration of periodic structure and highly narrowband mems sensor to enhance crack detection ability in steel structures." In SPIE Nanoscience+ Engineering, pages 99181N-99181N. International Society for Optics and Photonics, 2016.

Sincerely,

Minoo Kabir

Dear Minoo Kabir,

Thank you for seeking permission from SPIE to reprint material from our publications. As author, SPIE shares the copyright with you, so you retain the right to reproduce your paper in part or in whole.

Publisher's permission is hereby granted under the following conditions:

(1) the material to be used has appeared in our publication without credit or acknowledgment to another source; and

(2) you credit the original SPIE publication. Include the authors' names, title of paper, volume title, SPIE volume number, and year of publication in your credit statement.

Sincerely,

Nicole Harris

Administrative Editor, SPIE Publications

1000 20th St.

Bellingham, WA 98225

+1 360 685 5586 (office)

nicoleh@spie.org

SPIE is the international society for optics and photonics. <http://SPIE.org>

CITED LITERATURE

1. Kabir, M., Mostavi, A., and Ozevin, D.: Noise isolation with phononic crystals to enhance fatigue crack growth detection using acoustic emission. Journal of Civil Structural Health Monitoring, 2018.
2. Kabir, M., Kazari, H., and Ozevin, D.: Piezoelectric mems acoustic emission sensors. Sensors and Actuators A: Physical, 279:53 – 64, 2018.
3. Kabir, M. and Ozevin, D.: Integration of periodic structure and highly narrowband mems sensor to enhance crack detection ability in steel structures. In SPIE Nanoscience+ Engineering, pages 99181N–99181N. International Society for Optics and Photonics, 2016.
4. Saboonchi, H.: Design and Characterization of the MEMS Sensor Fusion for Real Time Damage Detection in Structures. Doctoral dissertation, University of Illinois at Chicago, 2014.
5. Saboonchi, H., Ozevin, D., and Kabir, M.: Mems sensor fusion: Acoustic emission and strain. Sensors and Actuators A: Physical, 247:566–578, 2016.
6. Bridge & structures office, skagit river bridge emergency. Technical report, Washington State Department of Transportation, 2014.
7. Caplan-Bricker, N.: This is what happens when a pipeline bursts in your town. Technical report, The New Republic, 2013.
8. Graybeal, B. A., Phares, B. M., Rolander, D. D., Moore, M., and Washer, G.: Visual inspection of highway bridges. Journal of nondestructive evaluation, 21(3):67–83, 2002.
9. Washer, G.: Reliability of visual inspection for highway bridges volume i: Final report. Technical report, Local Technical Assistance Program (LTAP), 2003.
10. Phares, B. M., Washer, G. A., Rolander, D. D., Graybeal, B. A., and Moore, M.: Routine highway bridge inspection condition documentation accuracy and reliability. Journal of Bridge Engineering, 9(4):403–413, 2004.

11. Moll, J. and Fritzen, C.-P.: Guided waves for autonomous online identification of structural defects under ambient temperature variations. Journal of Sound and Vibration, 331(20):4587–4597, 2012.
12. Chen, X., Michaels, J. E., Lee, S. J., and Michaels, T. E.: Load-differential imaging for detection and localization of fatigue cracks using lamb waves. NDT & E International, 51:142–149, 2012.
13. Ozevin, D., Pessiki, S. P., Jain, A., Greve, D. W., and Oppenheim, I. J.: Development of a mems device for acoustic emission testing. volume 5057, pages 5057 – 5057 – 11, 2003.
14. Kabir, M., Saboonchi, H., and Ozevin, D.: The design, characterization, and comparison of mems comb-drive acoustic emission transducers with the principles of area-change and gap-change. In SPIE Smart Structures and Materials+ Nondestructive Evaluation and Health Monitoring, pages 94352B–94352B. International Society for Optics and Photonics, 2015.
15. Spanner, J. C.: Acoustic emission techniques and applications. NDT INTERNATIONAL, page 107, 1977.
16. Liptai, R., Harris, D., and Tatro, C.: An introduction to acoustic emission. In Acoustic Emission. ASTM International, 1972.
17. Sachse, W.: Applications of Quantitative AE Methods: Dynamic Fracture, Materials and Transducer Characterization, pages 41–64. Dordrecht, Springer Netherlands, 1987.
18. Ohtsu, M.: The history and development of acoustic emission in concrete engineering. Magazine of concrete research, 48(177):321–330, 1996.
19. Miller, R., Pollock, A., Watts, D., Carlyle, J., Tafuri, A., and Yezzi, J.: A reference standard for the development of acoustic emission pipeline leak detection techniques. NDT & E International, 32(1):1–8, 1999.
20. Rens, K. L., Wipf, T. J., and Klaiber, F. W.: Review of nondestructive evaluation techniques of civil infrastructure. Journal of performance of constructed facilities, 11(4):152–160, 1997.
21. Ono, K.: Structural integrity evaluation using acoustic emission. J. Acoustic Emission, 25:1–20, 2007.

22. Holford, K. M., Pullin, R., Evans, S. L., Eaton, M. J., Hensman, J., and Worden, K.: Acoustic emission for monitoring aircraft structures. Proceedings of the Institution of Mechanical Engineers, Part G: Journal of Aerospace Engineering, 223(5):525–532, 2009.
23. Yu, J., Ziehl, P., Matta, F., and Pollock, A.: Acoustic emission detection of fatigue damage in cruciform welded joints. Journal of Constructional Steel Research, 86:85–91, 2013.
24. Holford, K. M., Eaton, M. J., Hensman, J. J., Pullin, R., Evans, S. L., Dervilis, N., and Worden, K.: A new methodology for automating acoustic emission detection of metallic fatigue fractures in highly demanding aerospace environments: An overview. Progress in Aerospace Sciences, 2017.
25. McCrory, J. P., Al-Jumaili, S. K., Crivelli, D., Pearson, M. R., Eaton, M. J., Featherston, C. A., Guagliano, M., Holford, K. M., and Pullin, R.: Damage classification in carbon fibre composites using acoustic emission: A comparison of three techniques. Composites Part B: Engineering, 68:424–430, 2015.
26. Nair, A. and Cai, C.: Acoustic emission monitoring of bridges: Review and case studies. Engineering structures, 32(6):1704–1714, 2010.
27. Nazarchuk, Z., Skalskyi, V., and Serhiyenko, O.: Acoustic Emission: Methodology and Application. Foundations of Engineering Mechanics. Springer International Publishing, 2017.
28. Ebrahimkhanlou, A. and Salamone, S.: A deep learning approach for single-sensor acoustic emission source localization in plate-like structures. Structural Health Monitoring 2017, 2017.
29. Ebrahimkhanlou, A. and Salamone, S.: A probabilistic framework for single-sensor acoustic emission source localization in thin metallic plates. Smart Materials and Structures, 26(9):095026, 2017.
30. Ritchie, R.: Near-threshold fatigue-crack propagation in steels. International Metals Reviews, 24(1):205–230, 1979.
31. Ono, K.: Acoustic Emission, pages 1209–1229. Springer New York, 2014.
32. Li, D., Kuang, K. S. C., and Koh, C. G.: Fatigue crack sizing in rail steel using crack closure-induced acoustic emission waves. Measurement Science and Technology, 28(6):065601, 2017.

33. Zhang, L., Ozevin, D., Hardman, W., and Timmons, A.: Acoustic emission signatures of fatigue damage in idealized bevel gear spline for localized sensing. Metals, 7(7), 2017.
34. Hopwood, I., Oka, V. G., Deen, R. C., et al.: Reliability assessment of high-risk steel bridges by nondestructive test methods. 1987.
35. McKeefry, J. A. and Shield, C. K.: Acoustic emission monitoring of fatigue cracks in steel bridge girders. 1999.
36. Yoon, D., Jung, J., Kim, K., Park, P., and Lee, S.: Ae parameter analysis for fatigue crack monitoring. In the 15th World Conference on Nondestructive Tesfing, 2000.
37. Kosnik, D. E.: Acoustic emission testing of a difficult-to-reach steel bridge detail. Journal of Acoustic Emission, 27:11–17, 2009.
38. Kosnik, D. E., Hopwood, T., Corr, D., Thompson, D. O., and Chimenti, D. E.: Acoustic emission monitoring for assessment of steel bridge details. In AIP Conference Proceedings-American Institute of Physics, volume 1335, page 1410, 2011.
39. Simon, S. H.: The Oxford solid state basics. Oxford University Press, 2013.
40. Perkowitz, S.: Phonons. <http://www.britannica.com/science/phonon>, 2016. Accessed: 2016-03-16.
41. Gorishnyy, T., Maldovan, M., Ullal, C., and Thomas, E.: Sound ideas. Physics World, 18(12):24, 2005.
42. Kushwaha, M. S., Halevi, P., Dobrzynski, L., and Djafari-Rouhani, B.: Acoustic band structure of periodic elastic composites. Physical review letters, 71(13):2022, 1993.
43. Kushwaha, M. and Halevi, P.: Band-gap engineering in periodic elastic composites. Applied Physics Letters, 64(9):1085–1087, 1994.
44. Mohammadi, S., Eftekhar, A. A., Khelif, A., Hunt, W. D., and Adibi, A.: Evidence of large high frequency complete phononic band gaps in silicon phononic crystal plates. Applied Physics Letters, 92(22):221905, 2008.
45. Deymier, P. A.: Acoustic metamaterials and phononic crystals, volume 173. Springer Science & Business Media, 2013.

46. Foehr, A., Bilal, O. R., Huber, S. D., and Daraio, C.: Spiral-based phononic plates: From wave beaming to topological insulators. arXiv preprint arXiv:1712.01360, 2017.
47. Li, J., Wang, W., Xie, Y., Popa, B.-I., and Cummer, S. A.: A sound absorbing metasurface with coupled resonators. Applied Physics Letters, 109(9):091908, 2016.
48. Pennec, Y., Djafari-Rouhani, B., Vasseur, J., Khelif, A., and Deymier, P. A.: Tunable filtering and demultiplexing in phononic crystals with hollow cylinders. Physical Review E, 69(4):046608, 2004.
49. Mostavi, A., Kabir, M., and Ozevin, D.: Enhancing the robustness of nonlinear ultrasonic testing by implementing 1d phononic crystals. Structural Health Monitoring 2017, 2017.
50. Zanjani, M. B., Davoyan, A. R., Mahmoud, A. M., Engheta, N., and Lukes, J. R.: One-way phonon isolation in acoustic waveguides. Applied Physics Letters, 104(8):081905, 2014.
51. Sigalas, M. and Economou, E.: Band structure of elastic waves in two dimensional systems. Solid State Communications, 86(3):141–143, 1993.
52. Kushwaha, M., Halevi, P., Martinez, G., Dobrzynski, L., and Djafari-Rouhani, B.: Theory of acoustic band structure of periodic elastic composites. Physical Review B, 49(4):2313, 1994.
53. Sigalas, M. and Economou, E.: Elastic and acoustic wave band structure. Journal of sound and vibration, 158(2):377–382, 1992.
54. Sigalas, M. and Economou, E.: Band structure of elastic waves in two dimensional systems. Solid State Communications, 86(3):141 – 143, 1993.
55. Kushwaha, M. S.: Classical band structure of periodic elastic composites. International Journal of Modern Physics B, 10(09):977–1094, 1996.
56. Martinezsala, R., Sancho, J., Sánchez, J., Gómez, V., Llinares, J., Meseguer, F., et al.: Sound attenuation by sculpture. nature, 378(6554):241–241, 1995.
57. De Espinosa, F. M., Jimenez, E., and Torres, M.: Ultrasonic band gap in a periodic two-dimensional composite. Physical Review Letters, 80(6):1208, 1998.

58. Vasseur, J., Deymier, P., Chenni, B., Djafari-Rouhani, B., Dobrzynski, L., and Prevost, D.: Experimental and theoretical evidence for the existence of absolute acoustic band gaps in two-dimensional solid phononic crystals. Physical Review Letters, 86(14):3012, 2001.
59. Wu, T.-T., Huang, Z.-G., Tsai, T.-C., and Wu, T.-C.: Evidence of complete band gap and resonances in a plate with periodic stubbed surface. Applied Physics Letters, 93(11):111902, 2008.
60. Pennec, Y., Djafari-Rouhani, B., Larabi, H., Vasseur, J., and Hladky-Hennion, A.: Low-frequency gaps in a phononic crystal constituted of cylindrical dots deposited on a thin homogeneous plate. Physical Review B, 78(10):104105, 2008.
61. Wu, T.-T., Hsu, J.-C., and Sun, J.-H.: Lamb waves in phononic-crystal plates: Numerical studies and experiments. In IUTAM Symposium on Recent Advances of Acoustic Waves in Solids, pages 221–231. Springer, 2010.
62. Oudich, M., Li, Y., Assouar, B. M., and Hou, Z.: A sonic band gap based on the locally resonant phononic plates with stubs. New Journal of Physics, 12(8):083049, 2010.
63. Oudich, M., Senesi, M., Assouar, M. B., Ruzenne, M., Sun, J.-H., Vincent, B., Hou, Z., and Wu, T.-T.: Experimental evidence of locally resonant sonic band gap in two-dimensional phononic stubbed plates. Physical Review B, 84(16):165136, 2011.
64. Olsson Iii, R. and El-Kady, I.: Microfabricated phononic crystal devices and applications. Measurement Science and Technology, 20(1):012002, 2008.
65. Wu, T.-T., Wu, L.-C., and Huang, Z.-G.: Frequency band-gap measurement of two-dimensional air/silicon phononic crystals using layered slanted finger interdigital transducers. Journal of Applied Physics, 97(9):094916, 2005.
66. Grosse, C. U. and Ohtsu, M.: Acoustic emission testing. Springer Science & Business Media, 2008.
67. MEMS and Exchange, N.: About mems, 2016.
68. Khuri-Yakub, B. T., Degertekin, F., Jin, X.-C., Calmes, S., Ladabaum, I., Hansen, S., and Zhang, X.: Silicon micromachined ultrasonic transducers. In Ultrasonics Symposium, 1998. Proceedings., 1998 IEEE, volume 2, pages 985–991. IEEE, 1998.

69. Eddy, D. S. and Sparks, D. R.: Application of mems technology in automotive sensors and actuators. Proceedings of the IEEE, 86(8):1747–1755, 1998.
70. Khuri-Yakub, B. T. and Oralkan, Ö.: Capacitive micromachined ultrasonic transducers for medical imaging and therapy. Journal of micromechanics and microengineering, 21(5):054004, 2011.
71. Grosse, C. U. and Krüger, M.: Wireless acoustic emission sensor networks for structural health monitoring in civil engineering. In Proc. European Conf. on Non-Destructive Testing (ECNDT), DGZfP BB-103-CD. Citeseer, 2006.
72. Schoess, J. N. and Zook, J. D.: Test results of a resonant integrated microbeam sensor (rims) for acoustic emission monitoring. In 5th Annual International Symposium on Smart Structures and Materials, pages 326–332. International Society for Optics and Photonics, 1998.
73. Varadan, V. and Varadan, V.: Wireless remotely readable and programmable microsensors and mems for health monitoring of aircraft structures. Structural Health Monitoring, pages 96–105, 2000.
74. Ozevin, D., Pessiki, S. P., Jain, A., Greve, D. W., and Oppenheim, I. J.: Development of a mems device for acoustic emission testing. In Smart Structures and Materials, pages 64–74. International Society for Optics and Photonics, 2003.
75. Ozevin, D., Greve, D., Oppenheim, I., and Pessiki, S.: Resonant capacitive mems acoustic emission transducers. Smart materials and structures, 15(6):1863, 2006.
76. Oppenheim, I. J., Greve, D. W., Ozevin, D., Hay, D. R., Hay, T. R., Pessiki, S. P., and Tyson, N. L.: Structural tests using a mems acoustic emission sensor. In Smart Structures and Materials, pages 617404–617404. International Society for Optics and Photonics, 2006.
77. Greve, D. W., Oppenheim, I. J., Wright, A. P., and Wu, W.: Design and testing of a mems acoustic emission sensor system. In The 15th International Symposium on: Smart Structures and Materials & Nondestructive Evaluation and Health Monitoring, pages 69321P–69321P. International Society for Optics and Photonics, 2008.
78. Harris, A., Oppenheim, I., and Greve, D.: Mems-based high-frequency vibration sensors. Smart Materials and Structures, 20(7):075018, 2011.
79. Wright, A. P.: A multi-axis capacitive mems sensor system for acoustic emission sensing, 2009.

80. Saboonchi, H. and Ozevin, D.: MemS acoustic emission transducers designed with high aspect ratio geometry. Smart Materials and Structures, 22(9):095006, 2013.
81. Kabir, M., Kazari, H., and Ozevin, D.: Piezoelectric micromachined acoustic emission sensors for early stage damage detection in structures. volume 10599, pages 10599 – 10599 – 7, 2018.
82. Jung, J., Lee, W., Kang, W., Shin, E., Ryu, J., and Choi, H.: Review of piezoelectric micro-machined ultrasonic transducers and their applications. Journal of Micromechanics and Microengineering, 27(11):113001, 2017.
83. Hao, Z. and Liao, B.: An analytical study on interfacial dissipation in piezoelectric rectangular block resonators with in-plane longitudinal-mode vibrations. Sensors and Actuators A: Physical, 163(1):401–409, 2010.
84. Akasheh, F., Myers, T., Fraser, J. D., Bose, S., and Bandyopadhyay, A.: Development of piezo-electric micromachined ultrasonic transducers. Sensors and Actuators A: Physical, 111(2-3):275–287, 2004.
85. Wong, L. L., Na, S., Chen, A. I., Li, Z., Macecek, M., and Yeow, J. T.: A feasibility study of piezoelectric micromachined ultrasonic transducers fabrication using a multi-user memS process. Sensors and Actuators A: Physical, 247:430–439, 2016.
86. Wang, Y., Ding, H., Le, X., Wang, W., and Xie, J.: A memS piezoelectric in-plane resonant accelerometer based on aluminum nitride with two-stage microleverage mechanism. Sensors and Actuators A: Physical, 254:126–133, 2017.
87. Feng, G.-H. and Chen, W.-M.: Micromachined lead zirconium titanate thin-film-cantilever-based acoustic emission sensor with poly (n-isopropylacrylamide) actuator for increasing contact pressure. Smart Materials and Structures, 25(5):055046, 2016.
88. Sommer, R., Freitag, M., Schaufuss, J., Sorger, A., and Mehner, J.: Improved memS ae sensors in harm technology. In Systems, Signals & Devices (SSD), 2014 11th International Multi-Conference on, pages 1–4. IEEE, 2014.
89. Lu, Y., Tang, H.-Y., Fung, S., Boser, B. E., and Horsley, D. A.: Pulse-echo ultrasound imaging using an aln piezoelectric micromachined ultrasonic transducer array with transmit beam-forming. Journal of Microelectromechanical Systems, 25(1):179–187, 2016.

90. Massimino, G., D'Alessandro, L., Procopio, F., Ardito, R., Ferrera, M., and Corigliano, A.: Air-coupled pmut at 100 khz with pzt active layer and residual stresses: Multiphysics model and experimental validation. In Thermal, Mechanical and Multi-Physics Simulation and Experiments in Microelectronics and Microsystems (EuroSimE), 2017 18th International Conference on, pages 1–4. IEEE, 2017.
91. Shelton, S., Chan, M.-L., Park, H., Horsley, D., Boser, B., Izyumin, I., Przybyla, R., Frey, T., Judy, M., Nunan, K., et al.: Cmos-compatible aln piezoelectric micromachined ultrasonic transducers. In Ultrasonics Symposium (IUS), 2009 IEEE International, pages 402–405. IEEE, 2009.
92. Cowen, A., Hames, G., Glukh, K., and Hardy, B.: PiezoMUMPs Design Handbook. MEMSCAP Inc., revision 1.3 edition, 2014.
93. Khelif, A., Achaoui, Y., and Aoubiza, B.: Acoustic Metamaterials: Negative Refraction, Imaging, Lensing and Cloaking, chapter Locally Resonant Structures for Low Frequency Surface Acoustic Band Gap Applications, pages 43–59. Springer Netherlands, 2013.
94. Elabbasi, N.: Modeling phononic band gap materials and structures, 2016.
95. Wu, T.-T., Wu, T.-C., and Hsu, J.-C.: Band gaps and waveguiding of lamb waves in stubbed phononic plates. In SPIE OPTO: Integrated Optoelectronic Devices, pages 72230G–72230G. International Society for Optics and Photonics, 2009.
96. Laude, V., Beugnot, J.-C., Benchabane, S., Pennec, Y., Djafari-Rouhani, B., Papanikolaou, N., Escalante, J. M., and Martinez, A.: Simultaneous guidance of slow photons and slow acoustic phonons in silicon phoxonic crystal slabs. Optics express, 19(10):9690–9698, 2011.
97. Wan, X., Peter, W. T., Chen, J., Xu, G., and Zhang, Q.: Second harmonic reflection and transmission from primary s0 mode lamb wave interacting with a localized microscale damage in a plate: A numerical perspective. Ultrasonics, 2017.
98. Mostavi, A., Kabir, M., and Ozevin, D.: The integration of superlattices and immersion nonlinear ultrasonics to enhance damage detection threshold. Applied Physics Letters, 111(20):201905, 2017.
99. Pennec, Y. and Djafari-Rouhani, B.: Fundamental Properties of Phononic Crystal, pages 23–50. New York, NY, Springer New York, 2016.

100. Wu, T.-C., Wu, T.-T., and Hsu, J.-C.: Waveguiding and frequency selection of lamb waves in a plate with a periodic stubbed surface. Physical Review B, 79(10):104306, 2009.
101. Liu, A. F.: Mechanical properties data for selected aluminum alloys. 2013.
102. COMSOL Multiphysics Application Library: Single Edge Crack, 2016.
103. Setter, N., Damjanovic, D., Eng, L., Fox, G., Gevorgian, S., Hong, S., Kingon, A., Kohlstedt, H., Park, N., Stephenson, G., et al.: Ferroelectric thin films: Review of materials, properties, and applications. Journal of Applied Physics, 100(5):051606, 2006.
104. Dubois, M.-A. and Muralt, P.: Properties of aluminum nitride thin films for piezoelectric transducers and microwave filter applications. Applied Physics Letters, 74(20):3032–3034, 1999.
105. Alper, E. and Inman, D. J.: Piezoelectric Energy Harvesting. John Wiley & Sons, April 2011.
106. Zhang, M., Yang, J., Si, C., Han, G., Zhao, Y., and Ning, J.: Research on the piezoelectric properties of aln thin films for mems applications. Micromachines, 6(9):1236–1248, 2015.
107. Choi, H., Ding, J., Bandyopadhyay, A., Anderson, M., and Bose, S.: Characterization and modeling of a piezoelectric micromachined ultrasonic transducer with a very large length/width aspect ratio. Journal of micromechanics and microengineering, 18(2):025037, 2008.
108. Ebrahimkhanlou, A. and Salamone, S.: Acoustic emission source localization in thin metallic plates: A single-sensor approach based on multimodal edge reflections. Ultrasonics, 78:134–145, 2017.

Minoo Kabir

Chicago, IL 60608, (312) 701-4186 | <https://www.linkedin.com/in/minoo-kabir> | minoo.kabir@gmail.com

EDUCATION

University of Illinois at Chicago

May 2018

Ph.D. in Civil and Materials Engineering with focus on Structural Engineering

Thesis: Engineered Acoustic Emission Sensing in Metallic Structures by Phononic Crystals and MEMS Sensors

Advisor: Prof. D. Ozevin

Sharif University of Technology (SUT), Iran

Sept. 2011 - June 2013

Master of Science in Structural Engineering

Thesis: Investigating Layout of Shear Walls in Tall Buildings with Non-symmetrical Plan

Advisor: Prof. A. Khaloo

Sharif University of Technology (SUT), Iran

Sept. 2007 - Sept. 2011

Bachelor of Science in Civil Engineering

PROFESSIONAL EXPERIENCE

Research Assistant,

Jan. 2014 - Present

University of Illinois at Chicago, Chicago, IL

- Noise Isolation through Phononic Crystals to Detect Active Cracks in Steel Bridges funded by National Science Foundation (*Designed a two-dimensional acoustic metamaterial to block background noise; consequently, enhanced fatigue crack growth detection capability of Acoustic Emission technique in plate-like structures*)
- Multi-sensor Fusion using Piezo MEMS for Detecting Weld Defects in Real Time funded by UI Labs DMDII (*Designed piezoelectric MEMS sensors working at low frequencies for Acoustic Emission detection, and high frequencies for Ultrasonic Testing*)
- Integrating 1D Phononic Crystals and Immersion Nonlinear Ultrasonic Testing to Enhance Damage Detection Threshold
- The Identification of Efficient Busyness in Composite Structures for Real Time Damage Detection using Acoustic Emission in collaboration with Drexel University
- The Integrated Phononic Crystals and Nonlinear Ultrasonic to Detect Creep and Fatigue Damage in Metals Bridges funded by National Science Foundation (*Designed a Superlattice to block the nonlinearity generated in water; consequently, improved immersion NLUT method*)
- Periodic Design of Steel Truss Systems for Early Damage Detection funded by National Science Foundation
- The Characterization of Capacitive MEMS Sensors for Acoustic Emission Detection
- Designed and fabricated a micro thermal actuator using microfabrication techniques

Research Assistant,

Sept. 2011- June 2013

Sharif University of Technology, Tehran, Iran

- Investigating Layout of Shear Walls in Tall Buildings with Non-symmetrical Plan, (Designed 20-story and 45-story concrete buildings by ETABS)

Intern, Keyson Construction Co. (Leading EPC contractor), Tehran, Iran

June 2011- Sept. 2011

- Bid evaluation and tendering documentation management, review EPC

Intern, Ameran Ofogh Co. (EPC Contractor for Power Plant), Tehran, Iran

June 2012- Sept. 2012

- Design of Steel and Concrete Buildings

TEACHING AND MENTORING EXPERIENCE

Teaching Assistant, Fall 2014- Spring 2016

Design of Prestressed Concrete Structures, Behavior and Design of Metal Structures, Advanced Design of Metal Structures, Structural Analysis I

- Graded homework/quizzes and conducted weekly office hours.
- Designed the project question and assisted students with their final project.

Mentoring Undergraduate Students (2015-2018)

- Mentored a group of undergraduate students on their senior design project, “The application of shape memory alloys in design of bridges”, 2018.
- Mentored two female undergraduate research assistants, and published conference papers jointly.
- Participated to women mentoring program to bring current female students, and alumni together to enhance their network and increase their retention to Civil Engineering, 2017.

HONORS AND AWARDS

1. Awarded the UIC Chancellor's Graduate Research Award 2017 for interdisciplinary research on “The Integration of Acoustic Metamaterials and MEMS Sensors”
2. Awarded the first place in the 2016 UIC Student Research Forum in the fields of Business/Computer Science/Mathematics + Engineering/Physical Sciences. UIC, Chicago, IL
3. Awarded the "Exceptional Talent Student" title by the SUT admission office that exempted me from M.Sc. program entrance exam.
4. Ranked among top 0.01% of national entry college exam in Iran

PUBLICATIONS AND PRESENTATIONS

Journal Papers

1. Saboonchi, H., Ozevin, D, and **Kabir, M.** (2016, August). “MEMS sensor fusion: Acoustic emission and strain.” *Sensors and Actuators A: Physical* 247: 566-578.
2. Mostavi, A., **Kabir, M.**, Ozevin, D., (2017, Nov.). “The integration of superlattices and immersion nonlinear ultrasonics to enhance damage detection threshold”, *Applied Physics Letter* 111(20): 201905.
3. Can, O., **Kabir, M.** and Ozevin, D. (2018). “Periodic Assembly of Steel Truss Systems for Efficient Analyses and Early Detection of Localized Damage using Impulse Response Method”, *Journal of Structural Engineering* 144(5): 04018032.
4. **Kabir, M.**, Kazari, H. and Ozevin, D., (2018). “Piezoelectric MEMS Acoustic Emission Sensors”, *Sensors and Actuators A: Physical* 279:53-64.
5. **Kabir, M.**, Mostavi, A. and Ozevin, D., (2018). “Noise Isolation with Phononic Crystals to Enhance Fatigue Crack Growth Detection Capability of Acoustic Emission in Steel Structures”, *Journal of Civil Structural Health Monitoring*.
6. **Kabir, M.**, Mostavi, A. and Ozevin, D., (2018). “An Approach towards the Repeatability of Acoustic Emission by Noise Isolation through Phononic Crystals” (drafted).

Conference Papers

1. Kabir, M., Kazari, H. and Ozevin, D. (2018, March). “Piezoelectric Micromachined Acoustic Emission Sensors for Early Stage Damage Detection in Structures”, *SPIE Smart Structures/NDE*, Denver, CO, USA.
2. Kabir, M., Can, O. and Ozevin, D. (2017, September). “The Influence of Periodic Arrangement of Structural Geometry to Ultrasonic Waves”, 11th *International Workshop on Structural Health Monitoring*, Stanford, CA, USA.

3. Mostavi, A., Kabir, M. and Ozevin, D. (2017, September). “Enhancing the Robustness of Nonlinear Ultrasonic Testing by Implementing 1D Phononic Crystals”, 11th *International Workshop on Structural Health Monitoring*, Stanford, CA, USA.
4. Kabir, M., M. G. Allen and D. Ozevin. (2017, March). “3D Printed Metamaterial Design to Focus Wave Energy in Thin Plates”, *SPIE Smart Structures/NDE*, Portland, OR, USA.
5. Kabir, M. and D. Ozevin. (2016, September). “Integration of periodic structure and highly narrowband MEMS sensor to enhance crack detection ability in steel structures”, *SPIE Optics+Photonics*, San Diego, CA, USA.
6. Kabir, M., Saboonchi, H. and Ozevin, D. (2015, September). “Accurate Source Localization using Highly Narrowband and densely populated MEMS acoustic emission sensors”, 10th *International Workshop on Structural Health Monitoring*, San Francisco, CA, USA.
7. Saboonchi, H., Kabir, M. and Ozevin, D. (2015, July). “Numerical and experimental characterizations of 3D MEMS acoustic emission sensors”, *ISHMII conference*, Torino, Italy.
8. Kabir, M., Saboonchi, H. and Ozevin, D. (2015, March). “The design, characterization, and comparison of MEMS comb-drive acoustic emission transducers with the principles of area-change and gap-change”, *SPIE Sensors and Smart Structures Conference*, San Diego, CA, USA.

Presentations

1. Kabir, M., Mostavi, A., Ozevin, D. (2017, December). “Noise Isolation with Acoustic Metamaterials and Piezoelectric MEMS AE Sensors”, Presented at *Mistras Inc.*, Princeton Junction, NJ, USA.
2. Kabir, M., Mostavi, A., Ozevin, D. (2017, November). “Intelligent Crack Activity Detection by Acoustic Metamaterials”, Presented at *UIC Workshop on Structural Design and Inspectability of Highway Bridges*, Chicago, IL, USA.
3. Kabir, M., Pahlavan, P.L., Ozevin, D. (2016, May). “Application of MEMS Acoustic Emission Sensors for Source Location using Quasi-beamforming Approach”, Presented at *AEWG-58 conference*, Drexel University, PA, USA.
4. Kabir, M., Saboonchi, H., Ozevin, D. (2015, May). “Integration of metamaterials and MEMS to block friction emissions”, Presented at *AEWG-57 conference*, Chicago, IL, USA.

SKILLS

Certifications: COMSOL Multiphysics Training, Chicago, IL, April, 2015.

Trained to Operate: Wire-bonding Machine (Wedge-Wedge wire bonder), Lithography, Optical Microscope, Probe station, Impedance analyzer, Oscilloscope and AE data acquisition systems.

Engineering Software: COMSOL Multiphysics, L-Edit, ETABS, SAP, and SAFE.

Computer Programming: MATLAB, Pascal.

Computer Graphics: AutoCAD, Photoshop, Flash5, 3DMax.

Project Management: MSP.

Applicable Program: Microsoft Office (Excel, Word, PowerPoint), LaTeX.

COURSE WORKS

- Non-destructive Testing and Characterization of Materials
- Micromachining and Sensors
- Additive Manufacturing

PROFESSIONAL ORGANIZATION

Member of Acoustic Emission Working Group (AEWG)

Member of American Society of Civil Engineers (ASCE)

Member of the Society of Women Engineers (SWE)